Can Science Save the Earth? – (also) lidar

Alcide Giorgio di Sarra
alcide.disarra@enea.it

IR0000032 – ITINERIS, Italian Integrated Environmental Research Infrastructures System
(D.D. n. 130/2022 - CUP B53C22002150006) Funded by EU - Next Generation EU PNRR-Mission 4 "Education and Research" - Component 2: "From research to business" - Investment 3.1: "Fund for the realisation of an integrated system of research and innovation infrastructures"

Finanziato dall'Unione europea NextGenerationEU
Ministero dell'Università e della Ricerca
Italiadomani

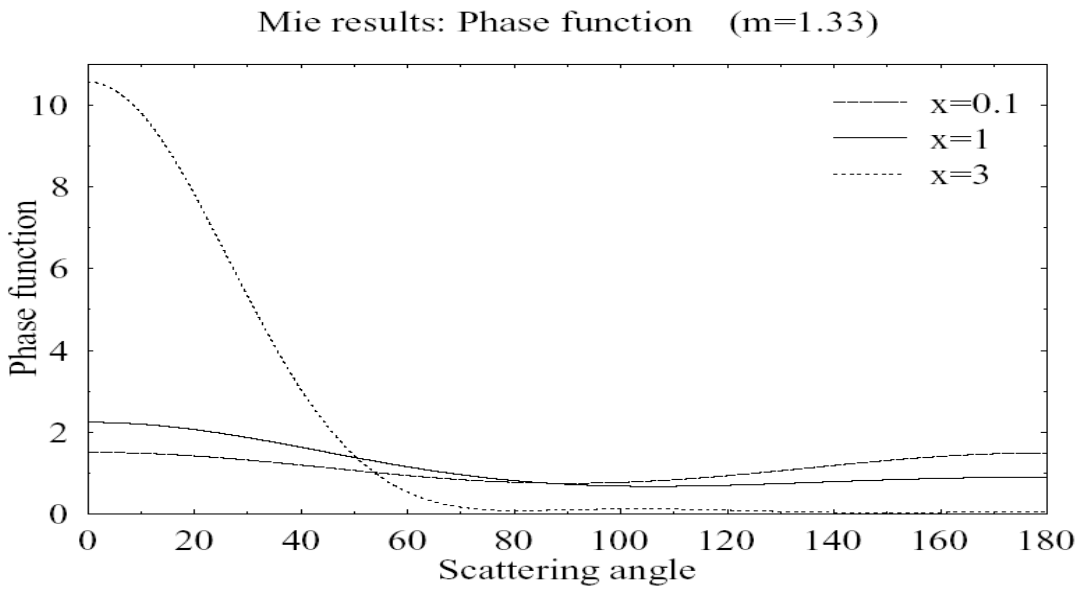
Mie results: Phase function (m=1.33)
Phase function
Scattering angle
x=0.1
x=1
x=3
0
2
4
6
8
10
0
20
40
60
80
100
120
140
160
180

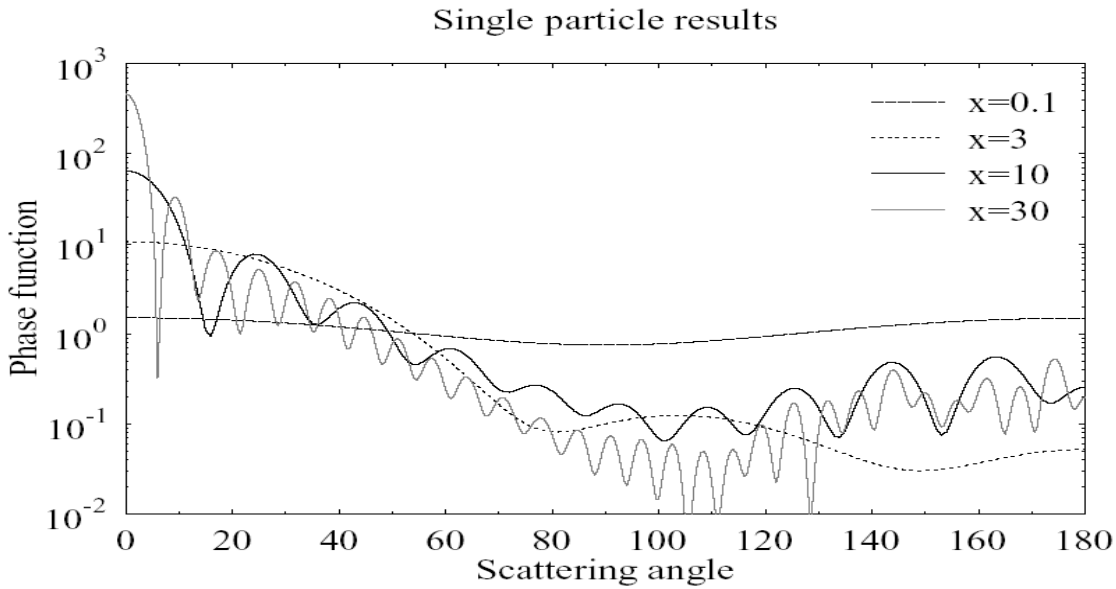
Single particle results
Phase function
Scattering angle
x=0.1
x=3
x=10
x=30
10^{3}
10^{2}
10^{1}
10^{0}
10^{-1}
10^{-2}
0
20
40
60
80
100
120
140
160
180

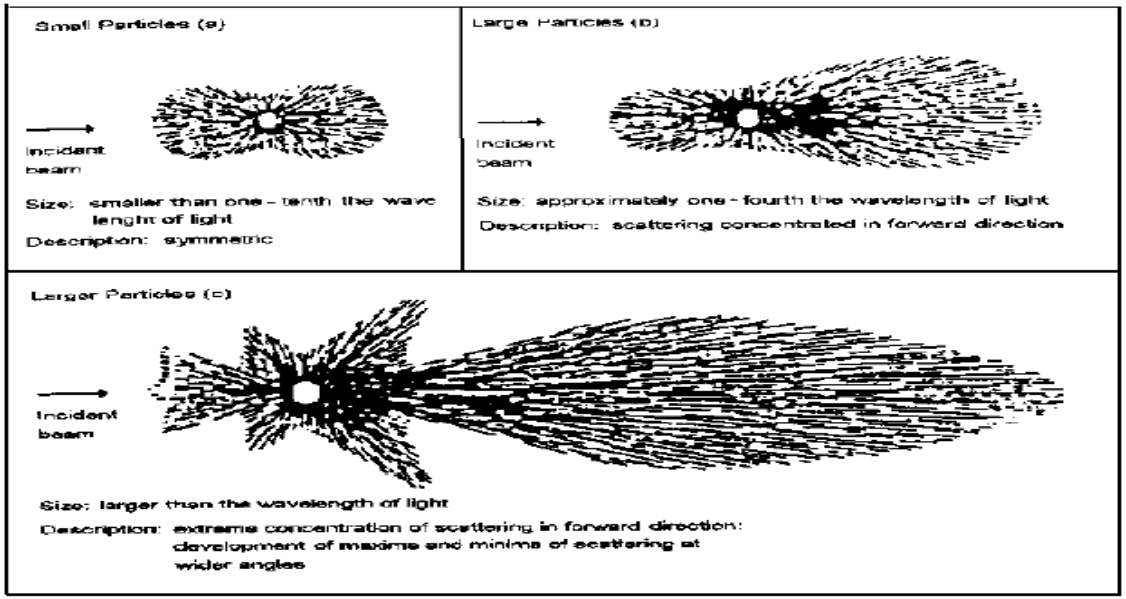

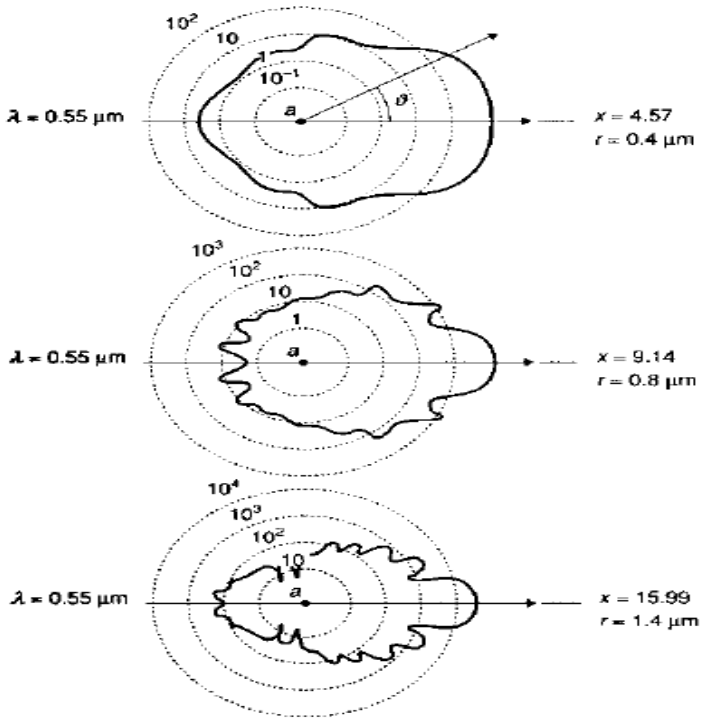

Fig. 6.3 - Diagrammi polari dell'intensità nel piano di diffusione per particelle **sferiche** *a* debolmente assorbenti, di raggio *r*, e per radiazione incidente non **polarizzata** di lunghezza d'onda λ=0.55 μm; $x=2\pi r/\lambda$, è il parametro di Mie.

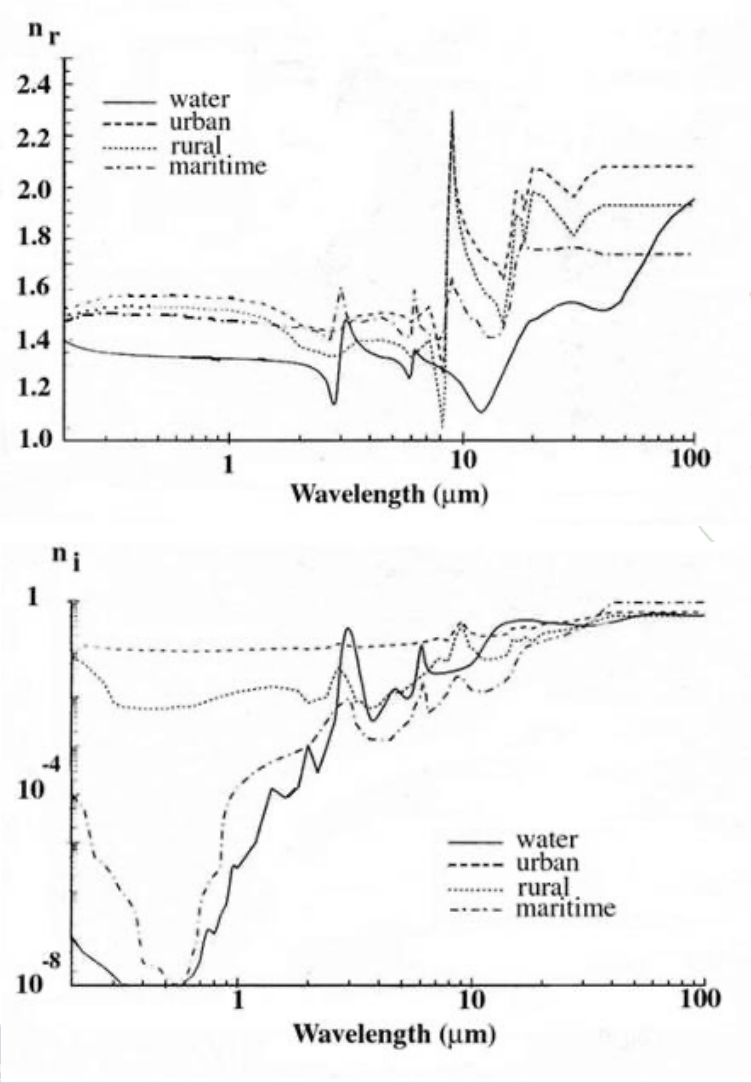
n r
2.4
2.2
2.0
1.8
1.6
1.4
1.2
1.0
water
urban
rural
maritime
1
10
100
Wavelength (μm)
n i
1
10 -4
10 -8
water
urban
rural
maritime
1
10
100
Wavelength (μm)

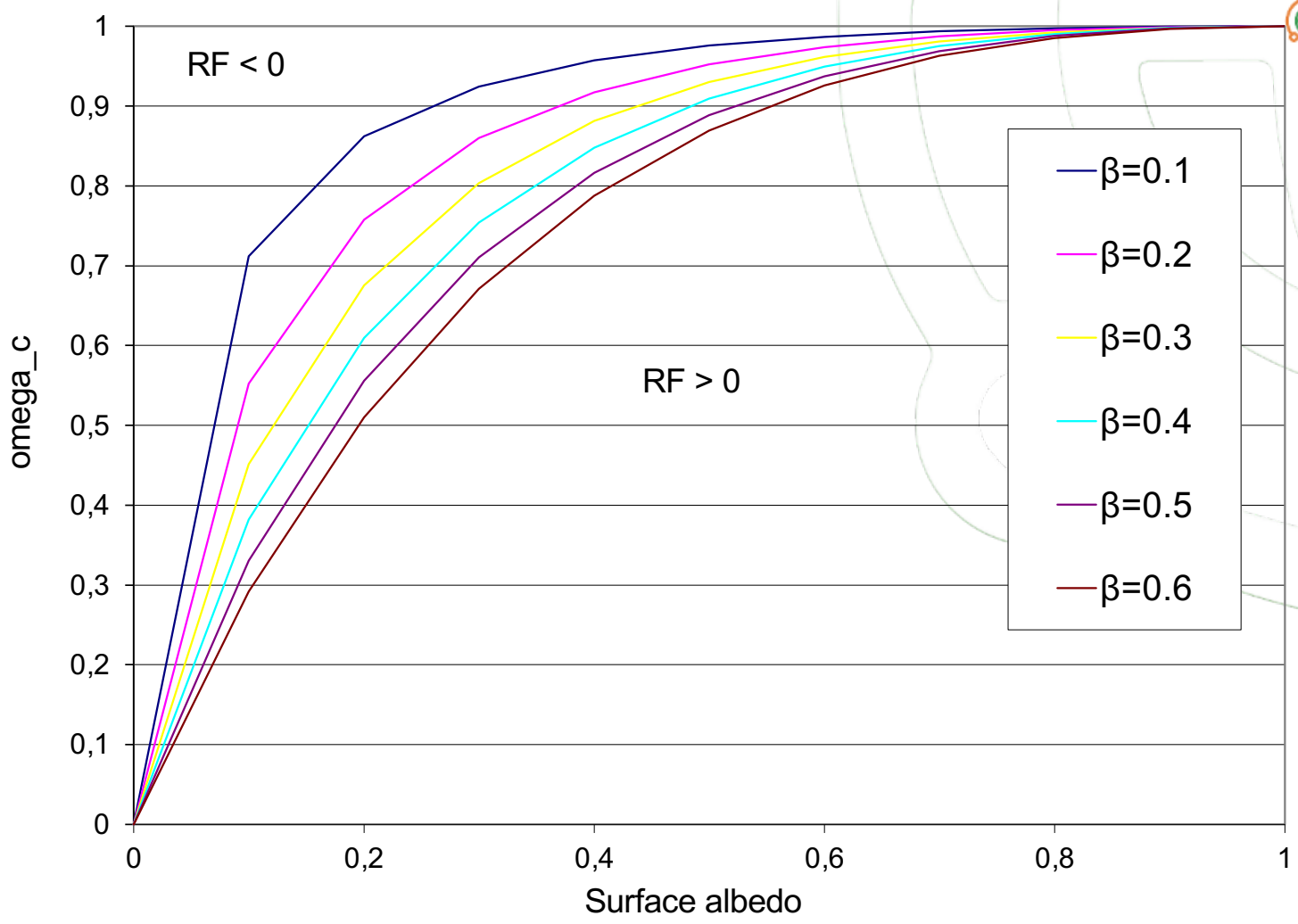
RF < 0
RF > 0
omega_c
Surface albedo
0
0,1
0,2
0,3
0,4
0,5
0,6
0,7
0,8
0,9
1
0,2
0,4
0,6
0,8
β=0.1
β=0.2
β=0.3
β=0.4
β=0.5
β=0.6

Subrahmanyan Chandrasekhar
1910-1995

$$\frac{dL_\lambda}{\beta_\lambda\, ds} = \frac{dL_\lambda(\tau_s,\theta,\varphi)}{d\tau_s(\theta,\varphi)} = -L_\lambda(\tau_s,\theta,\varphi) + \bar{\omega}_0(\tau_s)\tilde{J}_{\lambda,sc}(\tau_s,\theta,\varphi) + [1-\bar{\omega}_0(\tau_s)]\, L^*_\lambda(\tau_s)$$

$$\tilde{J}_{\lambda,sc}(\tau_s,\theta,\varphi) = \frac{1}{4\pi}\int_0^{2\pi} d\varphi' \int_0^{\pi} d\theta' \sin\theta' \, p_\lambda(\theta',\varphi';\theta,\varphi)\, L_\lambda(\tau_s,\theta',\varphi')$$

$$T = \exp(-\tau)$$

$$\tau = \tau_a + \tau_s$$

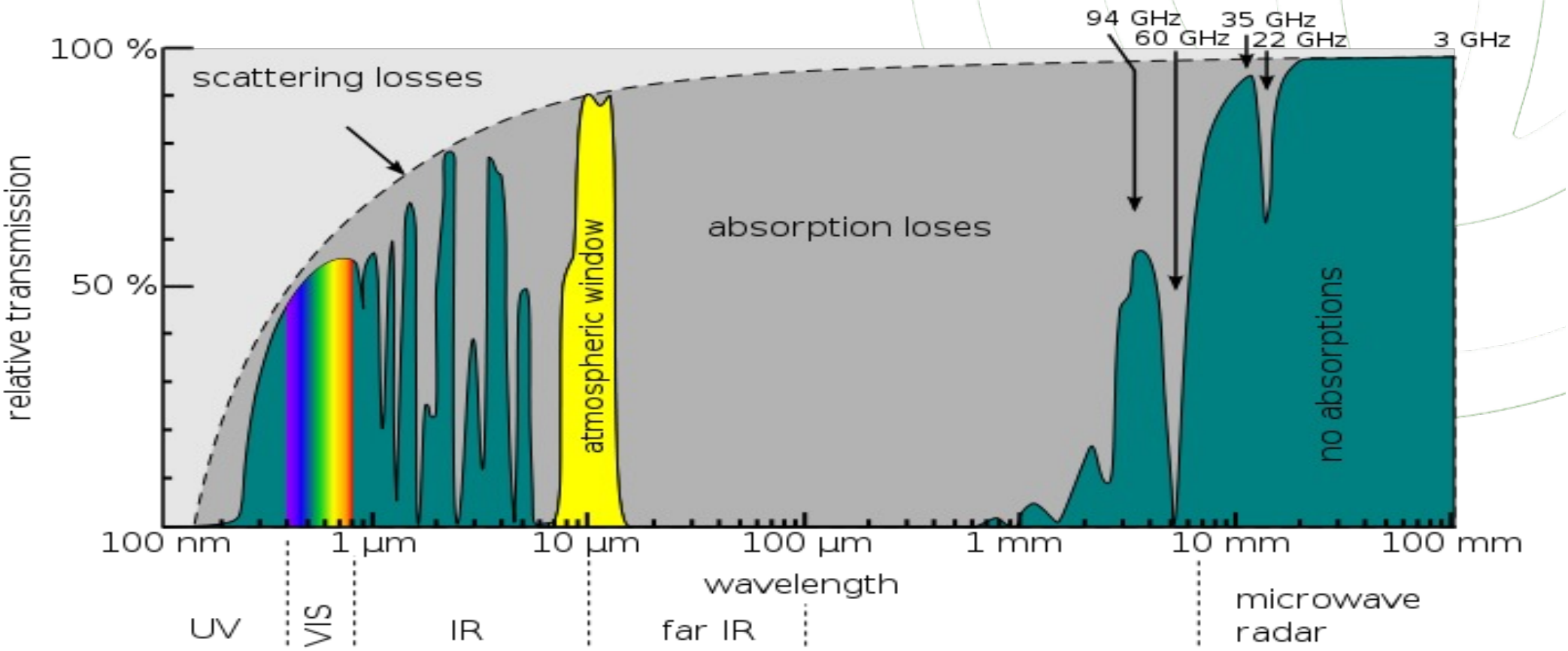

Absorption
Scattering
Emission

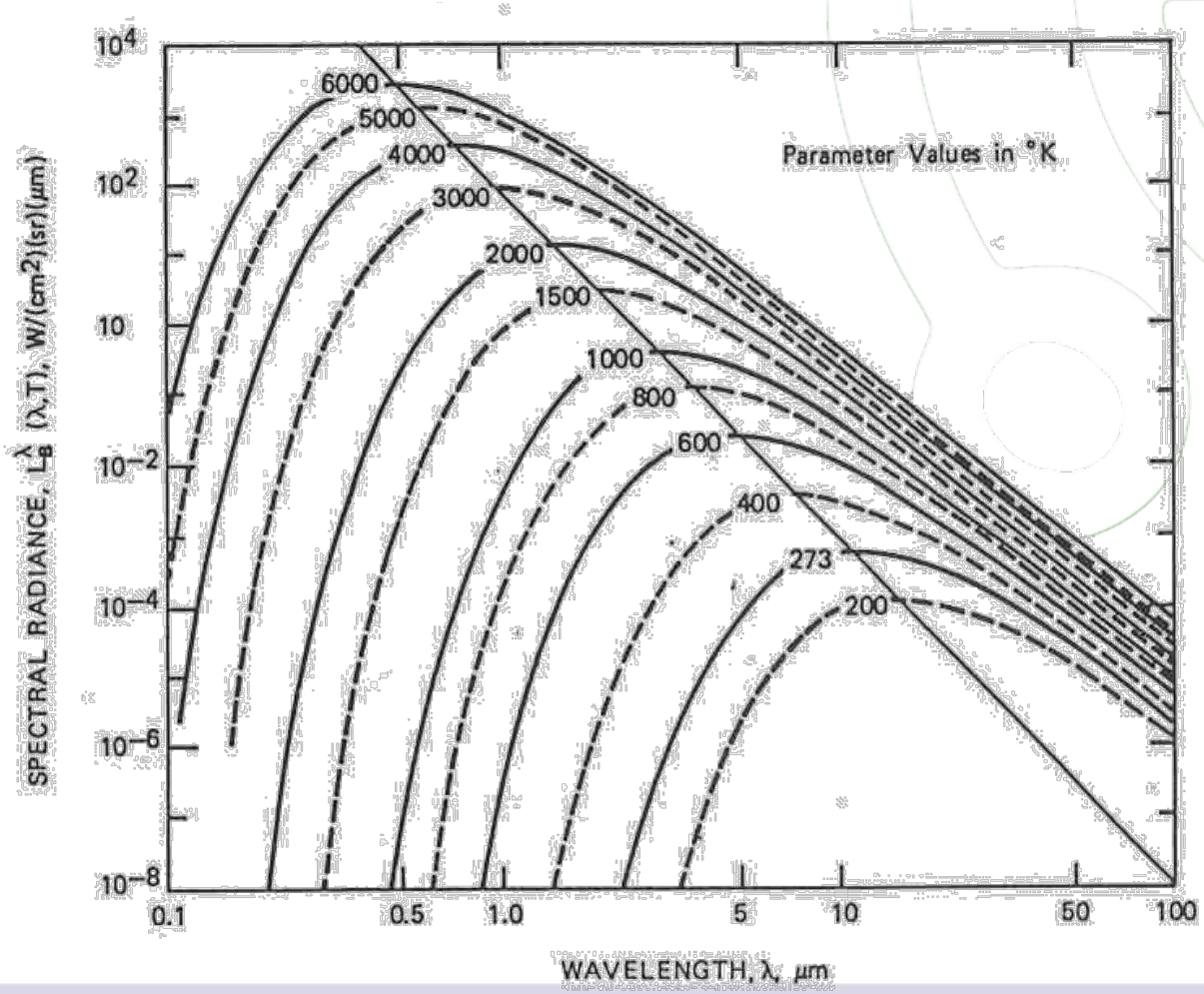
Parameter Values in °K
6000
5000
4000
3000
2000
1500
1000
800
600
400
273
200
SPECTRAL RADIANCE, L_B^{λ} (λ,T), W/(cm²)(sr)(μm)
WAVELENGTH, λ, μm
10^4
10^2
10
10^{-2}
10^{-4}
10^{-6}
10^{-8}
0.1
0.5
1.0
5
10
50
100

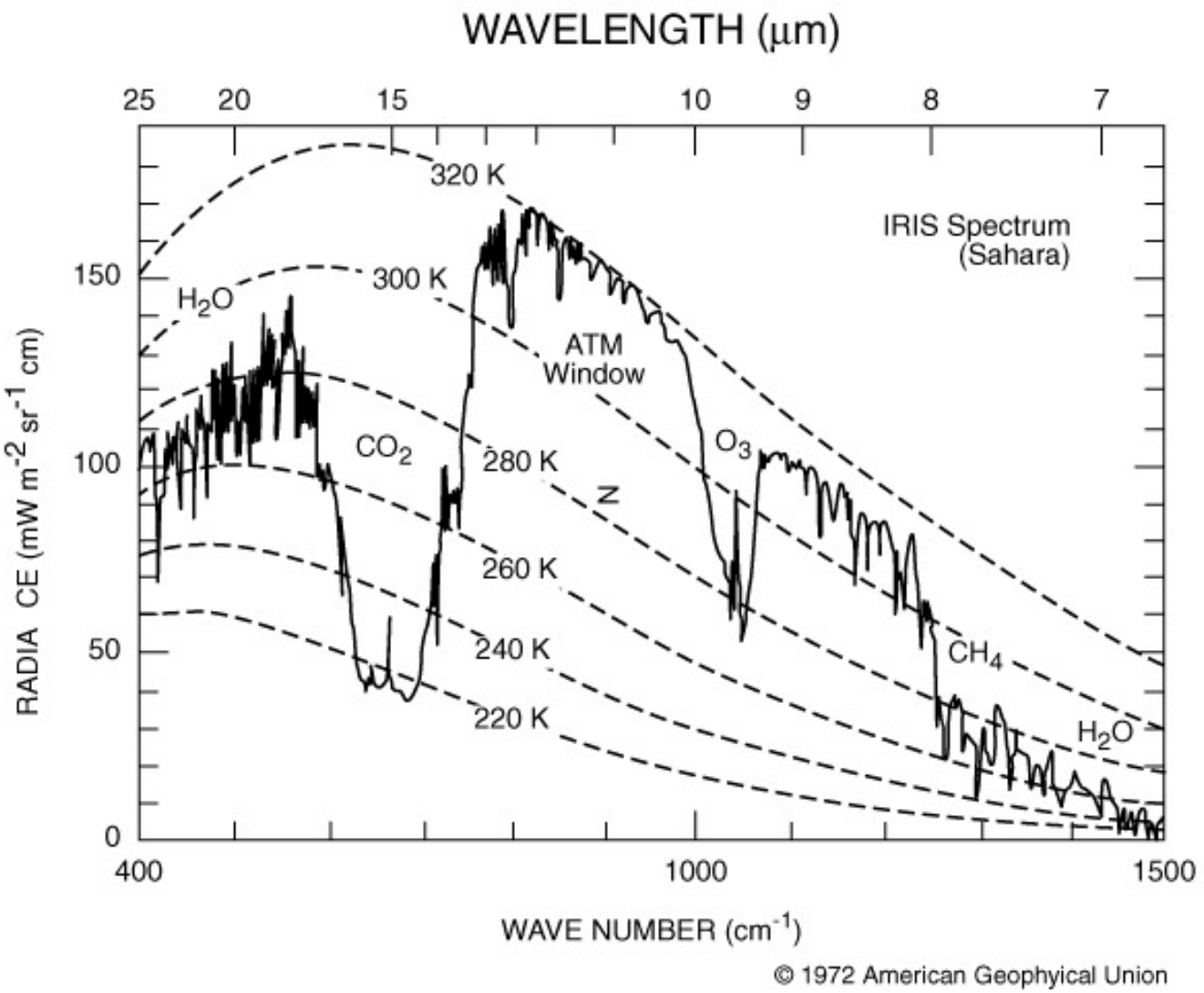
WAVELENGTH (μm)
25
20
15
10
9
8
7
320 K
300 K
280 K
260 K
240 K
220 K
IRIS Spectrum
(Sahara)
H2O
ATM
Window
CO2
O3
CH4
H2O
150
100
50
0
RADIA CE (mW m-2 sr-1 cm)
400
1000
1500
WAVE NUMBER (cm-1)
© 1972 American Geophyical Union

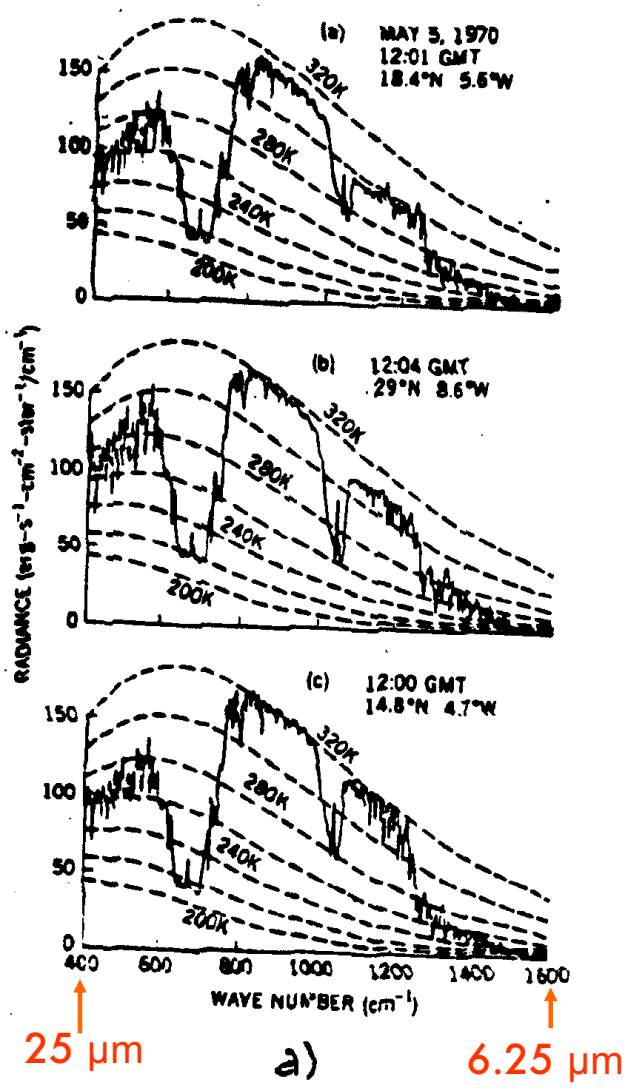
(a) MAY 5, 1970
12:01 GMT
18.4°N 5.6°W
(b) 12:04 GMT
29°N 8.6°W
(c) 12:00 GMT
14.8°N 4.7°W
320K
280K
240K
200K
RADIANCE (erg-s⁻¹-cm⁻²-ster⁻¹/cm⁻¹)
WAVE NUMBER (cm⁻¹)
25 μm
6.25 μm
a)

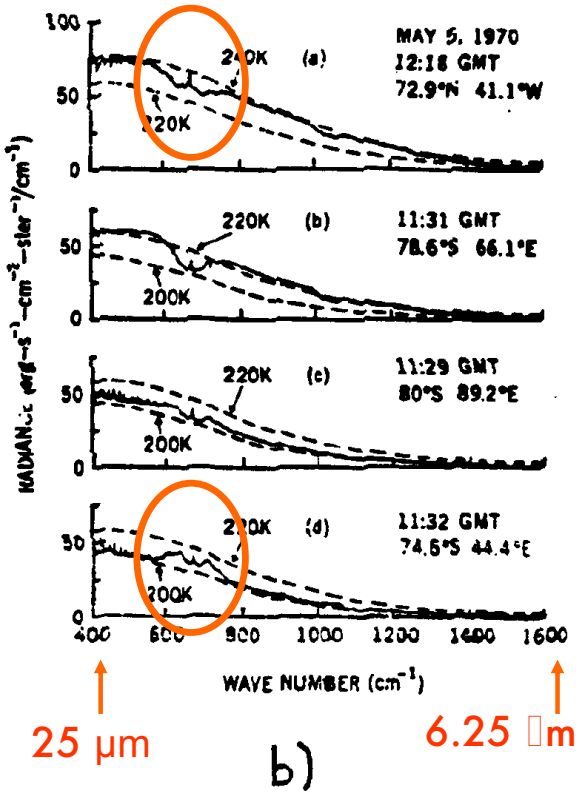
MAY 5, 1970
12:18 GMT
72.9°N 41.1°W
220K
200K
(a)
(b) 11:31 GMT
78.6°S 66.1°E
(c) 11:29 GMT
80°S 89.2°E
(d) 11:32 GMT
74.6°S 44.4°E
WAVE NUMBER (cm⁻¹)
25 μm
6.25 μm
b)

Karl Schwarzschild (1873–1916)

$$L_\lambda = \varepsilon_\lambda B_\lambda(T_S) e^{-\frac{\tau}{cos\theta}} + \int_0^\tau \frac{B_\lambda[T(\tau')] e^{-\frac{\tau-\tau'}{cos\theta}}}{cos\theta} d\tau'$$

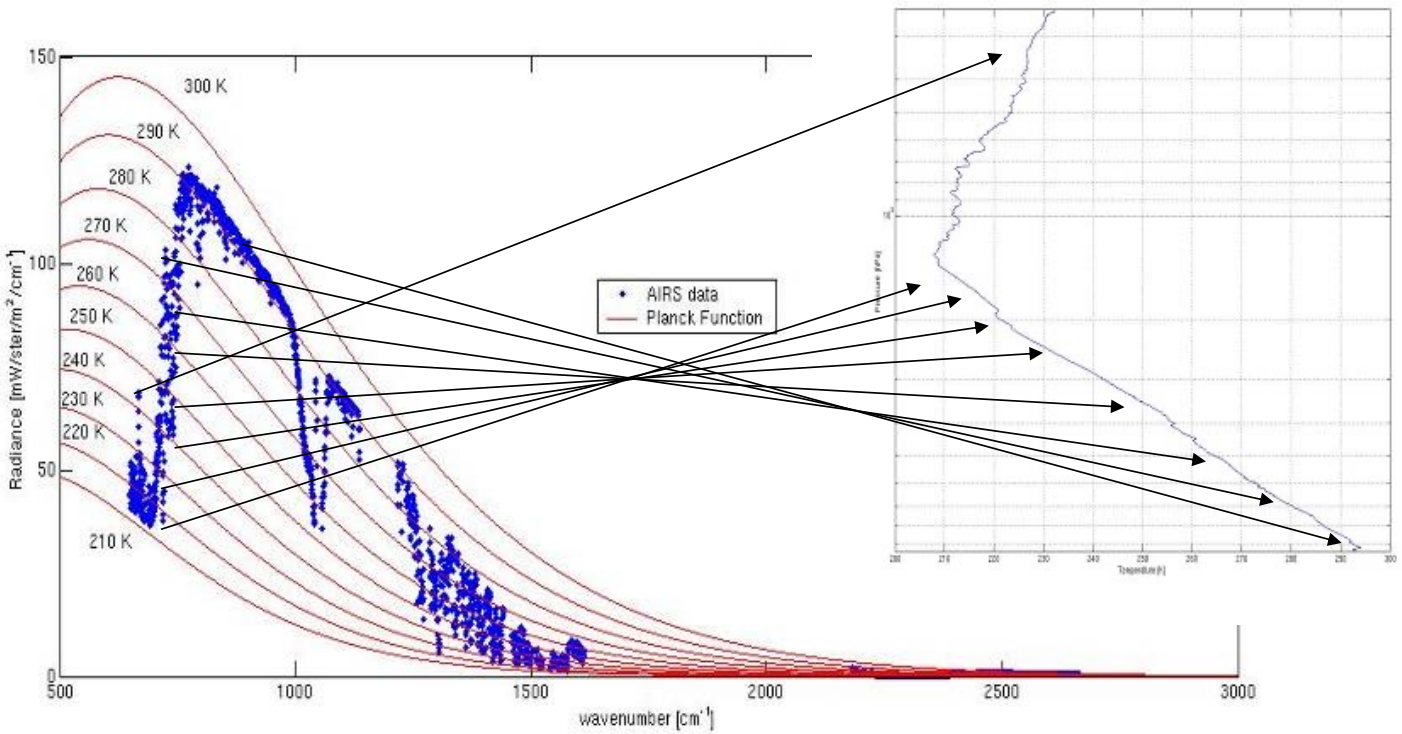

Sampling over rotational bands

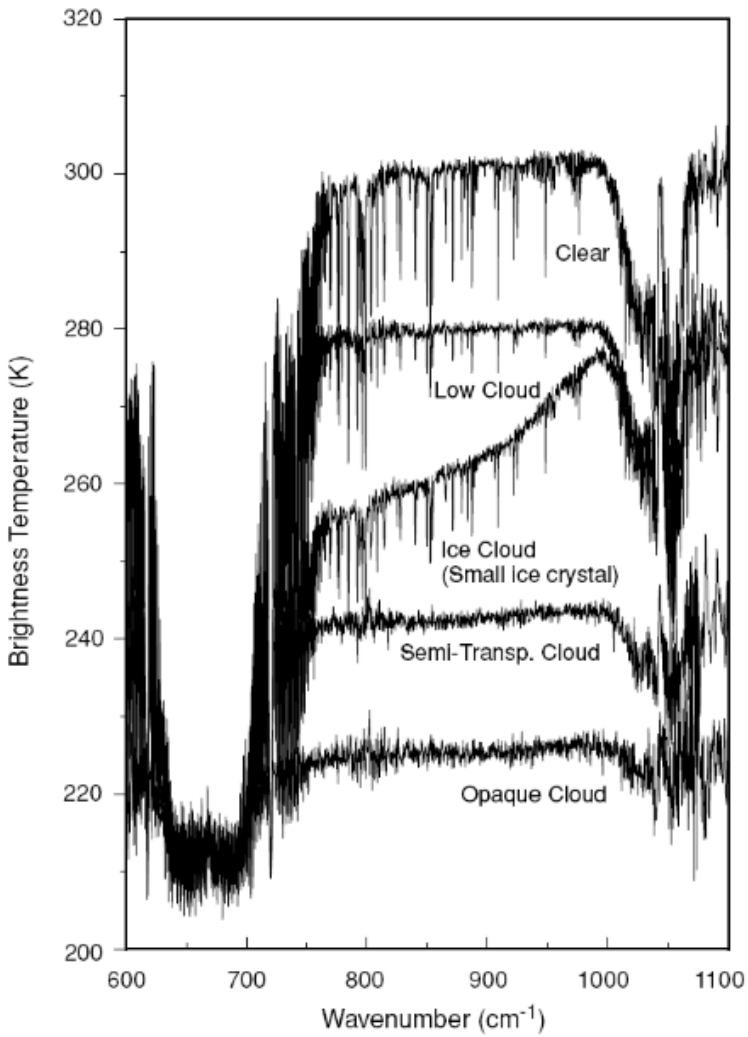

Figure 4.12 Spectra of brightness temperature observed from a high spectral resolution infrared spectrometer from the high-flying ER-2 aircraft over a domain, 37.1°–37.4° N, 95.0°–95.3° W, on April 21, 1996, indicating wavelength-dependent window brightness temperature changes according to various cloud types. The type of cloud indicated for each spectrum is identified from the Cloud Lidar System aboard the ER-2 (data taken from Smith *et al.*, 1998).

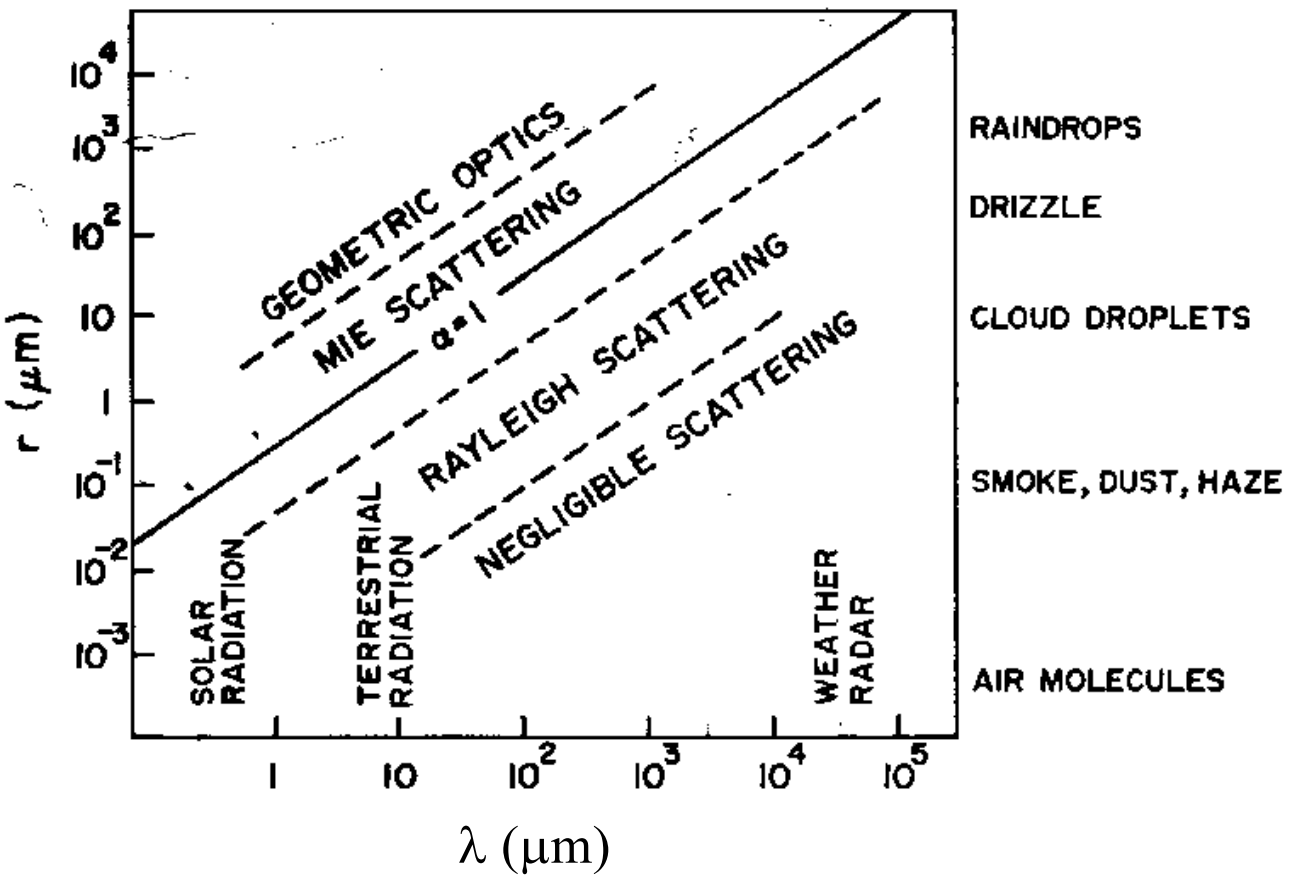
r (μm)
10⁴
10³
10²
10
1
10⁻¹
10⁻²
10⁻³
GEOMETRIC OPTICS
MIE SCATTERING
α=1
RAYLEIGH SCATTERING
NEGLIGIBLE SCATTERING
SOLAR RADIATION
TERRESTRIAL RADIATION
WEATHER RADAR
1
10
10²
10³
10⁴
10⁵
λ (μm)
RAINDROPS
DRIZZLE
CLOUD DROPLETS
SMOKE, DUST, HAZE
AIR MOLECULES

Di Biagio et al., 2014

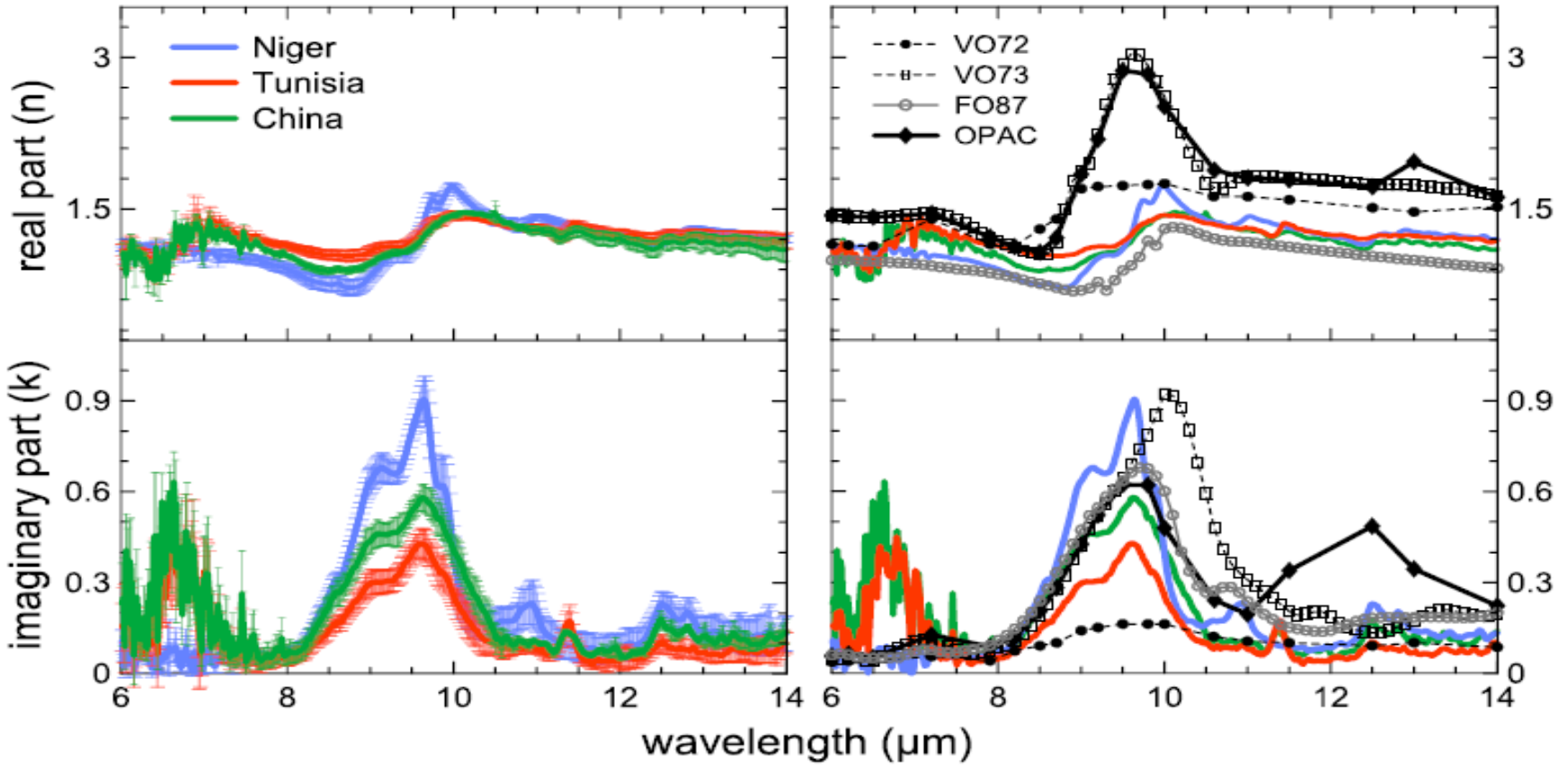

Subrahmanyan Chandrasekhar
1910-1995

$$\frac{dL_\lambda}{\beta_\lambda\, ds} = \frac{dL_\lambda(\tau_s,\theta,\varphi)}{d\tau_s(\theta,\varphi)} = -L_\lambda(\tau_s,\theta,\varphi) + \bar{\omega}_0(\tau_s)\tilde{J}_{\lambda,sc}(\tau_s,\theta,\varphi) + [1-\bar{\omega}_0(\tau_s)]\, L^*_\lambda(\tau_s)$$

$$\tilde{J}_{\lambda,sc}(\tau_s,\theta,\varphi) = \frac{1}{4\pi}\int_0^{2\pi} d\varphi' \int_0^{\pi} d\theta' \sin\theta' \, p_\lambda(\theta',\varphi';\theta,\varphi)\, L_\lambda(\tau_s,\theta',\varphi')$$

Lidar, eventually

IR0000032 – ITINERIS, Italian Integrated Environmental Research Infrastructures System
(D.D. n. 130/2022 - CUP B53C22002150006) Funded by EU - Next Generation EU PNRR-Mission 4 "Education and Research" - Component 2: "From research to business" - Investment 3.1: "Fund for the realisation of an integrated system of research and innovation infrastructures"

Finanziato dall'Unione europea NextGenerationEU
Ministero dell'Università e della Ricerca
Italiadomani

Giorgio Fiocco
1931-2012

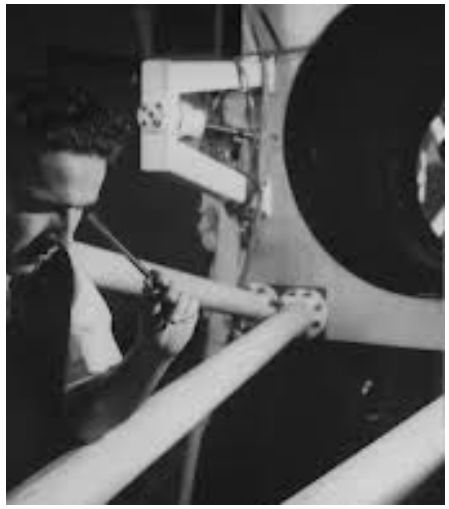

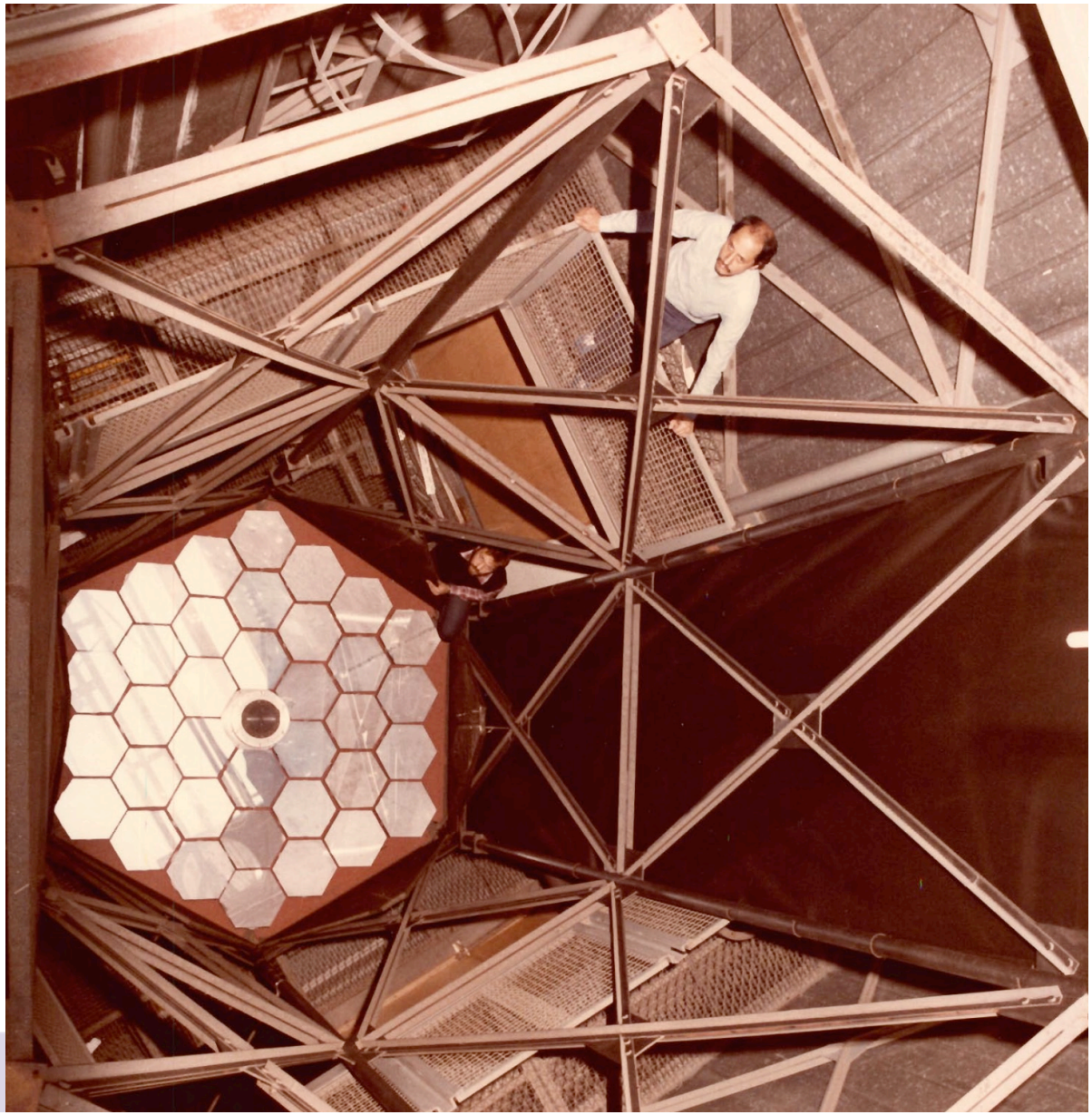

LETTERS TO THE EDITOR

ASTROPHYSICS

Optical Echoes from the Moon

EXPERIMENTS have been conducted to focus pulsed optical radiation on to the surface of the Moon and to detect the echoes.

A ruby optical maser radiating pulses of approximately 50 joules energy, 0·5-msec. duration, at 6934 Å. was used as the source. The transmitting optical system included a Cassegrainian telescope of 12-in. diameter. The echoes were received on a Cassegrainian telescope of 48-in. diameter, passed through an interference filter of 7 Å. band-width and were detected with a photomultiplier tube of spectral response type *S*-20, cooled to liquid nitrogen temperature. The field of view of the receiving telescope

Fundamental Band of the Quadrupole Spectrum of the Hydrogen Molecule

THE application of interferometric techniques to astrophysical problems in the near infra-red shows considerable promise. The abundance of hydrogen in planetary atmospheres is probably of major importance.

Herzberg[1] observed the 2–0 and 3–0 bands of the quadrupole spectrum of hydrogen using pressures of 10 atmospheres and optical paths of 10–55 km. atmospheres. In addition, an induced dipole spectrum of hydrogen has been found by Chisholm, MacDonald, Crawford and Welsh[2] by making measurements in the pressure-range of hundreds to thousands of atmospheres.

We have observed the 1–0 band of the quadrupole

Observations of the Aerosol Layer at 20 km by Optical Radar

G. FIOCCO AND G. GRAMS

Massachusetts Institute of Technology

25 March 1964

The existence of an aerosol layer at an altitude of about 20 km has been well established by optical techniques (Gruner, 1942; Bigg, 1956; Volz and Goody, 1962) and by direct sampling from balloons and aircraft (see, for example, Junge and Manson, 1961). Preliminary results from observation of this layer with an optical radar are reported in this note.

The optical radar system, which uses a pulsed ruby laser as a source of radiation, presents some changes and improvements over the instrumentation previously utilized (Fiocco and Smullin, 1963; Fiocco and Colombo, 1964). The system consists of a Q-switched ruby laser, a transmitting telescope to collimate the outgoing beam, a receiving telescope of the Dahl-Kirkham type with 40-cm aperture, and a detector incorporating narrow band interference filters, a mechanical shutter, and a photomultiplier of S-20 type. The laser emits a pulse of approximately one-half joule with a wavelength of 0.694 micron and a duration of 50 nanoseconds. The mechanical shutter is incorporated into the detector to prevent exposing the photomultiplier to the strong echoes from short distances.

The intensity of the received signal displayed as a function of height is related to the collective backscattering radar cross section of the atmospheric constituents. When the component due to molecular scattering is separately evaluated, anomalous contributions due to the presence of aerosols, in some cases, can be isolated. A profile of the relative intensity of the echoes from altitudes of 14 to 25 km is presented in Fig. 1, curve *a*. This profile has been obtained by averaging 20 successive traces to eliminate fluctuations; the traces

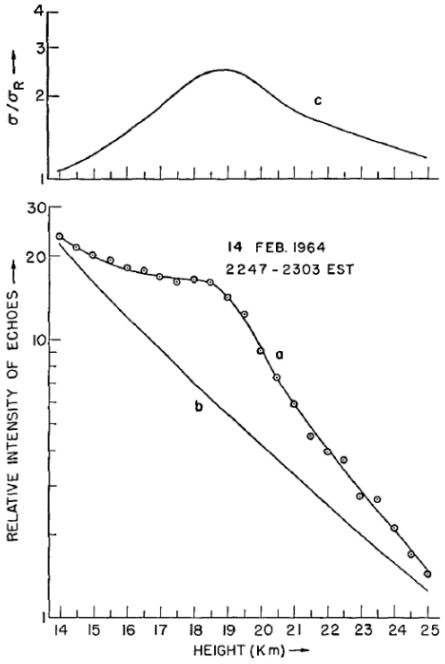

FIG. 1. Curve *a*: observed relative intensity of echoes from a

Measurement of Aerosol Motion and Wind Velocity in the Lower Troposphere by Doppler Optical Radar

G. BENEDETTI-MICHELANGELI, F. CONGEDUTI AND G. FIOCCO[1]

European Space Research Institute (ESRIN), Frascati (Rome), Italy

(Manuscript received 19 October 1971, in revised form 6 March 1972)

ABSTRACT

An optical radar has been used to measure the radial wind velocity component in the lower troposphere by detecting interferometrically the bulk Doppler shift affecting the echoes from atmospheric aerosols. The measurements, carried out at night, have basically utilized a highly coherent single-frequency Ar^+ laser in the transmitter, and a small telescope, a scanning spherical Fabry-Perot interferometer, and a photon counting system in the receiver.

1. Introduction

Continuing our investigations on the use of optical radars to measure atmospheric properties, we wish to report preliminary measurements of wind velocity in

LETTERS TO NATURE

Measurement of Temperature and Aerosol to Molecule Ratio in the Troposphere by Optical Radar

WE wish to describe preliminary optical radar measurements of atmospheric temperature and aerosol to molecule ratio. Optical radar can radiate pulses of highly monochromatic laser light and resolve the frequency spectrum of the light d by atmospheric constituents. Because of the ounts of Doppler broadening which affect the e echoes from aerosols and molecules, it is possible between molecules. This is possible when the ratio of the wavelength to collision mean free path is small, which is the case in the upper atmosphere. At higher pressures, pressure fluctuations modify the spectrum by introducing two displaced components (the Brillouin doublet). At tropospheric heights the peaks are not expected to be distinguishable, but there should be a broadening of the spectrum and slight modifications in its shape. Yip and Nelkin[2] have computed spectral profiles for scattering from a monoatomic gas for various values of the parameter y, a measure of the ratio of the wavelength to the collision mean free path. From their graphs we have evaluated

Atmospheric Environment Vol. 8, pp. 793–799. Pergamon Press 1974. Printed in Great Britain.

DETERMINATION OF VERTICAL EDDY DIFFUSION PARAMETERS BY DOPPLER OPTICAL RADAR

G. BENEDETTI-MICHELANGELI and F. CONGEDUTI

CNR-LPS, Elettrofisica Atmosferica, c.p. 27, Frascati, Italy

and

G. FIOCCO

Istituto di Fisica, Università, Firenze, Italy

(*First received* 25 *June* 1973 *and in final form* 11 *December* 1973)

Abstract—Simultaneous measurements of aerosol concentration and vertical wind velocity by Doppler optical radar permit the determination of the vertical eddy flux of aerosols and of the diffusion coefficient. Results of experiments are presented.

INTRODUCTION

In a previous paper (Benedetti-Michelangeli, Congeduti and Fiocco, 1972) we reported measurements of aerosol motion and wind velocity in the lower troposphere by Doppler optical radar. The measurements relied on the interferometric analysis of the radial

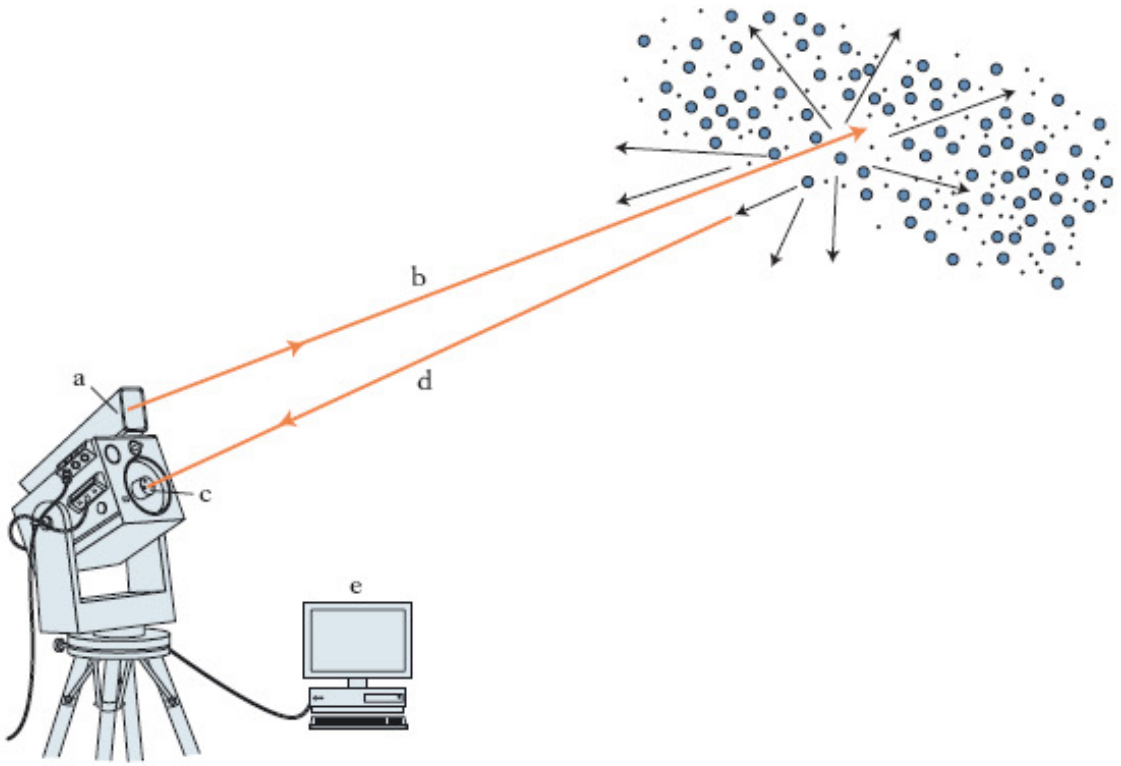
a
b
c
d
e

$$T = \exp(-\tau)$$

$$\tau = \tau_a + \tau_s$$

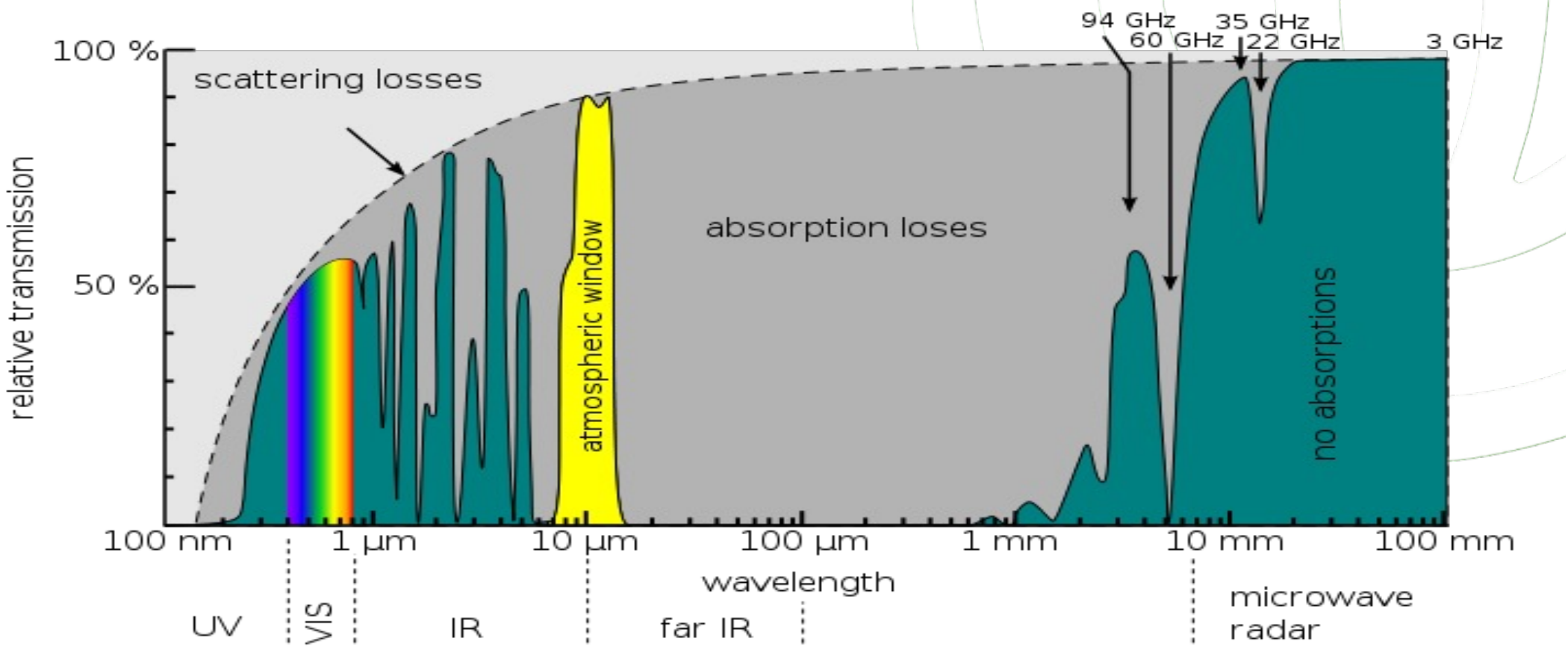

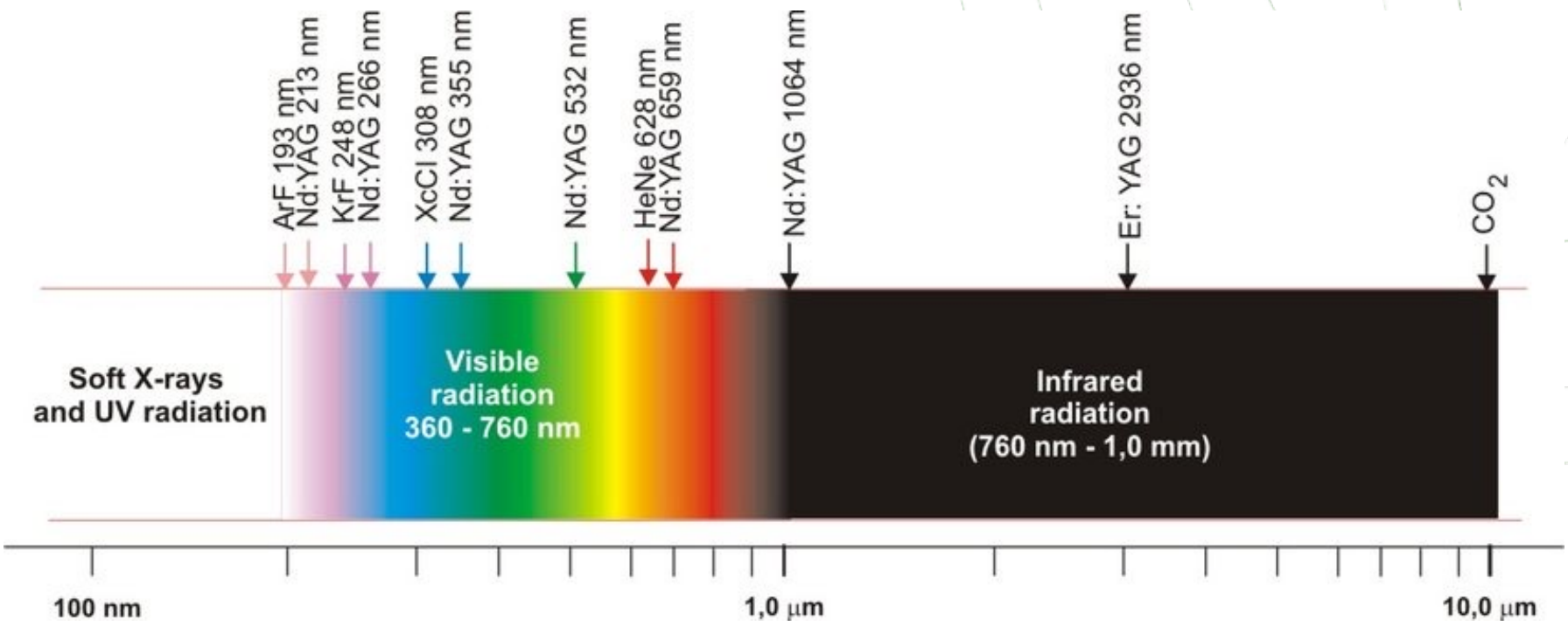
ArF 193 nm
Nd:YAG 213 nm
KrF 248 nm
Nd:YAG 266 nm
XcCl 308 nm
Nd:YAG 355 nm
Nd:YAG 532 nm
HeNe 628 nm
Nd:YAG 659 nm
Nd:YAG 1064 nm
Er: YAG 2936 nm
CO_2
Soft X-rays
and UV radiation
Visible
radiation
360 - 760 nm
Infrared
radiation
(760 nm - 1,0 mm)
100 nm
1,0 μm
10,0 μm

$x=2\pi r/\lambda$

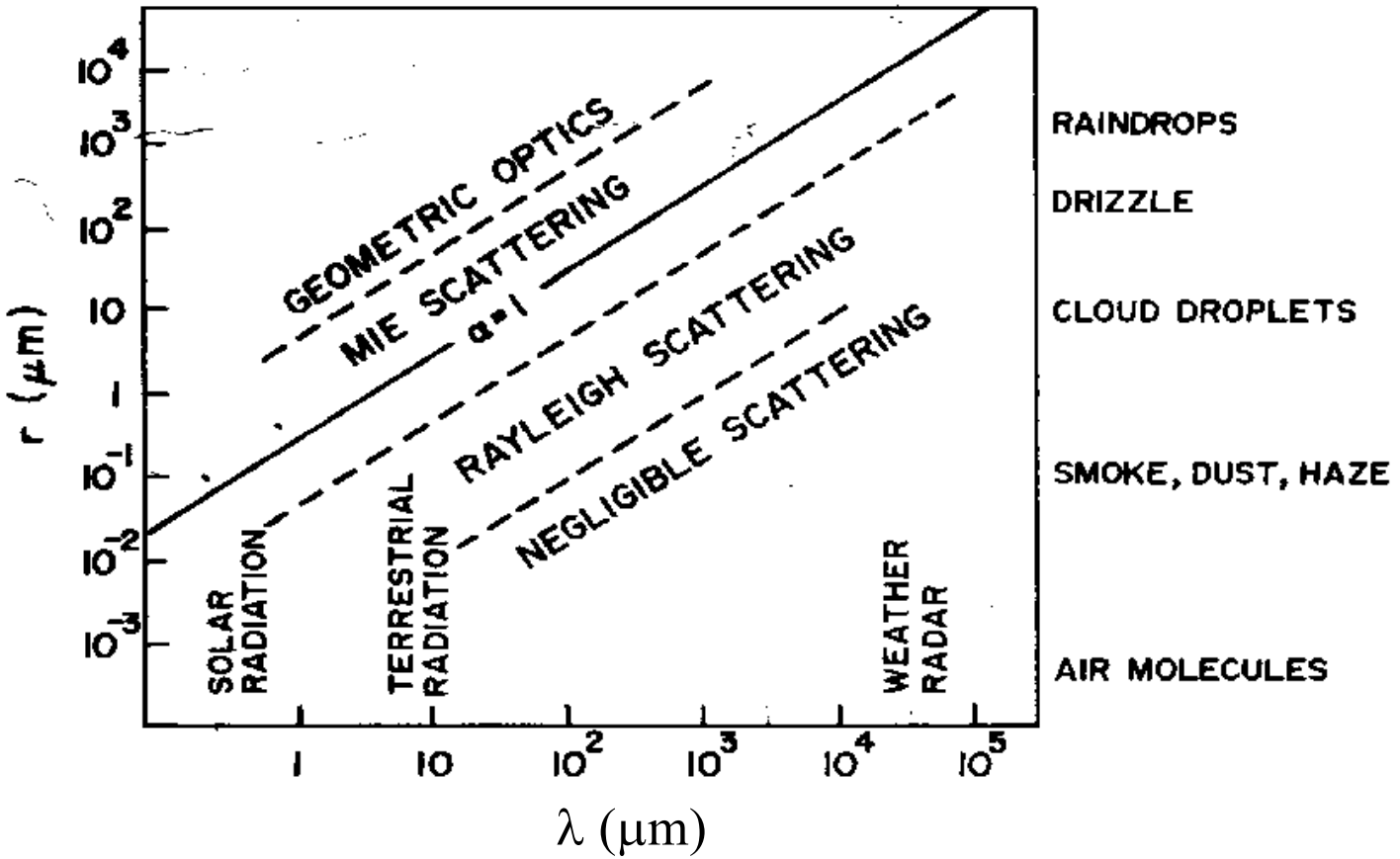

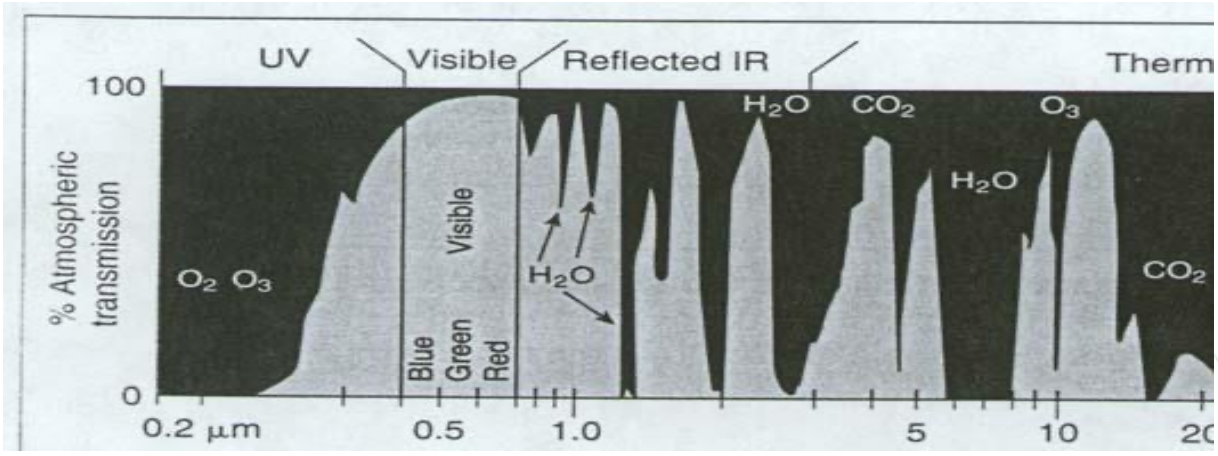
UV
Visible
Reflected IR
Therm
100
0
% Atmospheric transmission
O_2 O_3
Blue
Green
Red
Visible
H_2O
H_2O
CO_2
O_3
H_2O
CO_2
0.2 µm
0.5
1.0
5
10

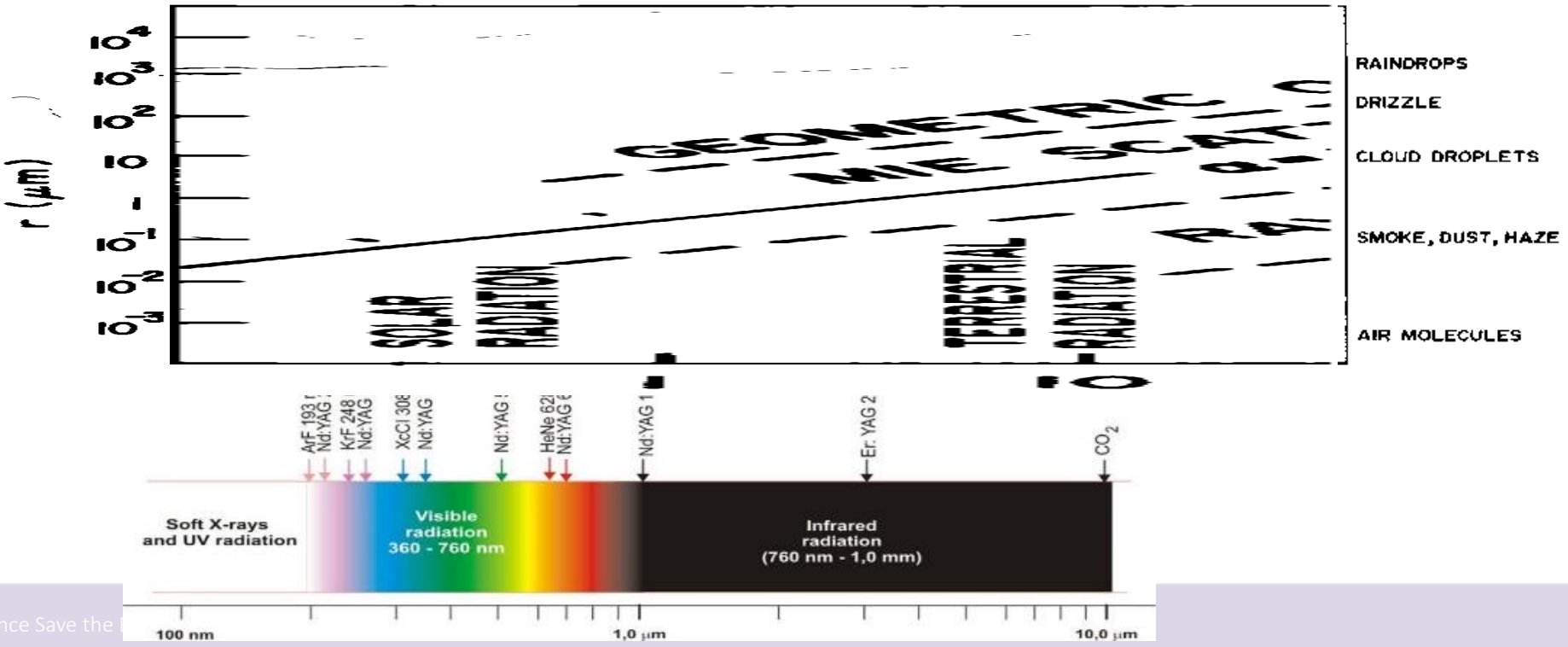
r (µm)
GEOMETRIC
MIE SCATT
SOLAR RADIATION
TERRESTRIAL RADIATION
RAINDROPS
DRIZZLE
CLOUD DROPLETS
SMOKE, DUST, HAZE
AIR MOLECULES
ArF: 193 r
Nd:YAG
KrF: 248
Nd:YAG
XeCl: 308
Nd:YAG
Nd:YAG
HeNe: 62
Nd:YAG
Nd:YAG 1
Er: YAG 2
CO_2
Soft X-rays and UV radiation
Visible radiation 360 - 760 nm
Infrared radiation (760 nm - 1,0 mm)
100 nm
1,0 µm
10,0 µm

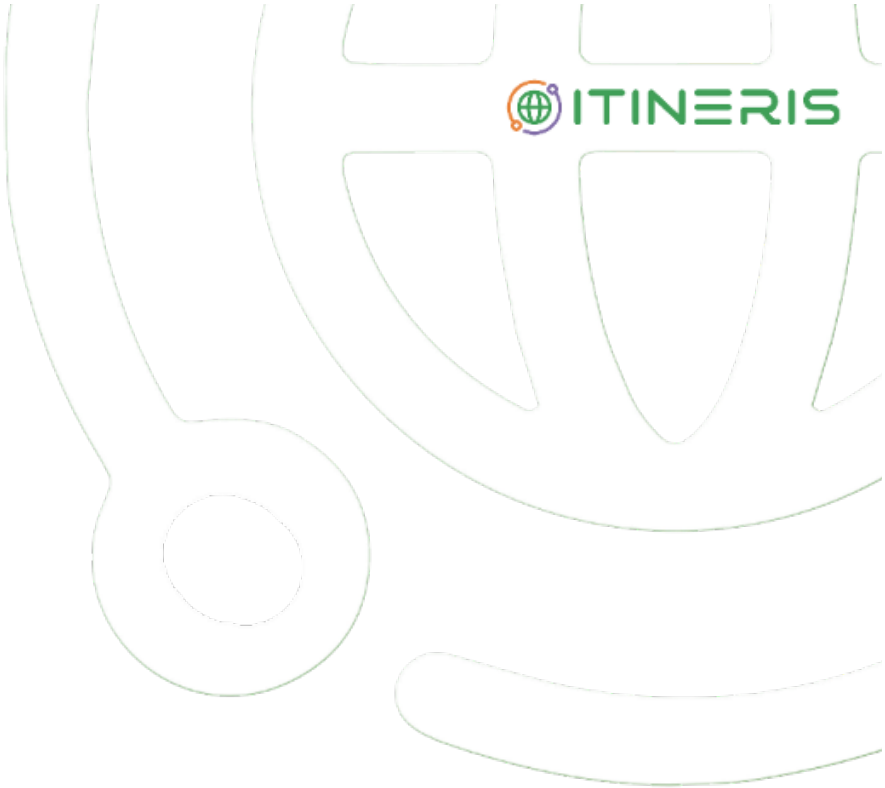
ITINERIS

Incoherent elastic backscattering lidar

No information from the phase of the signal

Emission and detection at the same wavelength

Incoherent «broadband» elastic backscattering lidar

Outside of gas absorption lines: aerosol/clouds

single/multi wavelengths

depolarization

without aerosol: density, temperature

In/out of absorption lines (differential absorption): gas concentrations

- Incoherent «narrowband» elastic backscattering lidar
  - HSRL: aerosol
  - Doppler shift: wind velocity (*)
  - line shape: temperature

(*) not exactly the same wavelength, but elastic scattering processes

Incoherent anelastic backscattering lidar (1)

No information from the phase of the signal

Emission and detection at different wavelengths

Incoherent «broadband» anelastic backscattering lidar

Raman: aerosol extinction; profile of specific gases

Fluorescence: aerosol typing (vegetation, ocean properties)

Incoherent «narrowband» anelastic backscattering lidar

Raman: temperature profile

Incoherent anelastic backscattering lidar (2)

No information from the phase of the signal

Emission and detection at the same wavelength, in correspondance with an atomic energy level transition (resonance scattering)

- Incoherent «broadband» anelastic backscattering lidar

  Resonance scattering: concentration profile for Na, Ca, Ca+, Fe, K, ...

- Incoherent «narrowband» anelastic backscattering lidar

  Resonance scattering, hyperfine structure: temperature profile

- **Coherent elastic backscattering lidar**
  - Information in the phase of the signal
  - Emission and detection at (almost) the same wavelength, elastic scattering
- Coherent «narrowband» elastic backscattering lidar
  - Temperature profile, aerosol profile, wind

- The lidar equation in the simplest case: single wavelength, vertically pointing elastic backscattering lidar, no aerosols

90

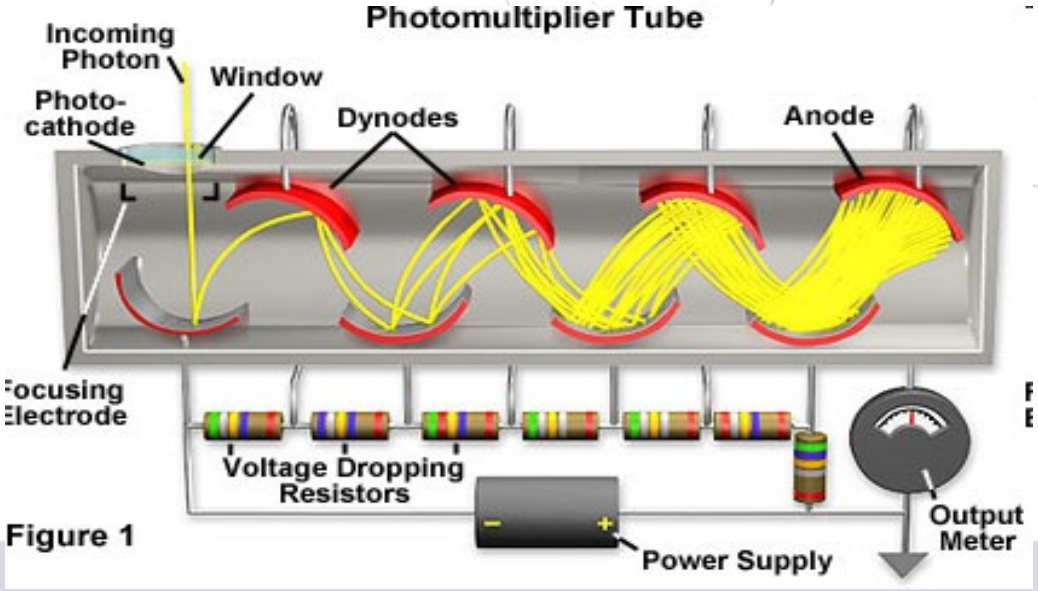
Photomultiplier Tube
Incoming Photon
Window
Photo-cathode
Dynodes
Anode
Focusing Electrode
Voltage Dropping Resistors
Output Meter
Power Supply

Figure 1

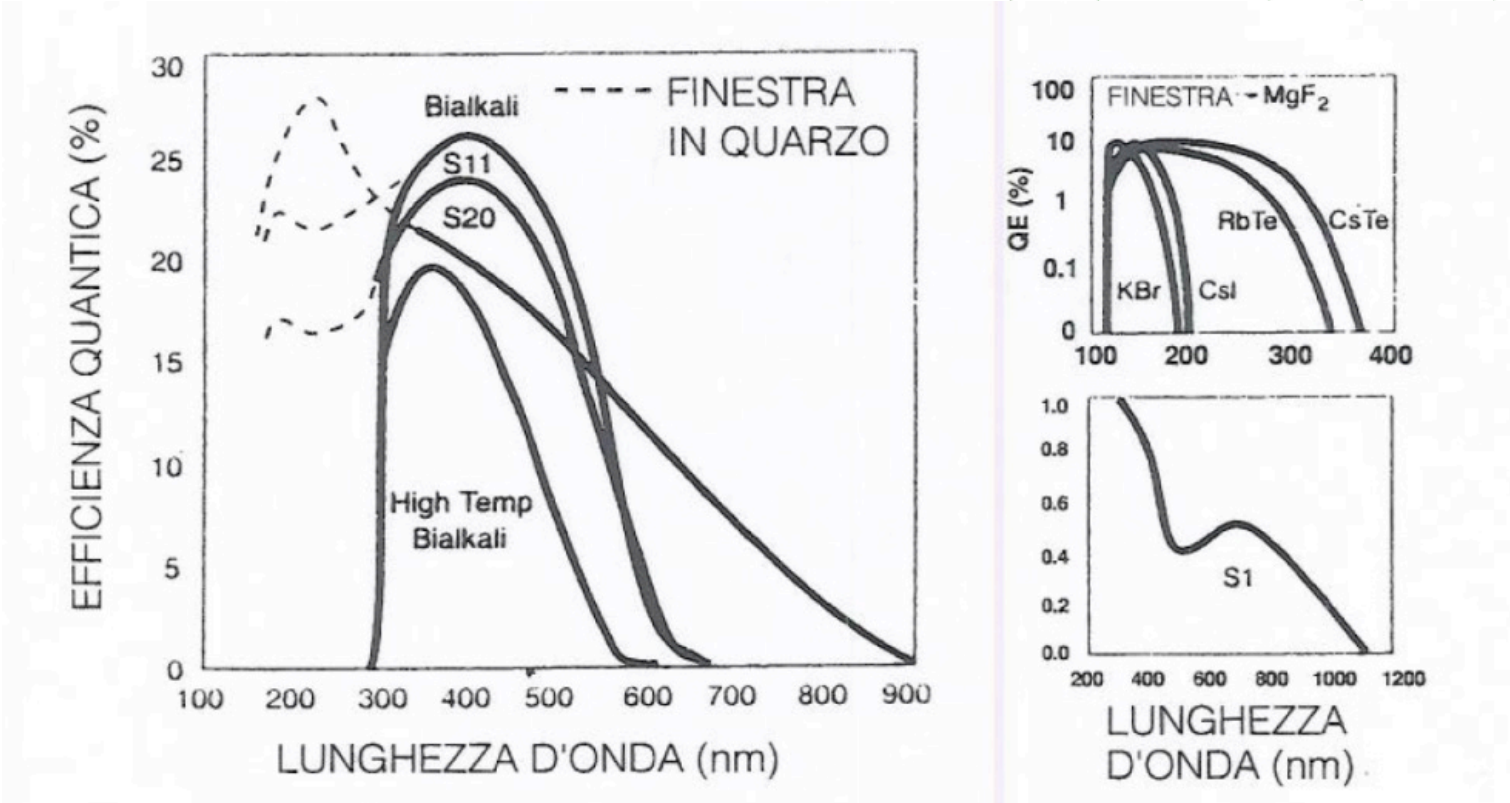
EFFICIENZA QUANTICA (%)
30
25
20
15
10
5
0
Bialkali
FINESTRA
IN QUARZO
S11
S20
High Temp
Bialkali
100
200
300
400
500
600
700
800
900
LUNGHEZZA D'ONDA (nm)
QE (%)
100
10
1
0.1
0
FINESTRA - MgF_2
RbTe
CsTe
KBr
CsI
100
200
300
400
1.0
0.8
0.6
0.4
0.2
0.0
S1
200
400
600
800
1000
1200
LUNGHEZZA
D'ONDA (nm)

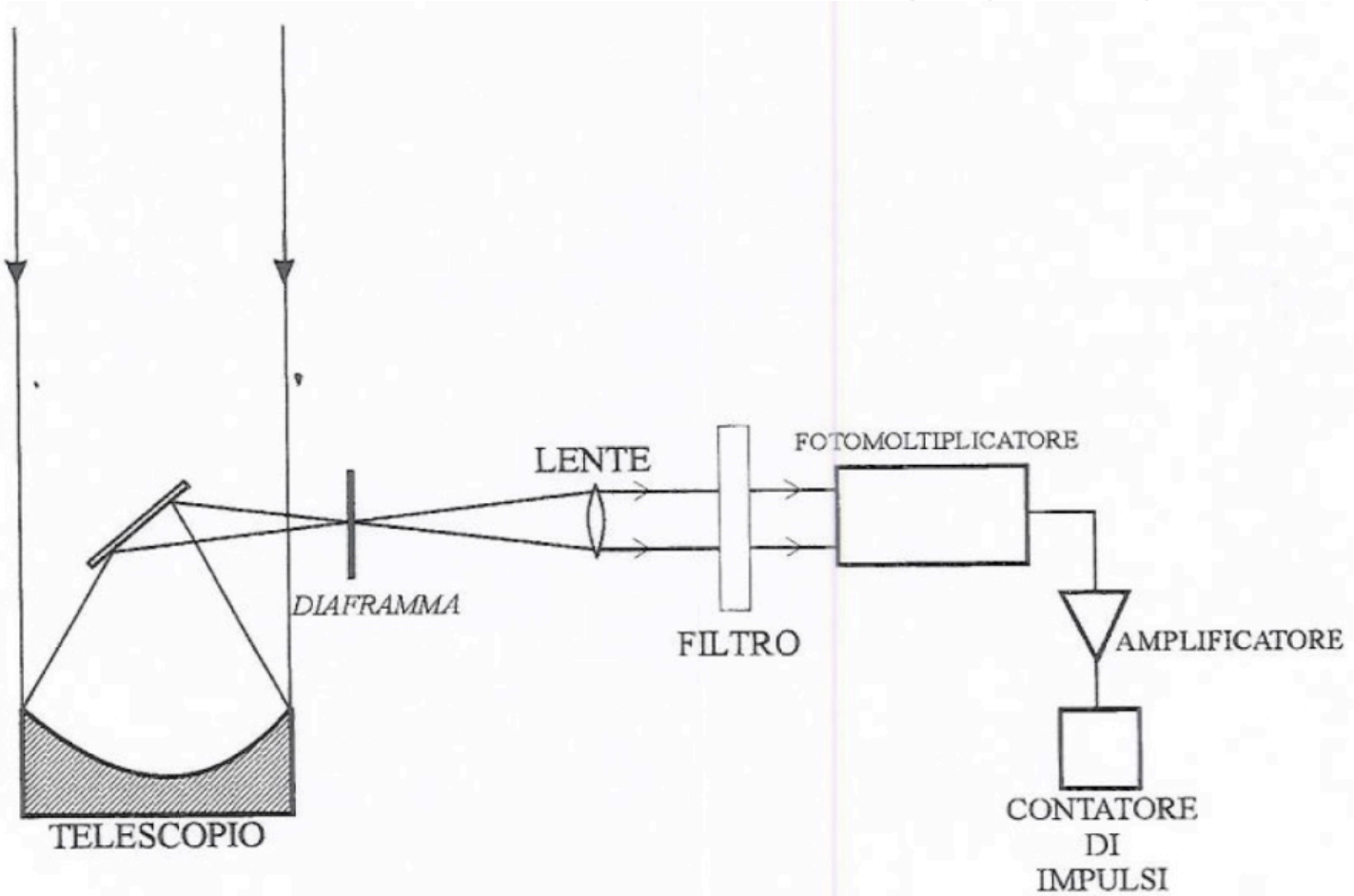
LENTE
FOTOMOLTIPLICATORE
DIAFRAMMA
FILTRO
AMPLIFICATORE
TELESCOPIO
CONTATORE
DI
IMPULSI

100

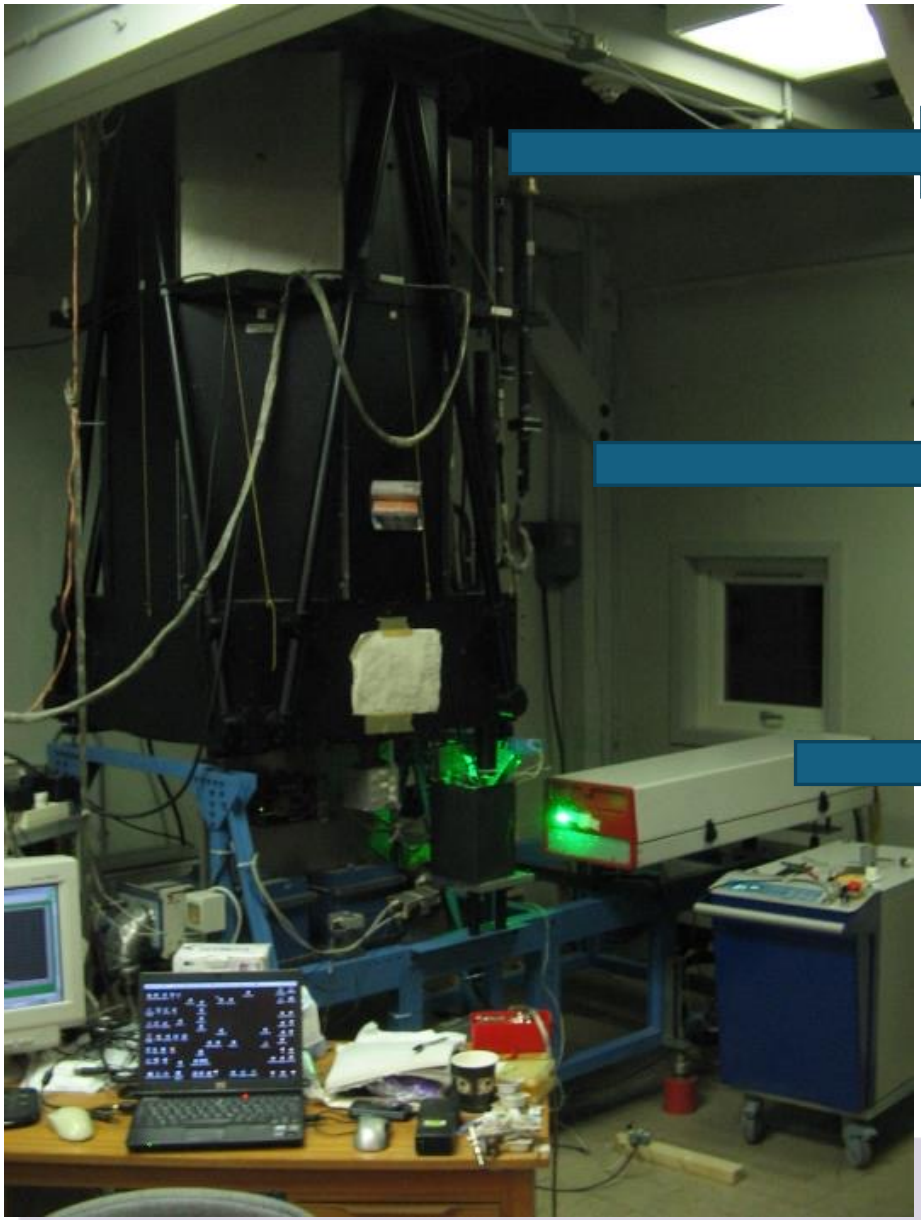

Ø 80 cm telescope for high troposphere and middle atmosphere

small refractive telescopes for the troposphere

Nd:YAG laser (355, 532, and 1064 nm)

The Thule High Arctic Atmospheric Observatory

THAAO (76.52° N, 68.76° W, 220 m amsl) within the Pituffik Space Base.

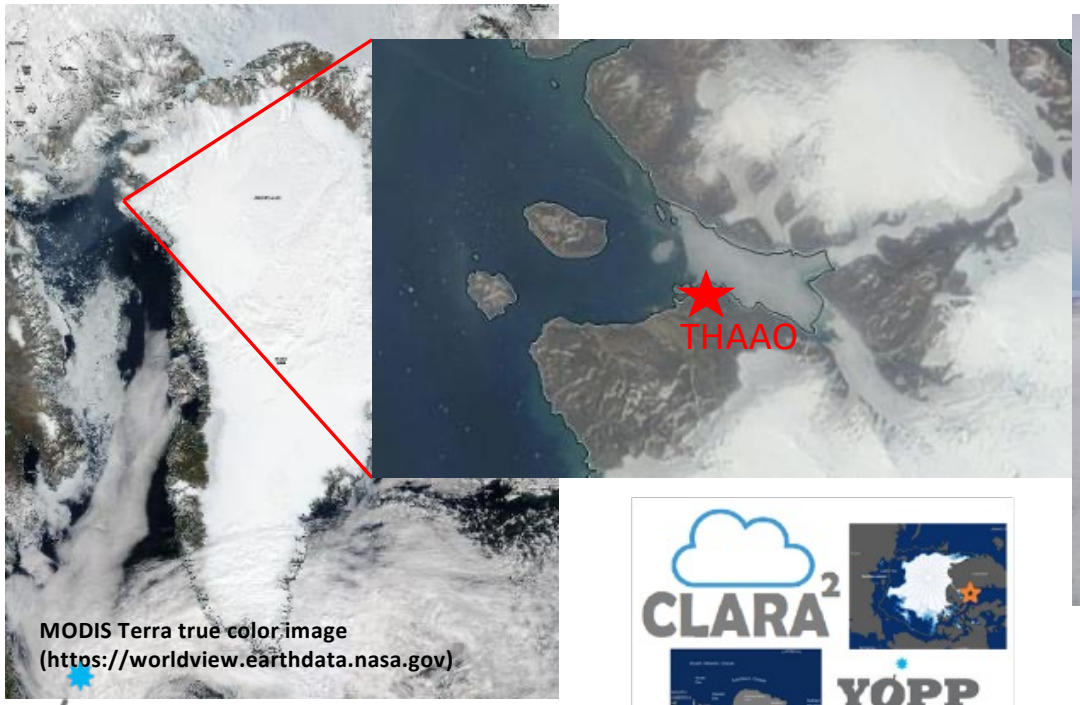

ARCSIX
Arctic Radiation-Cloud-Aerosol-Surface Interaction Experiment

YOPP YEAR OF POLAR PREDICTION

SEANA

Shipping Emissions in the Arctic and North Atlantic atmosphere

CLARA²

YOPP YEAR OF POLAR PREDICTION

ECAPAC

https://www.thuleatmos-it.it

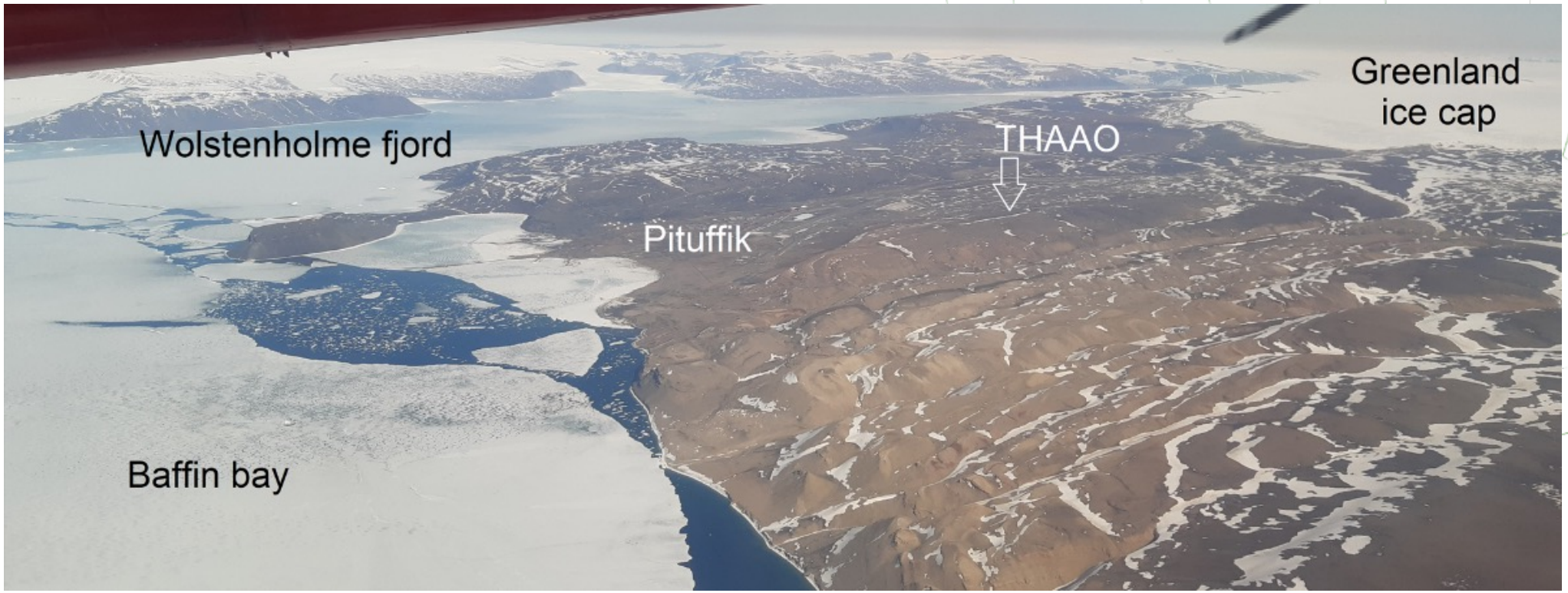
Wolstenholme fjord
Pituffik
THAAO
Greenland
ice cap
Baffin bay


Building 1971 with
active/passive radiation sensors,
PM samplers, spectrometers, ...
Balloon house
for radiosonde
launches
MRR-2
Disdrometer
Weather station
Snow level sensor
Precipitation gauge

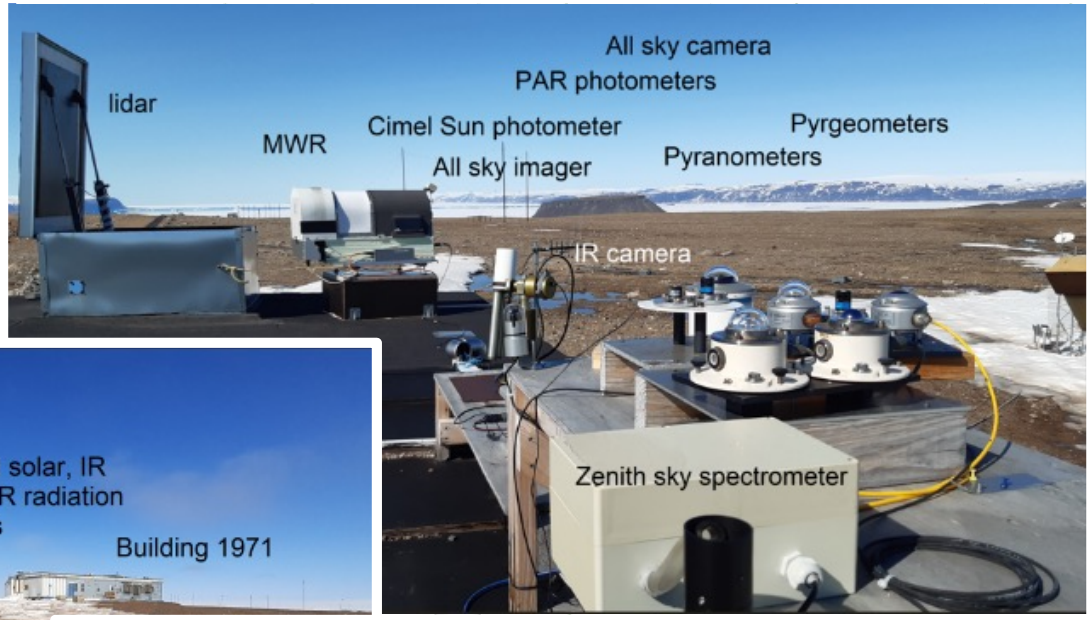
lidar
All sky camera
PAR photometers
MWR
Cimel Sun photometer
All sky imager
Pyrgeometers
Pyranometers
IR camera
Zenith sky spectrometer

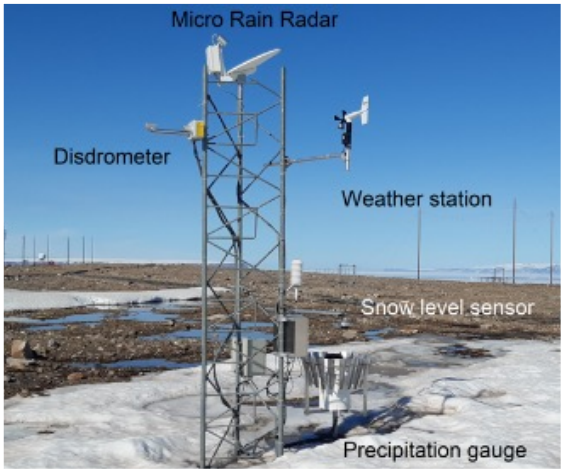
Micro Rain Radar
Disdrometer
Weather station
Snow level sensor
Precipitation gauge

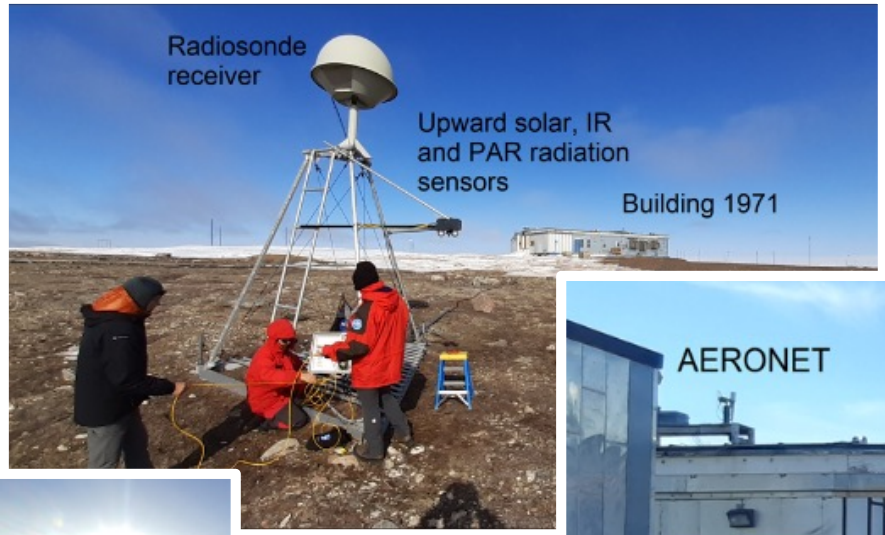
Radiosonde
receiver
Upward solar, IR
and PAR radiation
sensors
Building 1971

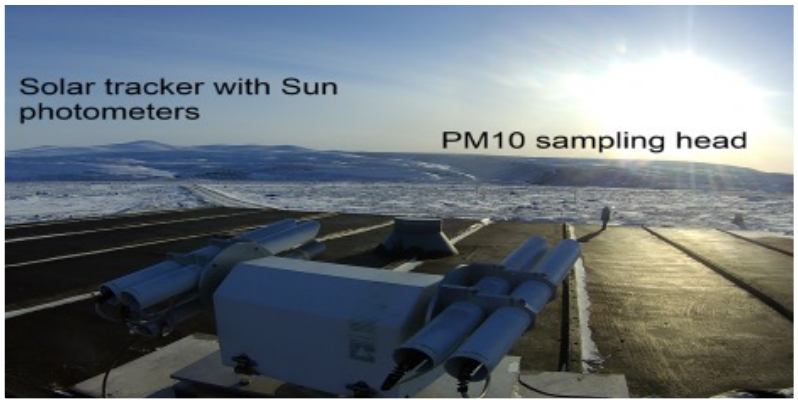
Solar tracker with Sun
photometers
PM10 sampling head

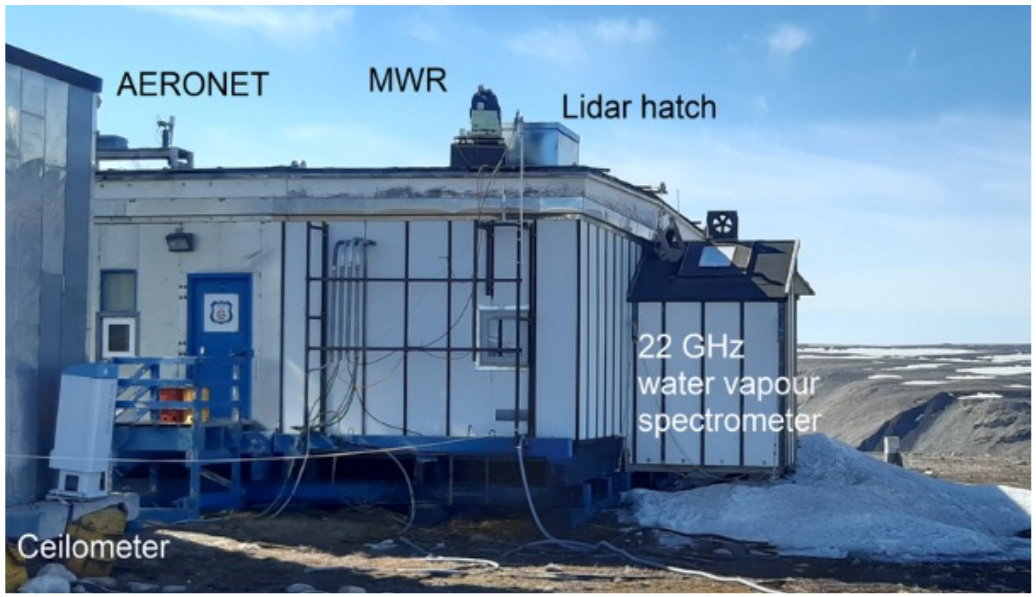
AERONET
MWR
Lidar hatch
22 GHz
water vapour
spectrometer
Ceilometer

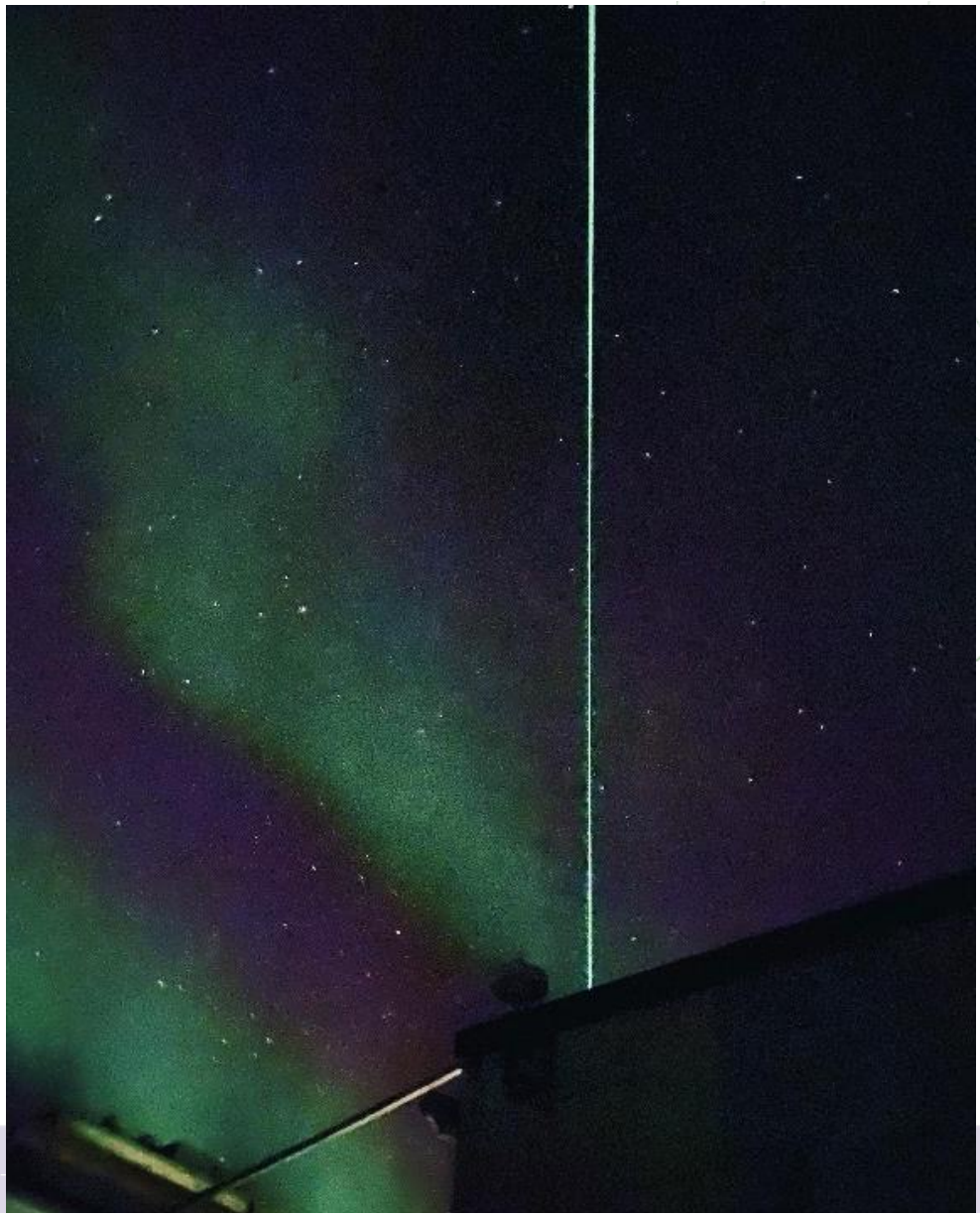

By combining the equation of state for ideal gases and the hydrostatic equation, in aerosol-free regions the lidar signal can be used to derive the atmospheric temperature

THAAO, 76.5°N

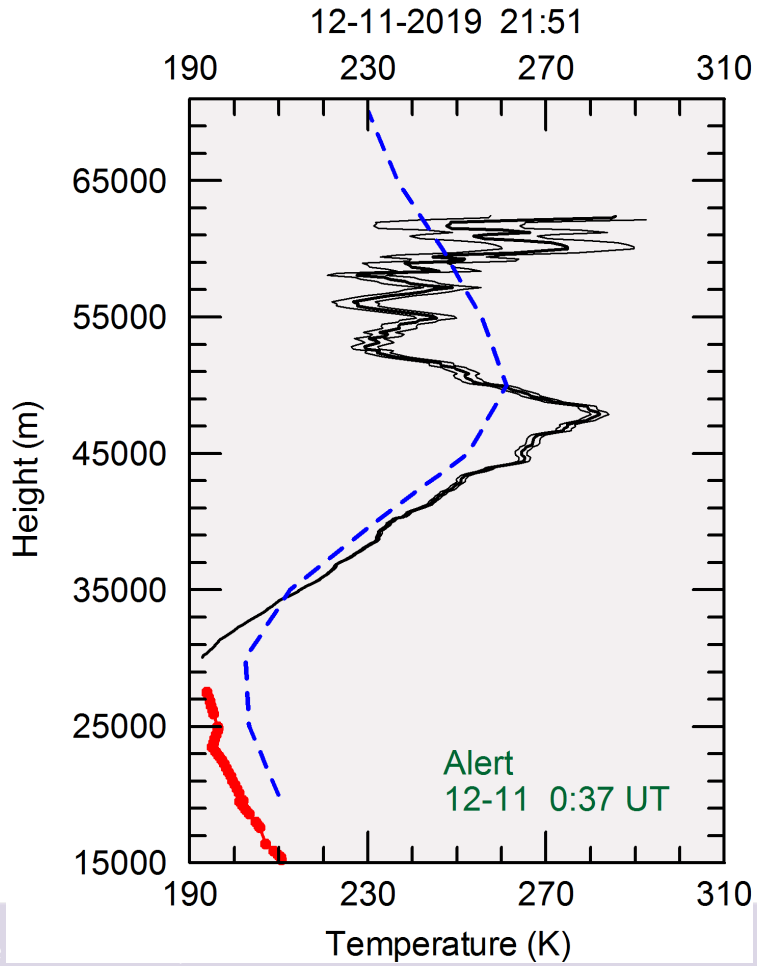

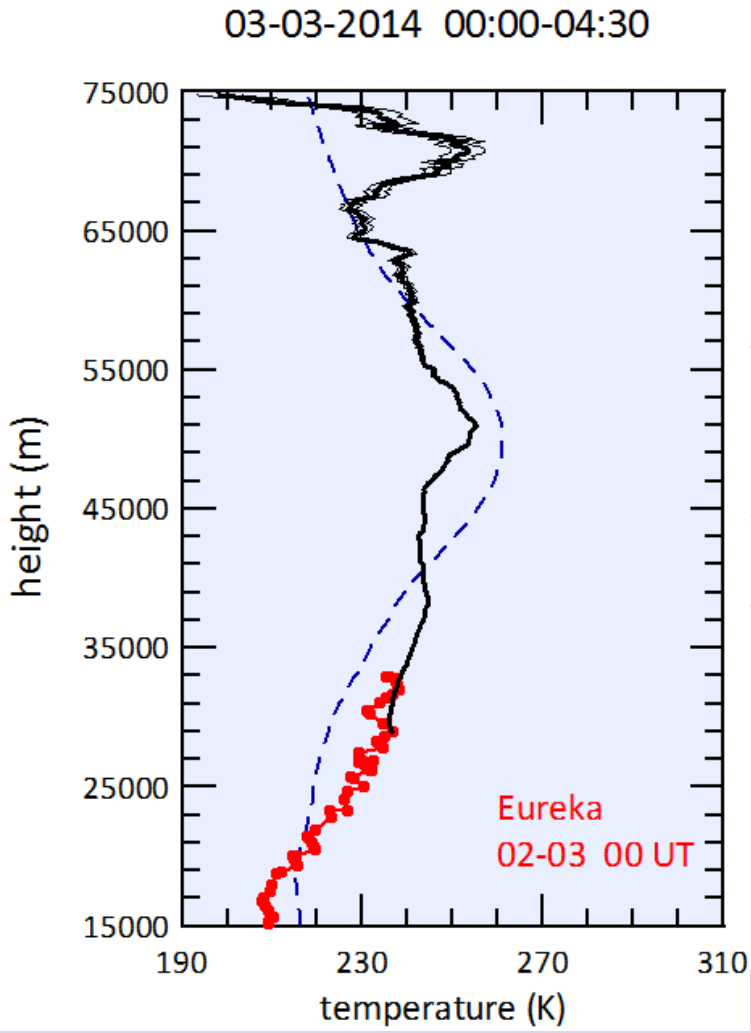

Di Biagio et al., 2010

Temperature profiles in the Arctic: the exceptional 2009 stratospheric warming

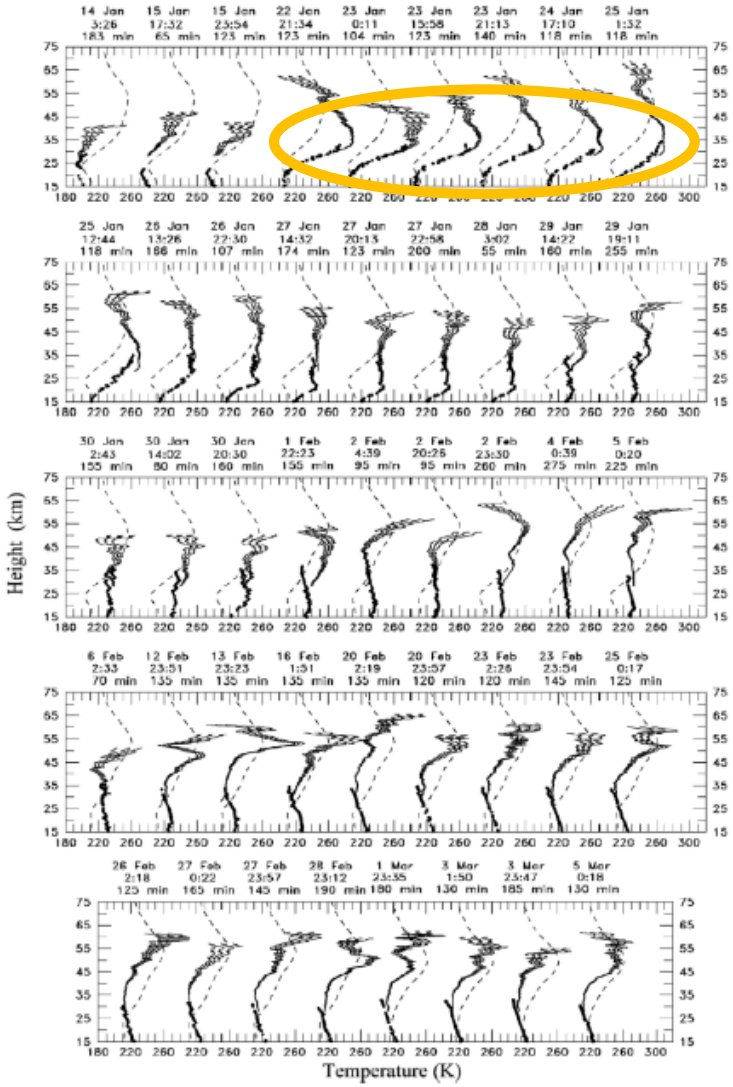

Figure 1. Lidar temperature profiles obtained between 14 January and 5 March 2009 at Thule. T, $T+\sigma$, and $T-\sigma$ are shown. The dashed line represents the CIRA 1986 model [*Barnett and Corney*, 1985] for the month. Dotted profiles are radiosonde data that are the closest in time data (from Eureka or Alert, depending on the data availability). Date, time, and integration time in minutes are reported.

Di Biagio et al., 2010

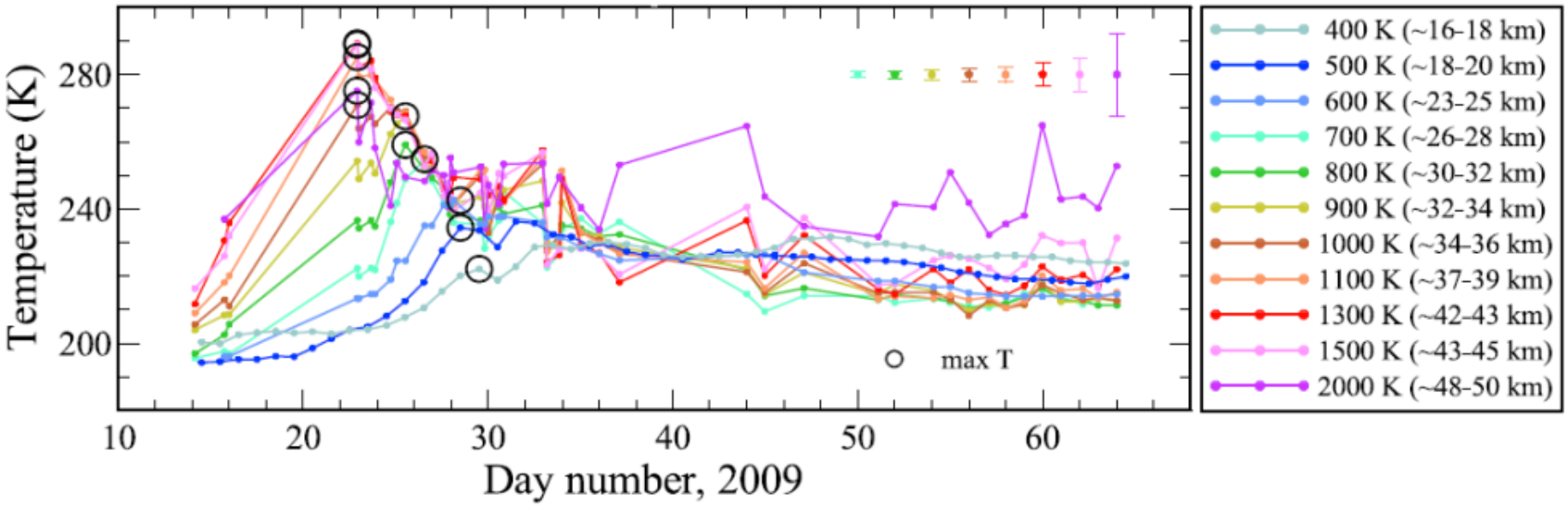

Figure 2. Temporal evolution of stratospheric temperature interpolated at different θ levels between 400 and 2000 K (temperatures at 400, 500, and 600 K are from National Centers for Environmental Predictions (NCEP) reanalyses) in the period 14 January to 5 March 2009 (days 14–64). Maximum 1σ uncertainties at the different levels are indicated by vertical bars. Maximum temperature obtained at each level due to downward propagation of the warming is highlighted by a circle.

Muscari et al., 2007

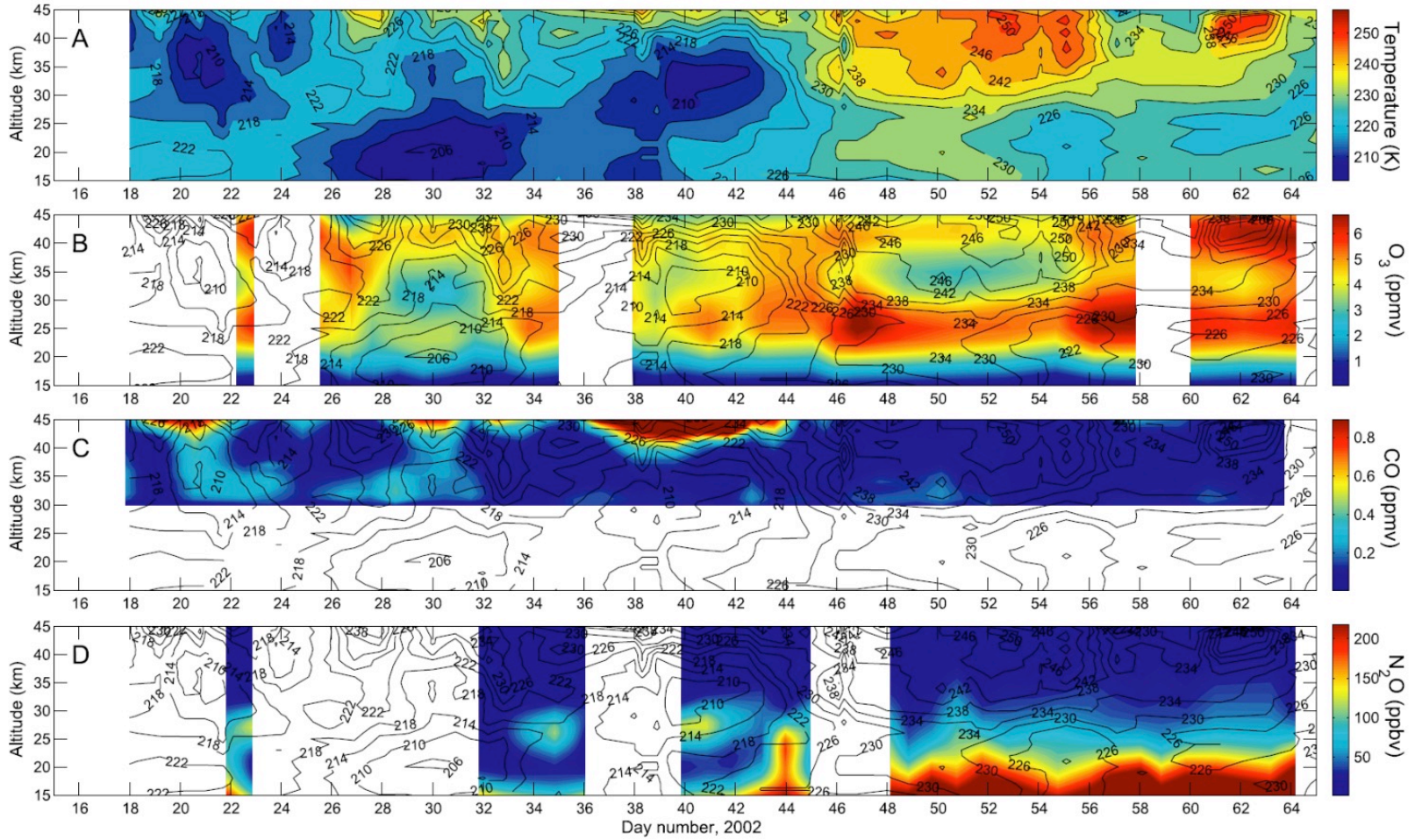

Figure 1. (a) Colored contour maps of lidar/balloon temperature; (b) GBMS O_3; (c) CO; and (d) N_2O, with the relative color scale to the right of each panel. In Figures 1b–1d, lidar/balloon temperature contours of Figure 1a are superimposed on the colored maps with solid black lines. White gaps in GBMS data indicate when no measurement is available for more than 48 hours, because of either poor weather conditions, instrumental malfunctioning, or unreliable spectral data.

- The lidar equation for: single wavelength, vertically pointing elastic backscattering lidar, with aerosols

120

Fernald, 1984

$$\beta_1(Z)+\beta_2(Z)=\frac{X\left(Z\right)\exp\left[-2\left(S_1-S_2\right)\int_{Z_c}^{Z}\beta_2(z)dz\right]}{\frac{X(Z_c)}{\beta_1(Z_c)+\beta_2(Z_c)}-2S_1\int_{Z_c}^{Z}X(z)\exp[-2(S_1-S_2)\int_{Z_c}^{z}\beta_2(z')dz']dz},$$

$X(z) = P(z)\, z^2$ RCS

1 – Rayleigh
2 – Mie
S_1 – extinction-to-backscattering ratio for molecules (Rayleigh)
S_2 - extinction-to-backscattering ratio for particles (Mie)

Di Girolamo et al., 1994

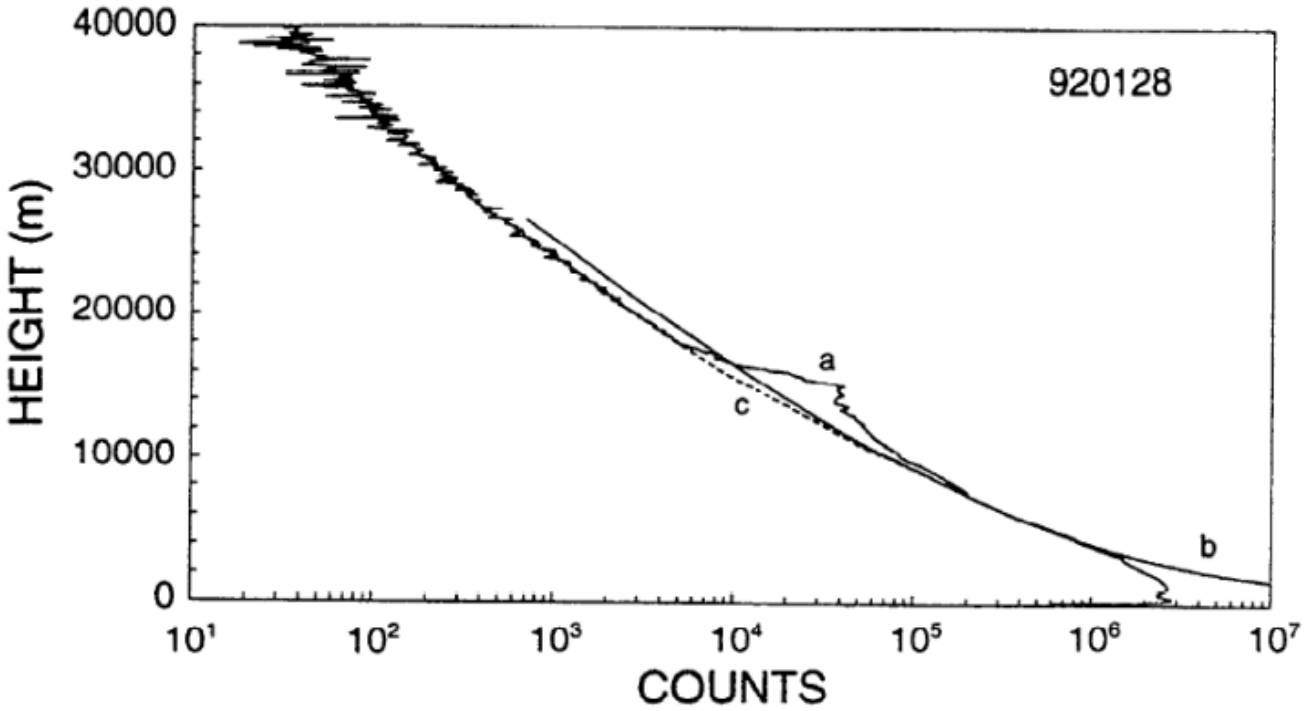

Fig. 1. Lidar echo profile (curve a) and molecular profile (curve b) for January 28, 1992. Curve c is the molecular profile corrected for aerosol extinction. The chopper prevents overlapping in the lowest levels.

125

di Sarra et al., 1998

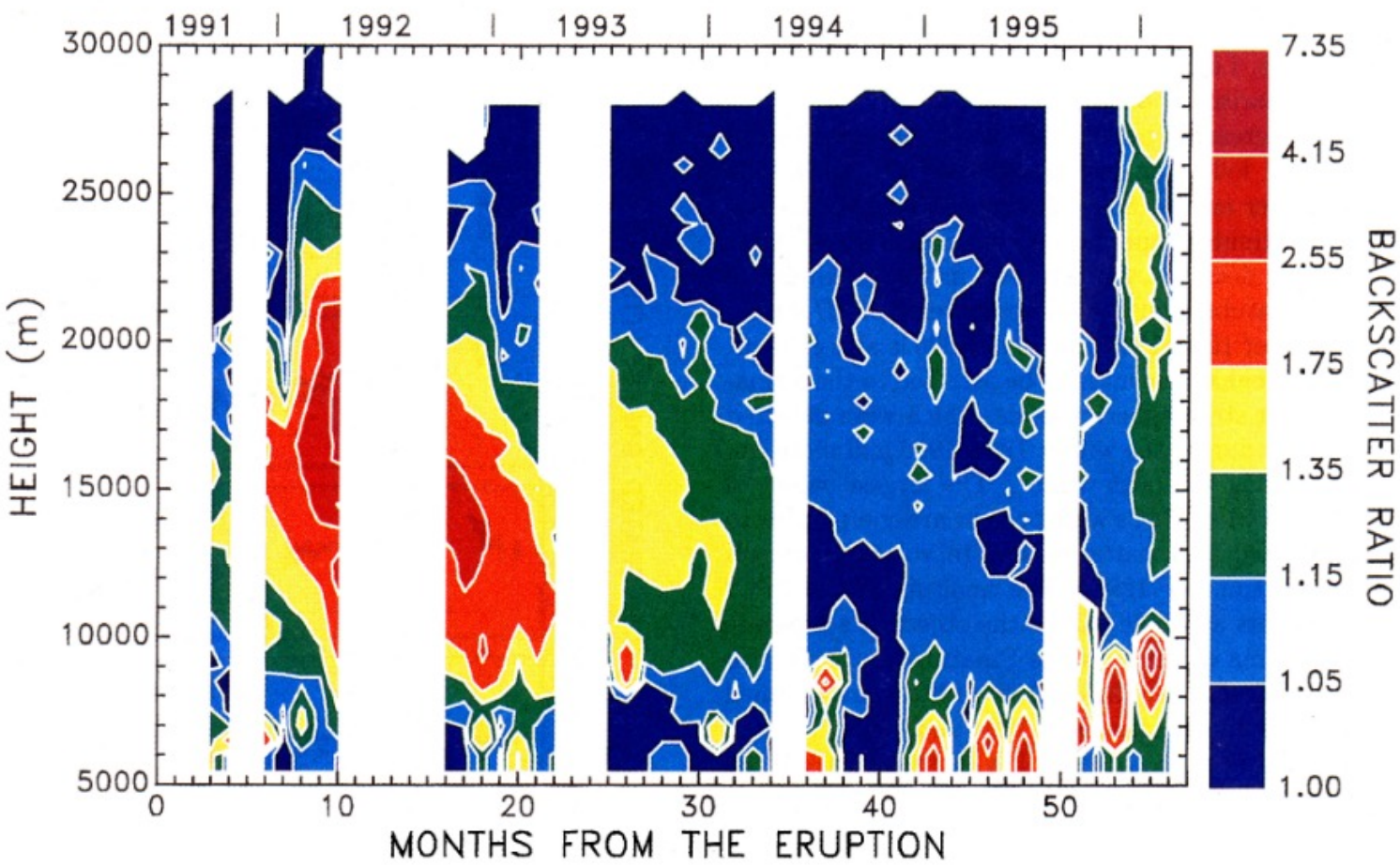

Plate 1. Backscatter ratio as a function of height and time between September 1991 and February 1996. The contour plot is obtained from monthly average profiles.

Stratospheric aerosols from the Pinatubo volcanic eruption above the Thule High Arctic Atmospheric Observatory

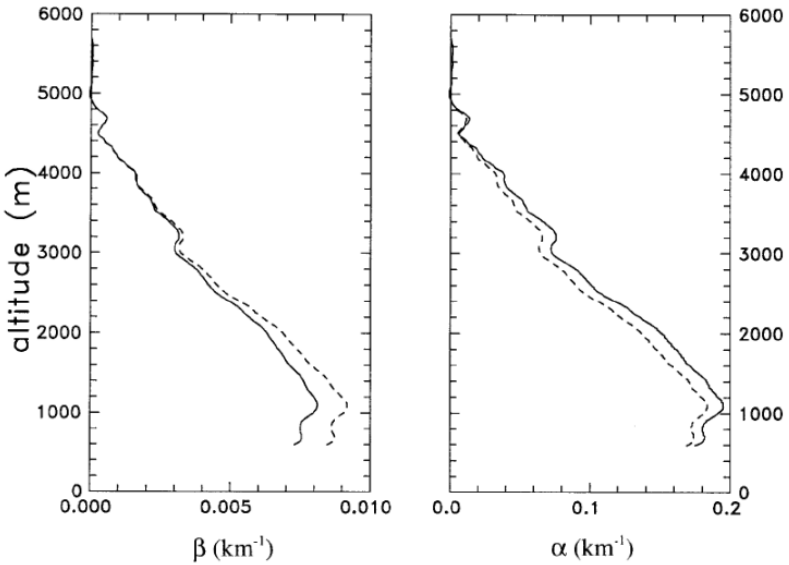

Fig. 9. Profiles of aerosol backscattering (β) and extinction (α) coefficients at 355 nm, derived with the iterative method (solid curves). Also shown is the Fernald–Klett solution (dashed curves). These curves were obtained for the daily averaged lidar profile of 13 June 1996.

Marenco et al.,1997

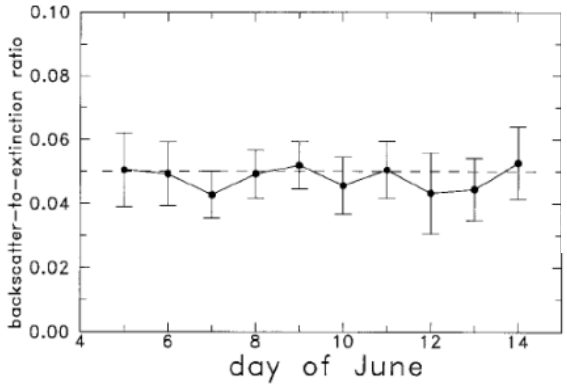

Fig. 10. Mean daily values of the backscatter-to-extinction ratio. The error bars denote the magnitude of the standard deviation. The dashed line indicates the maritime aerosol model used for an *a priori* input to the Fernald–Klett solution ($C = 0.05$).

MODIS Aqua – 11 Apr 2020

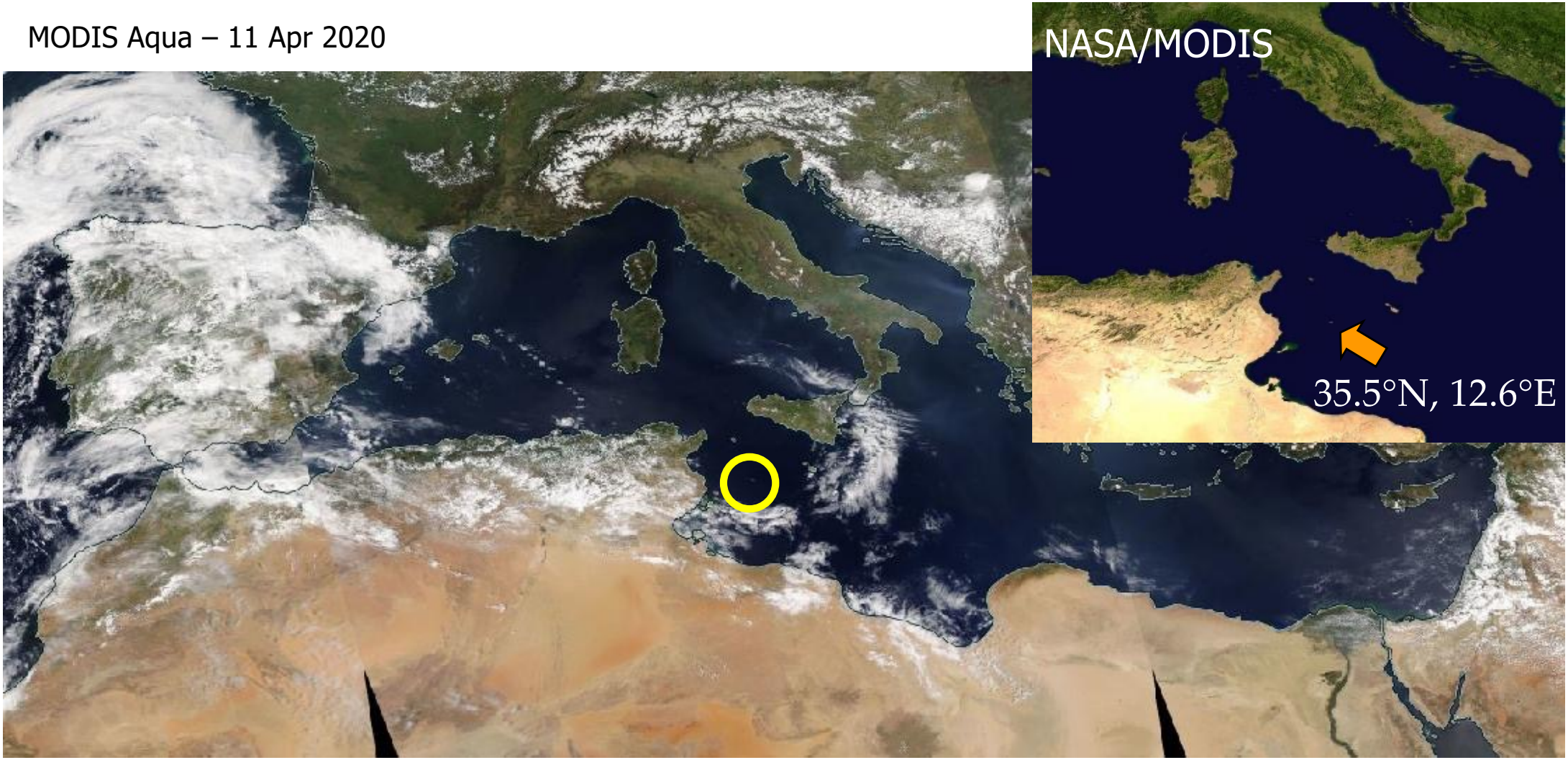

http://www.lampedusa.enea.it

Ground-based and Airborne Measurements of the Aerosol Radiative Forcing (GAMARF) 2008

Lampedusa, 35.5°N 12.6°E

Meloni et al., 2015

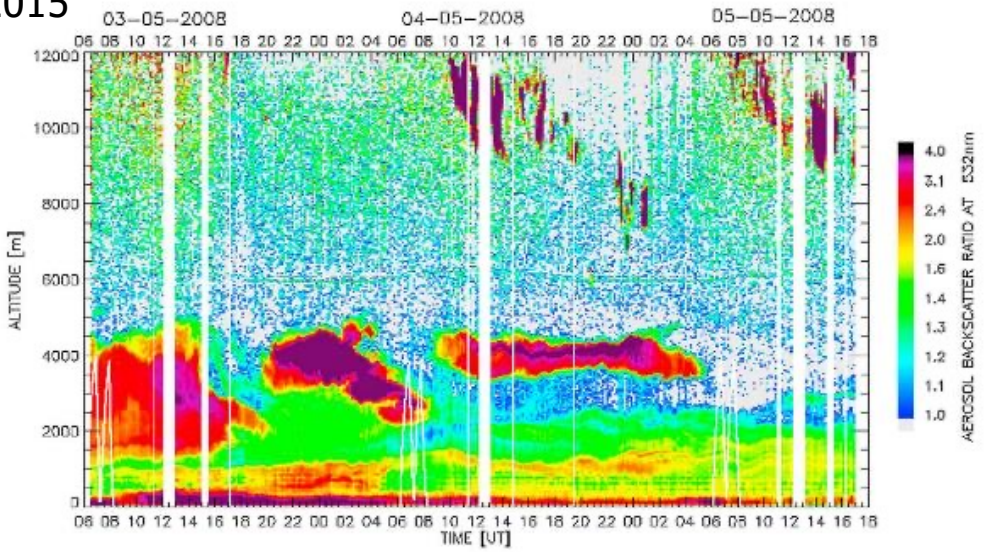

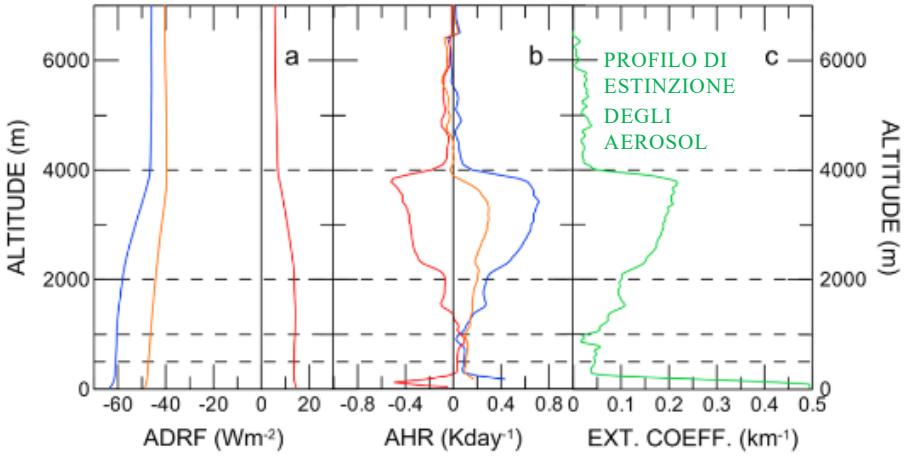

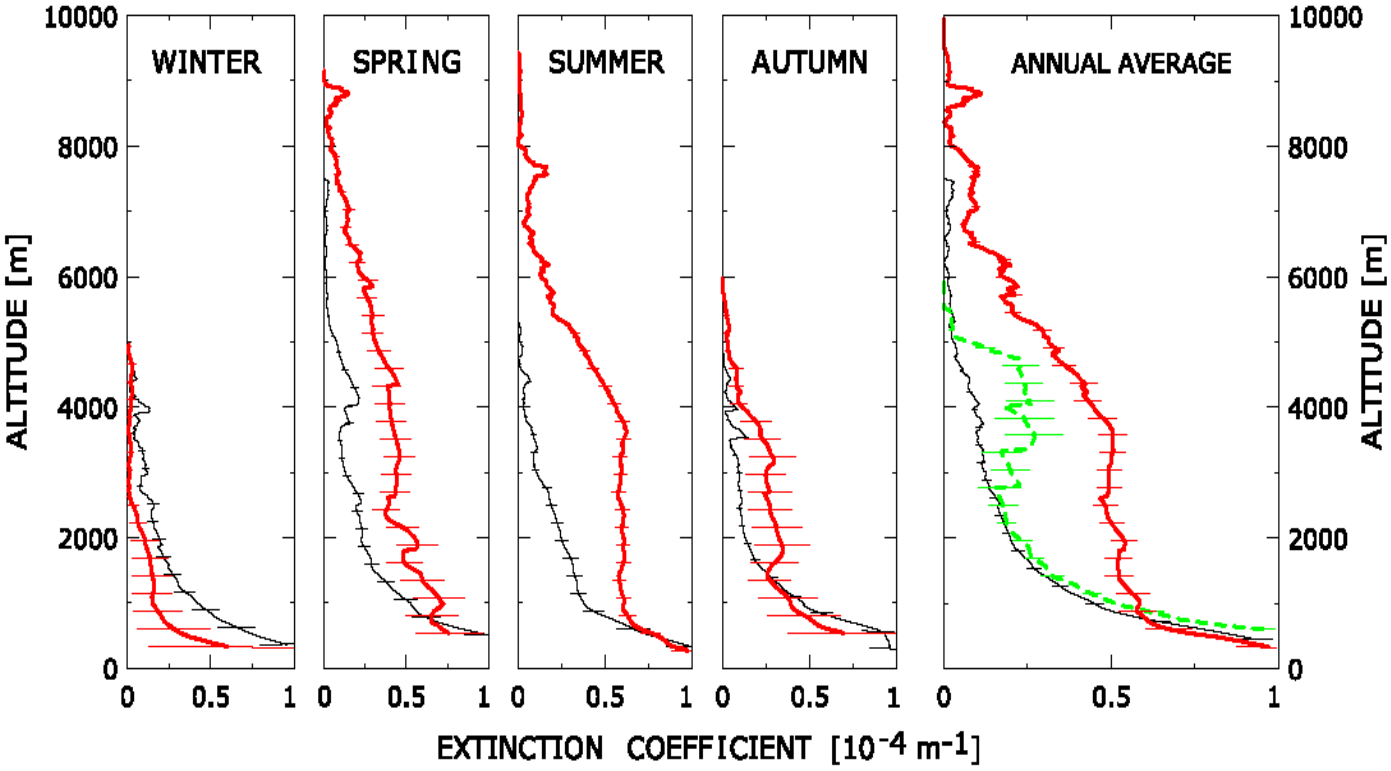

Di Iorio et al., 2009

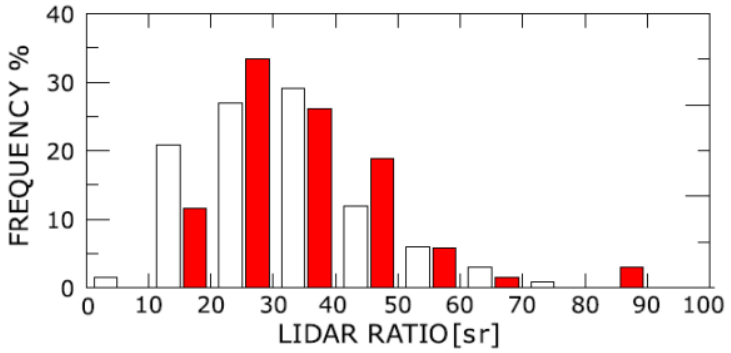

Figure 5. Lidar ratio frequency of occurrences for Class 0 (white bars) and Class 1b (red bars; see text).

long term measurements

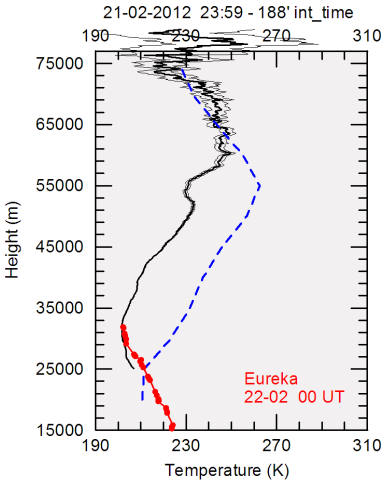

Temperature profiles obtained by lidar at Thule. T, T+σ, and T-σ are shown in black lines. The blue dashed line represents the temperature CIRA 1986 model for the specific month. Red dotted profile is closest in time radiosonde data available from Eureka or Alert.

Backscatter ratio versus height obtained at Thule in the period September 1991 to February 1996. The lidar has permitted to show the build up and the decay of the volcanic aerosols originated from the eruption of Mount Pinatubo in June 1991 [*di Sarra et al., 1998*]

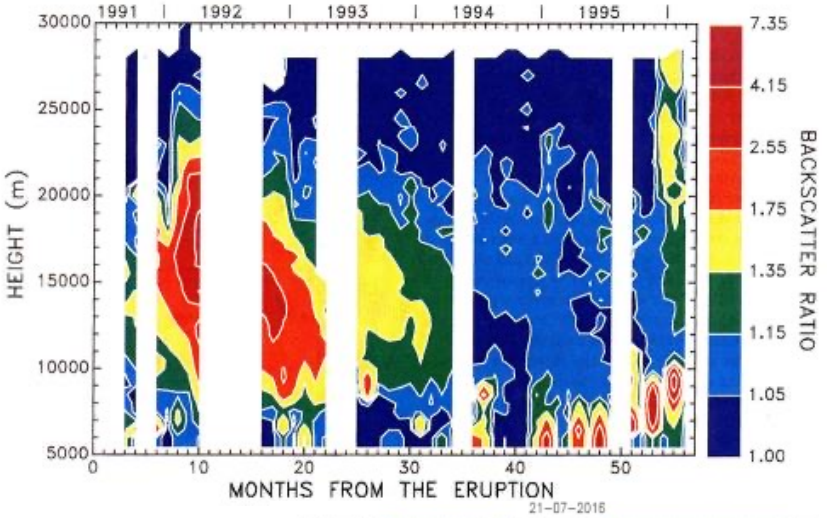

A long record of Arctic stratospheric temperatures derived by Thule LIDAR during winter campaigns

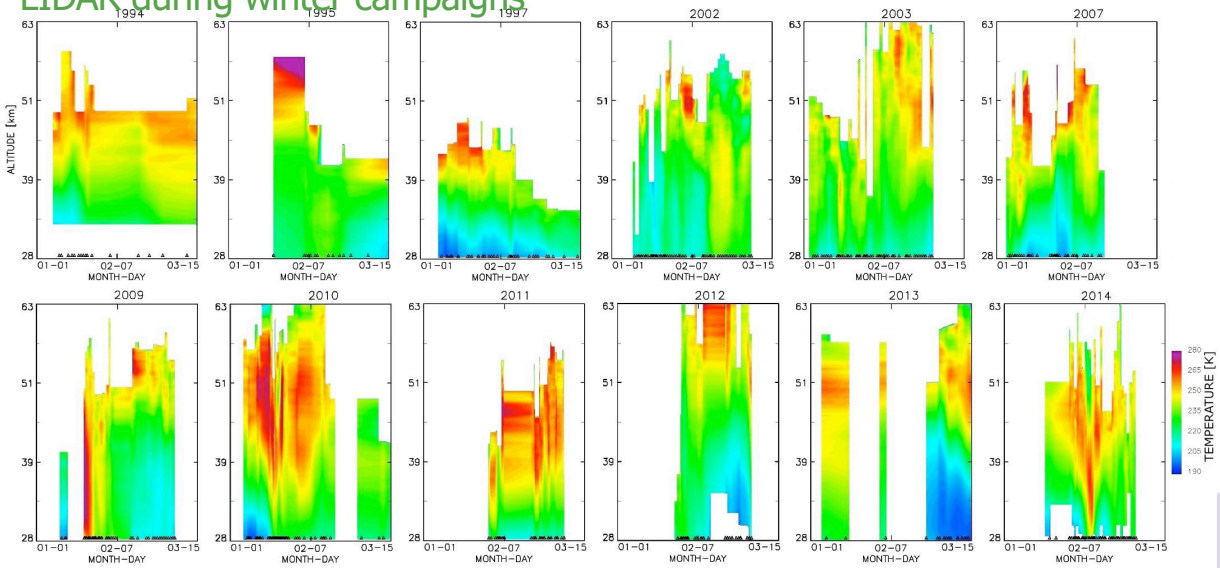

LIDAR Contour plots of the aerosol backscattering coefficient at 1064 nm. Examples of the time evolution of low level clouds during the SVAAP campaign in July 2016.

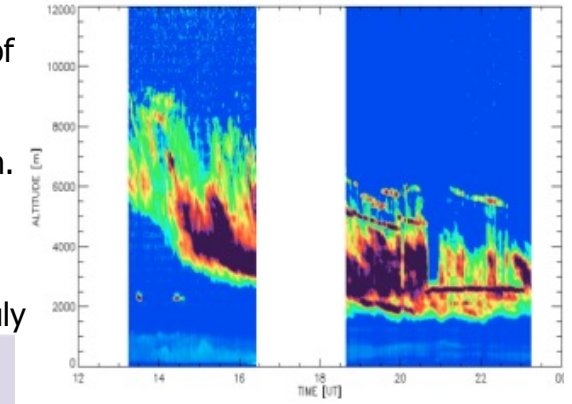

Integrated retrievals (e.g. GRASP)

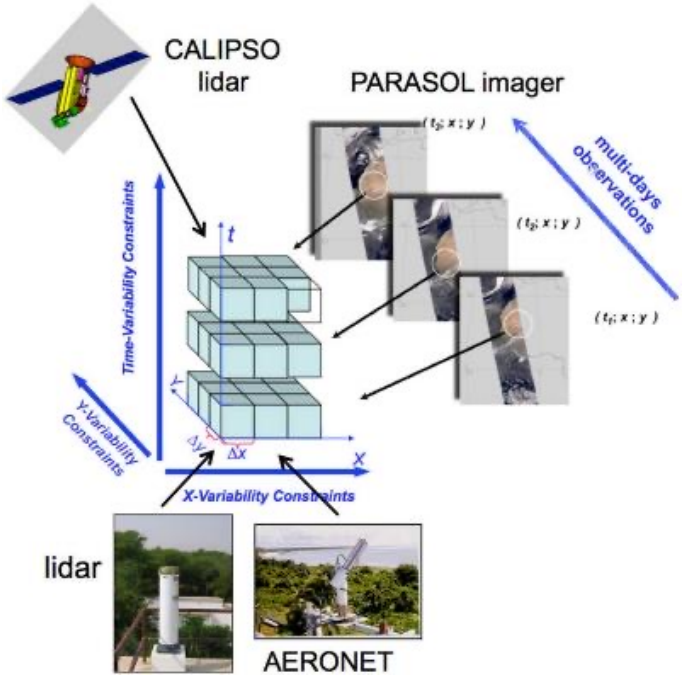

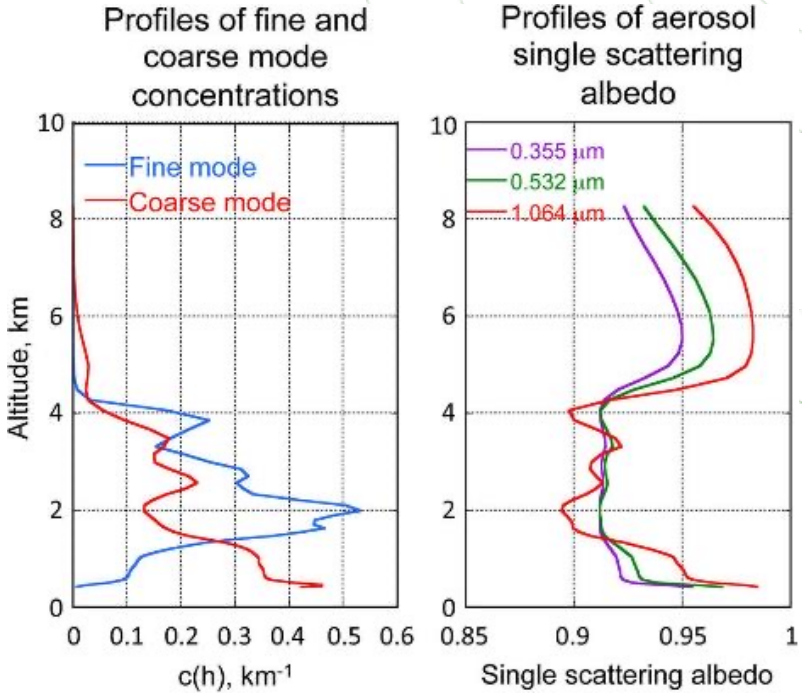

Polarization!

130

Particle linear depolarization ratio

$$\delta = \frac{\mathrm{Mie}_{\mathrm{cross}}}{\mathrm{Mie}_{\mathrm{co}}}$$

Already available from L1 data!

Essential quantity in aerosol typing and separation of aerosol components

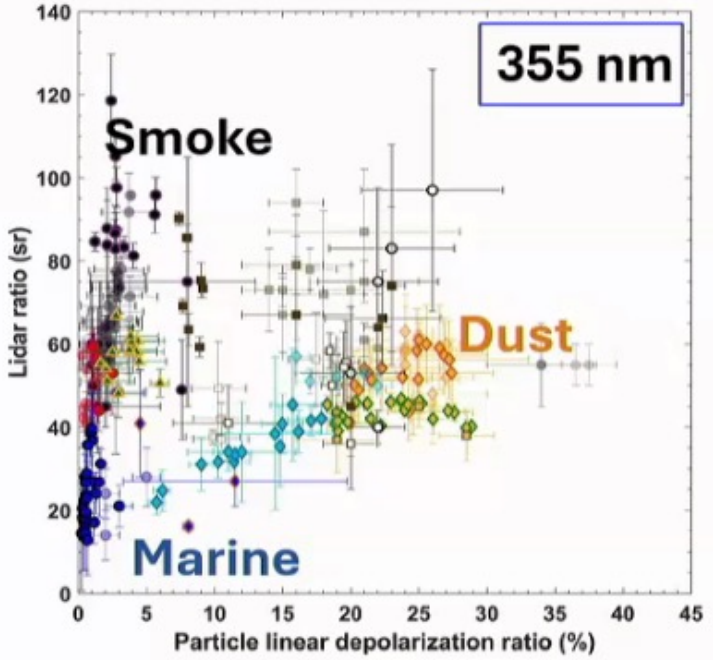

Floutsi et al., AMT 2023 [2]

di Sarra et al., 2001

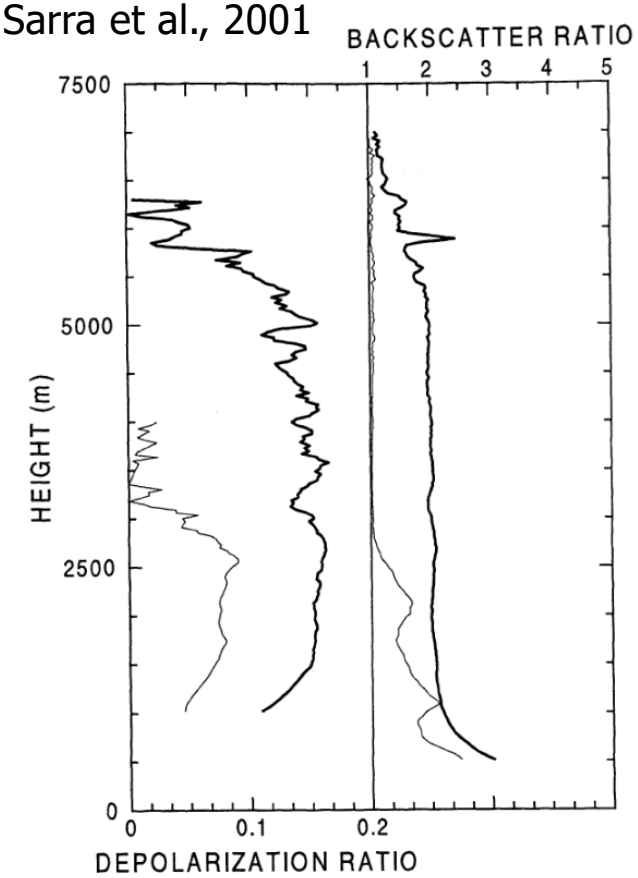

Figure 3. (left) Backscatter ratio and (right) depolarization ratio profiles for May 28 (thin lines) and June 3 (thick lines), 1999.

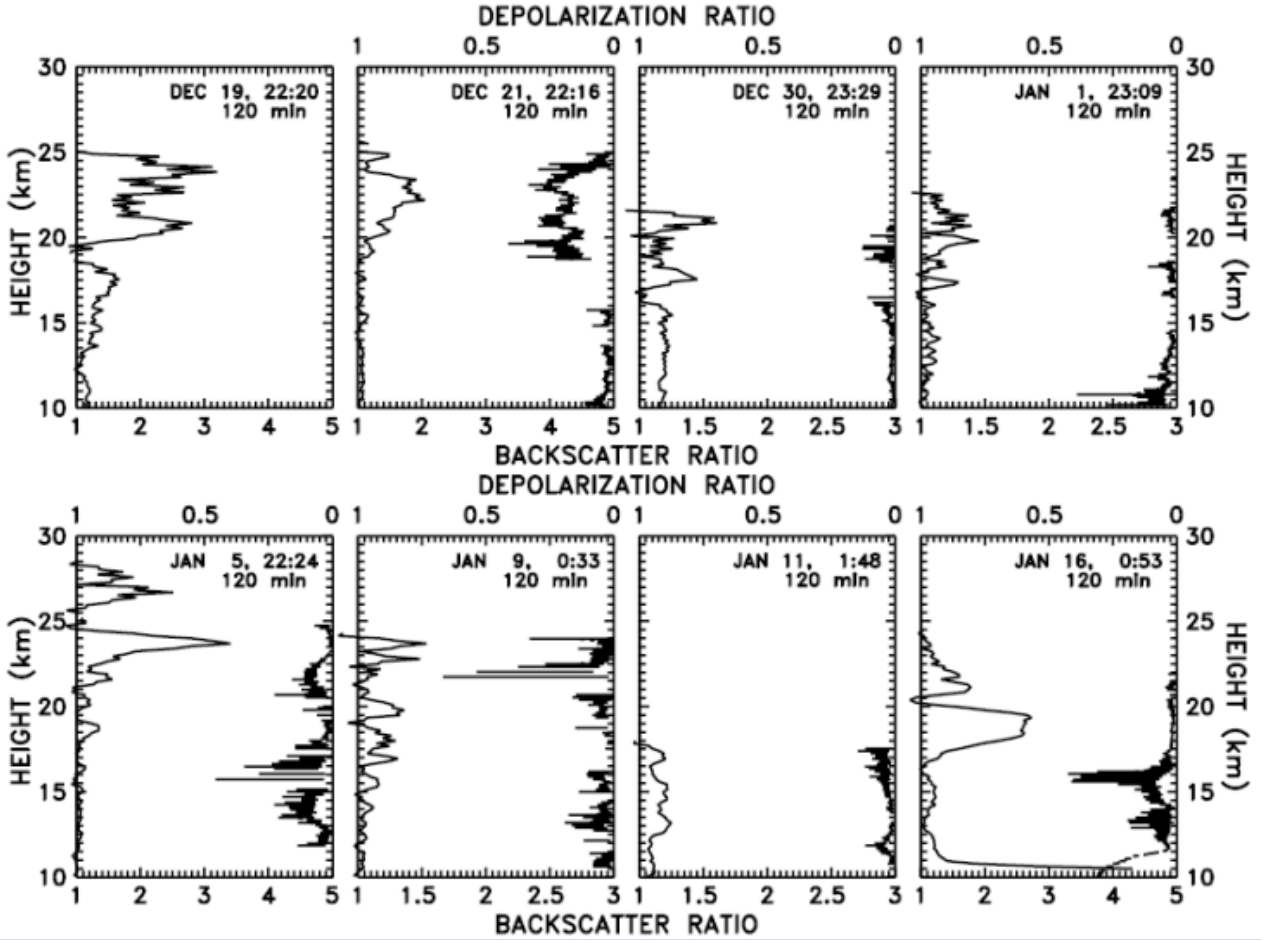

di Sarra et al., 2002

Incoherent elastic backscattering lidar

No information from the phase of the signal

Emission and detection at the same wavelength

Incoherent «broadband» elastic backscattering lidar

Outside of gas absorption lines: aerosol/clouds

single/multi wavelengths

depolarization

without aerosol: density, temperature

In/out of absorption lines (differential absorption): gas concentrations

$$P_{on}(r) = P_0^{on} \frac{A}{r^2} \eta_{on} \frac{c\Delta t}{2} \beta_{on}(r) T_r^{on}(r)^2$$

$$P_{off}(r) = P_0^{off} \frac{A}{r^2} \eta_{off} \frac{c\Delta t}{2} \beta_{off}(r) T_r^{off}(r)^2$$

$$T_r^{on}(r) = \exp\left\{-\int_0^r \left[n_g(x)\sigma_{on} + \alpha_M^{on}(x) + \alpha_R^{on}(x)\right]dx\right\}$$

$$T_r^{off}(r) = \exp\left\{-\int_0^r \left[n_g(x)\sigma_{off} + \alpha_M^{off}(x) + \alpha_R^{off}(x)\right]dx\right\}$$

$$\overline{n}_g(r+\Delta r/2) = \frac{1}{2\Delta r(\sigma_{on} - \sigma_{off})}\left[\ln\frac{P_{on}(r)P_{off}(r+\Delta r)}{P_{on}(r+\Delta r)P_{off}(r)} - E - B\right]$$

$$E = 2\Delta r(\overline{\alpha}_M^{on} + \overline{\alpha}_R^{on} - \overline{\alpha}_M^{off} - \overline{\alpha}_R^{off})$$

$$B = \ln\left[\frac{\beta_{on}(r)\beta_{off}(r+\Delta r)}{\beta_{off}(r)\beta_{on}(r+\Delta r)}\right]$$

150

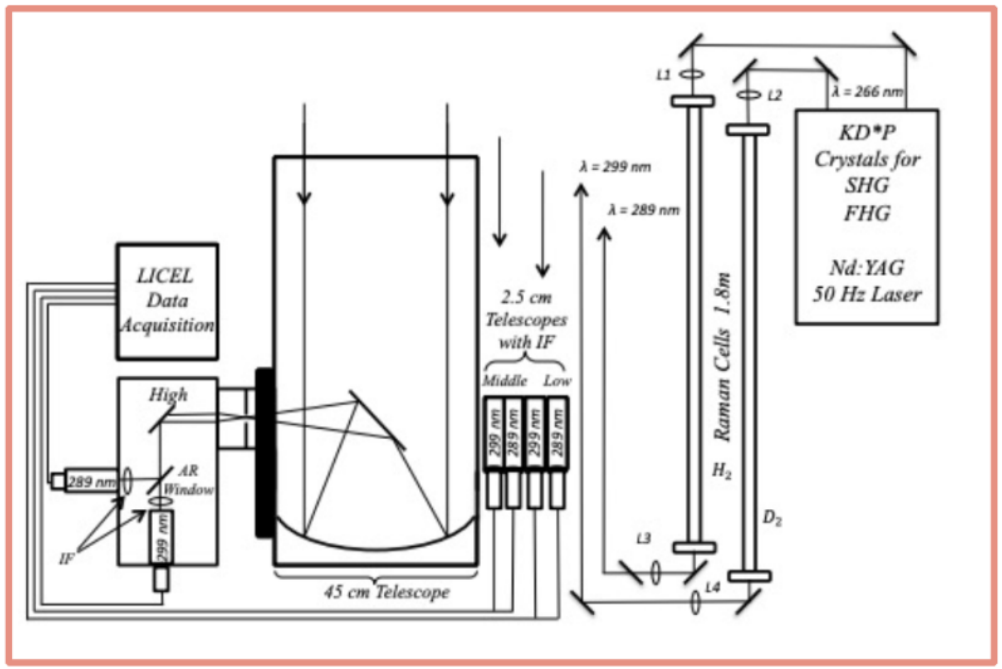

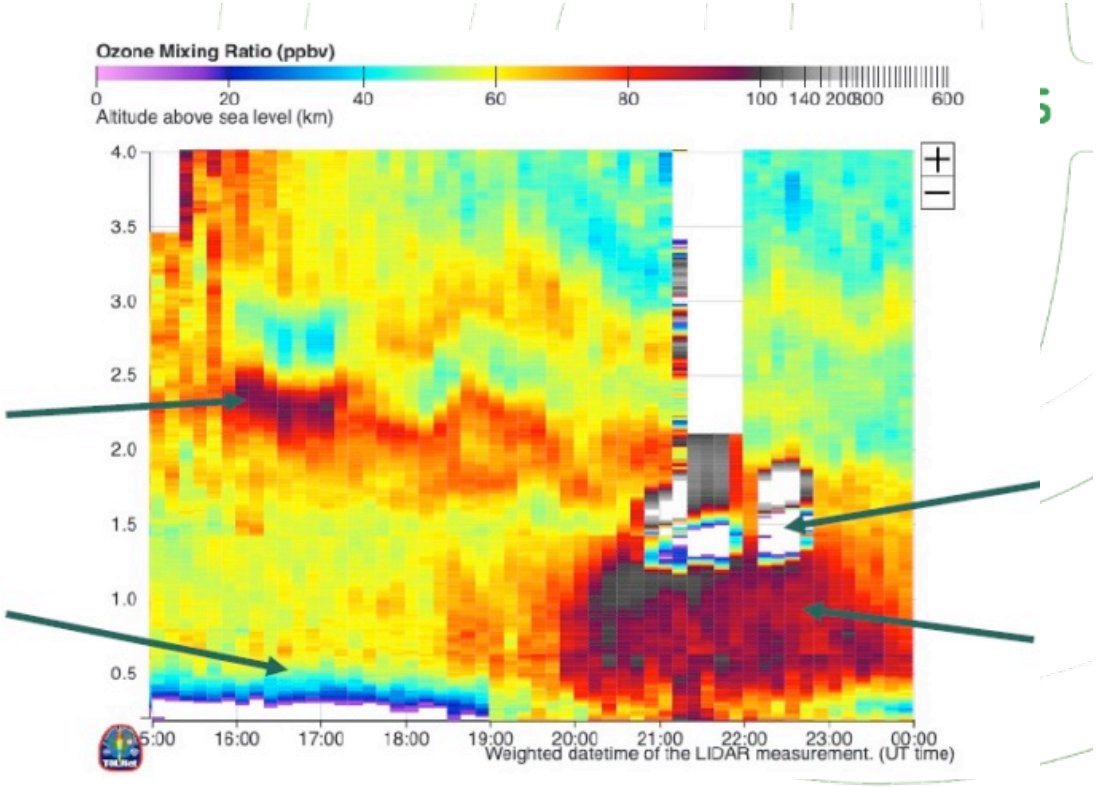

Sullivan, 2024

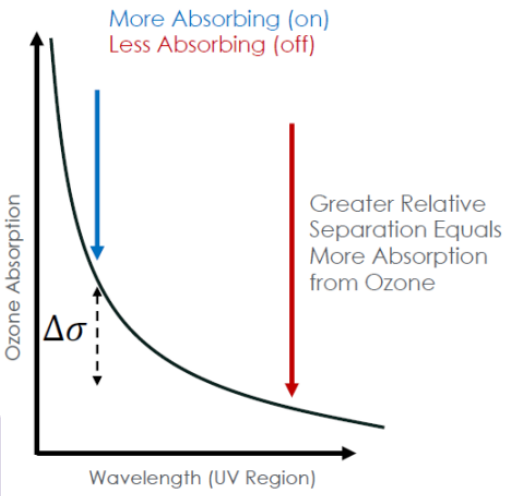

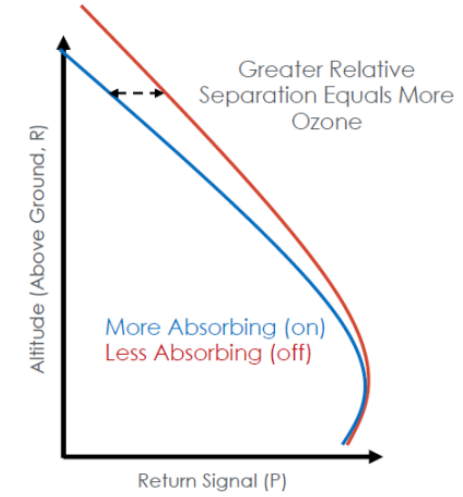

https://appliedsciences.nasa.gov/sites/default/files/2024-08/GroundNetworks_Part4_final.pdf

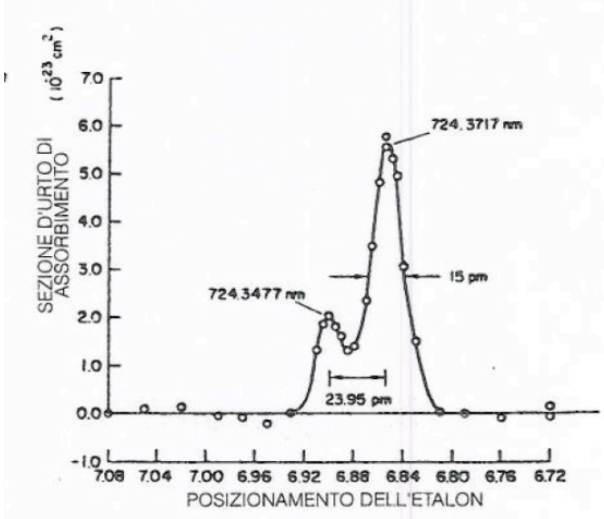

Cahen et al., 1982

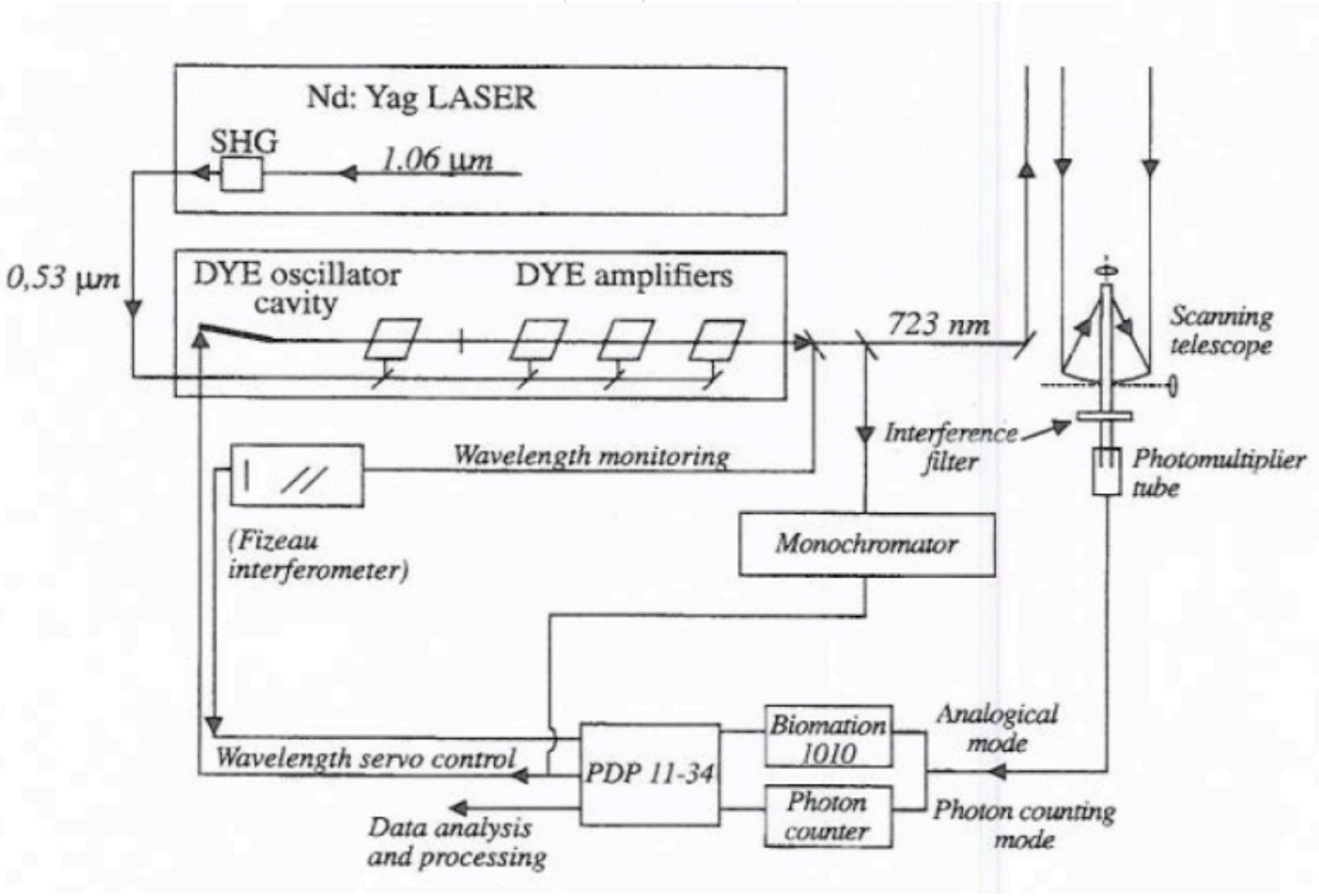

- Incoherent «narrowband» elastic backscattering lidar
  - HSRL: aerosol
  - Doppler shift: wind velocity (*)
  - line shape: temperature

(*) not exactly the same wavelength, but elastic scattering processes

Frequency Spectrum of Laser Echoes from Atmospheric Constituents and Determination of the Aerosol Content of Air[1]

G. FIOCCO AND J. B. DEWOLF

Massachusetts Institute of Technology, Cambridge

(Manuscript received 21 August 1967)

ABSTRACT

Spectral analysis of the echoes obtained from atmospheric constituents in optical radar experiments yields information related to wind motion, temperature and composition. In particular, air with suspended aerosols is considered, and preliminary experiments are described showing that apparatus of limited resolution yields the ratio of the aerosol-to-molecular component. In the experiments, radiation from a cw He-Ne laser was scattered by air with a variable aerosol content. Spectral analysis of the scattered light was performed with a pressure-scanned Fabry-Perot interferometer.

1. Introduction

With coherent, quasi-monochromatic light sources it is possible to perform a spectral analysis of the light very small scale, such techniques yield in a simple manner the ratio of the aerosol-to-gaseous component. In light-scattering experiments in which only the intensity

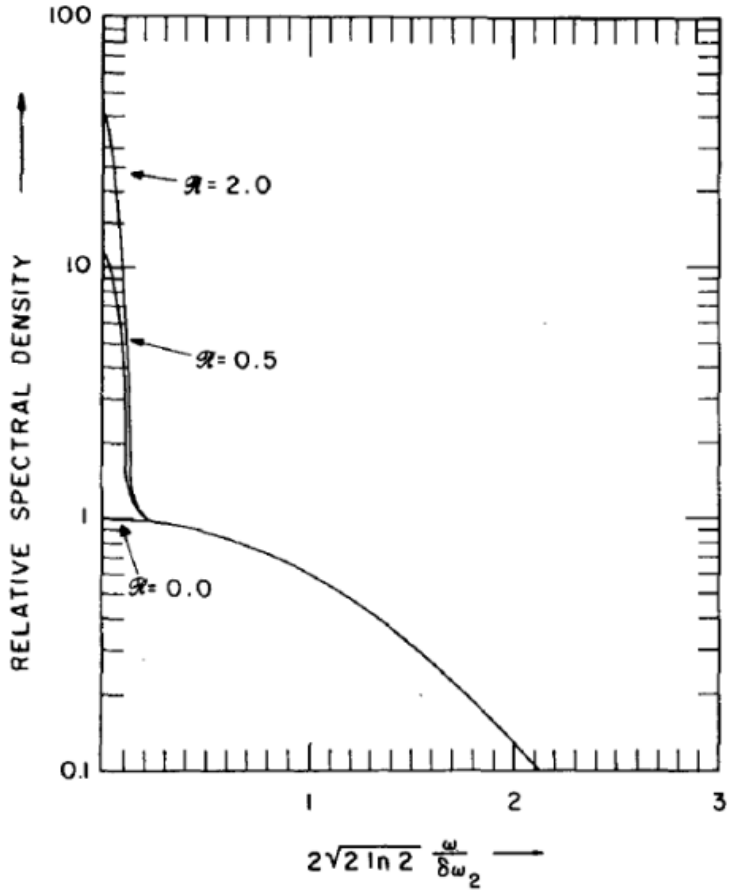

FIG. 2. Relative spectral density of light scattered from air with variable aerosol content as would be observed with a high-resolution spectrometer.

LETTERS TO NATURE

Measurement of Temperature and Aerosol to Molecule Ratio in the Troposphere by Optical Radar

WE wish to describe preliminary optical radar measurements of atmospheric temperature and aerosol to molecule ratio. Optical radar can radiate pulses of highly monochromatic laser light and resolve the frequency spectrum of the light

between molecules. This
wavelength to collision m
case in the upper atmosp
fluctuations modify the spe
components (the Brillouin
the peaks are not expecte
should be a broadening of t
in its shape. Yip and Nelk

Fiocco et al., 1971

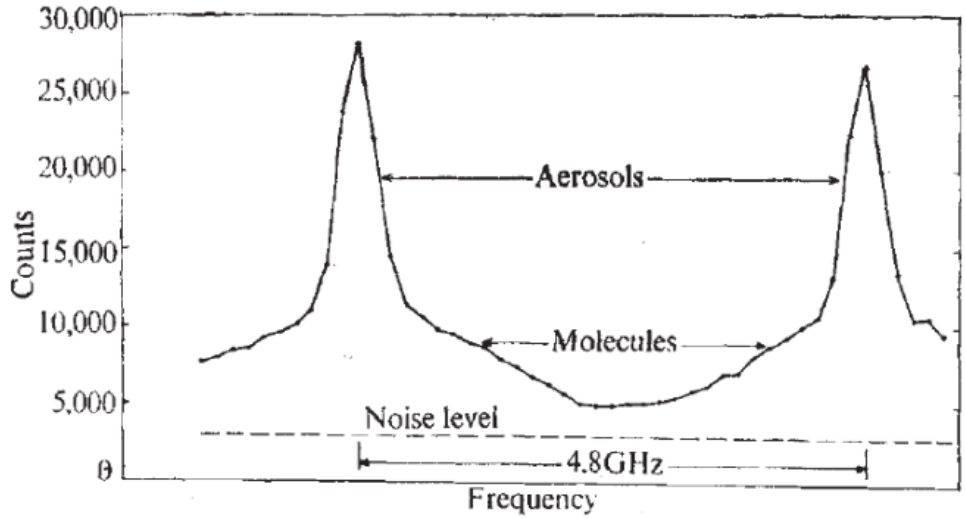

Fig. 1 Spectrum of echoes from air. Contributions of molecules from aerosols can be separated.

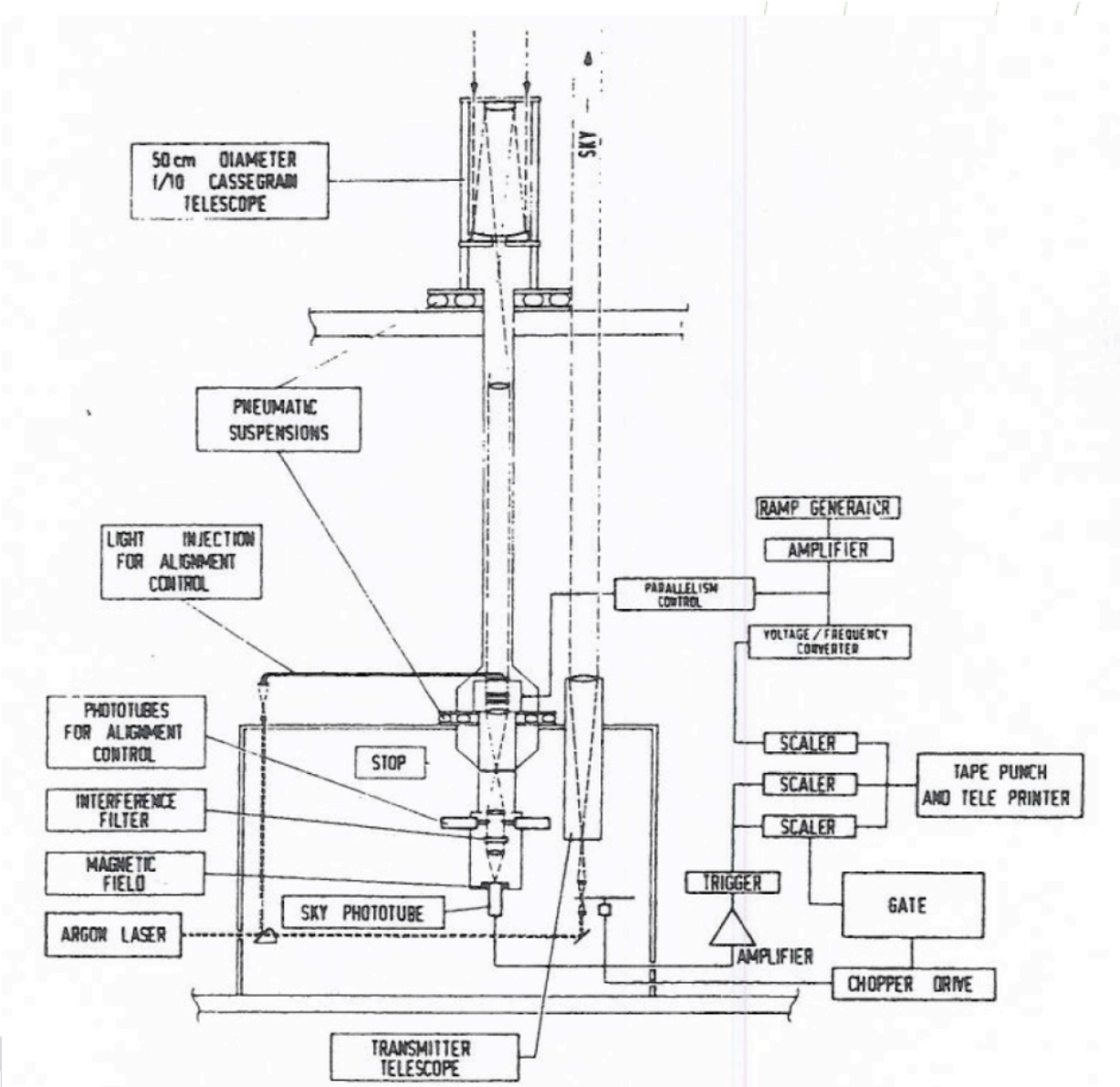
50 cm DIAMETER
1/10 CASSEGRAIN
TELESCOPE
SKY
PNEUMATIC
SUSPENSIONS
LIGHT INJECTION
FOR ALIGNMENT
CONTROL
RAMP GENERATOR
AMPLIFIER
PARALLELISM
CONTROL
VOLTAGE / FREQUENCY
CONVERTER
PHOTOTUBES
FOR ALIGNMENT
CONTROL
STOP
SCALER
SCALER
SCALER
TAPE PUNCH
AND TELE PRINTER
INTERFERENCE
FILTER
MAGNETIC
FIELD
SKY PHOTOTUBE
TRIGGER
GATE
ARGON LASER
AMPLIFIER
CHOPPER DRIVE
TRANSMITTER
TELESCOPE

$$\delta\nu_R = \frac{1}{\lambda}\sqrt{\frac{32k\ln(2)T}{M}} = 79{,}5\frac{\sqrt{T}}{\lambda}\,\mathrm{GHz}$$

At 532 nm and 280 K, $\delta\nu_R$ is 2.5 GHz

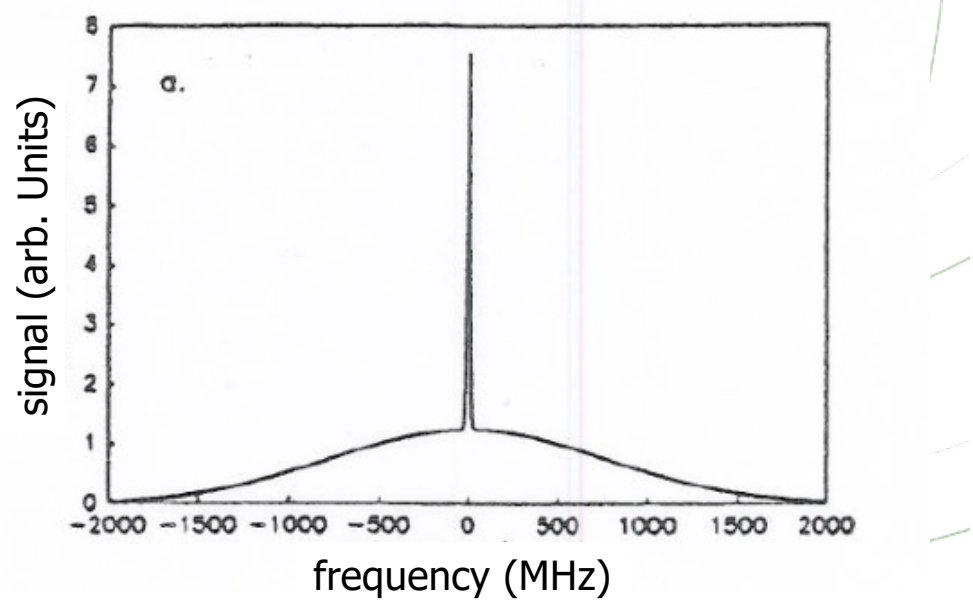

HSR lidar

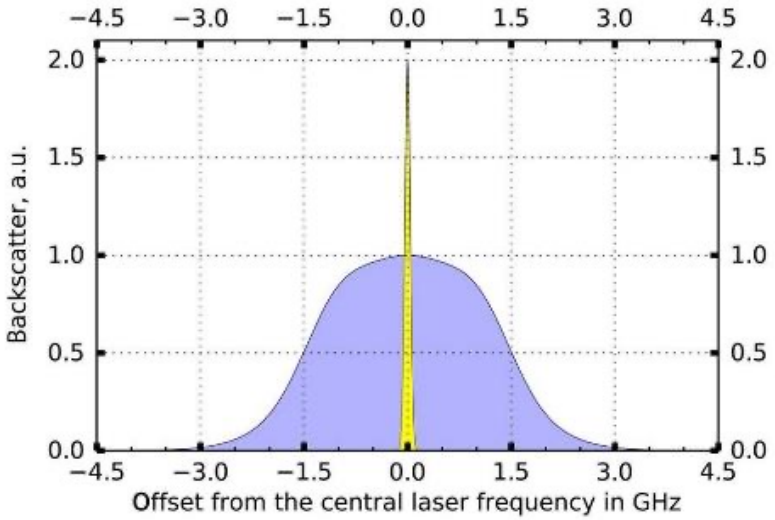
−4.5 −3.0 −1.5 0.0 1.5 3.0 4.5
2.0
1.5
1.0
0.5
0.0
Backscatter, a.u.
Offset from the central laser frequency in GHz

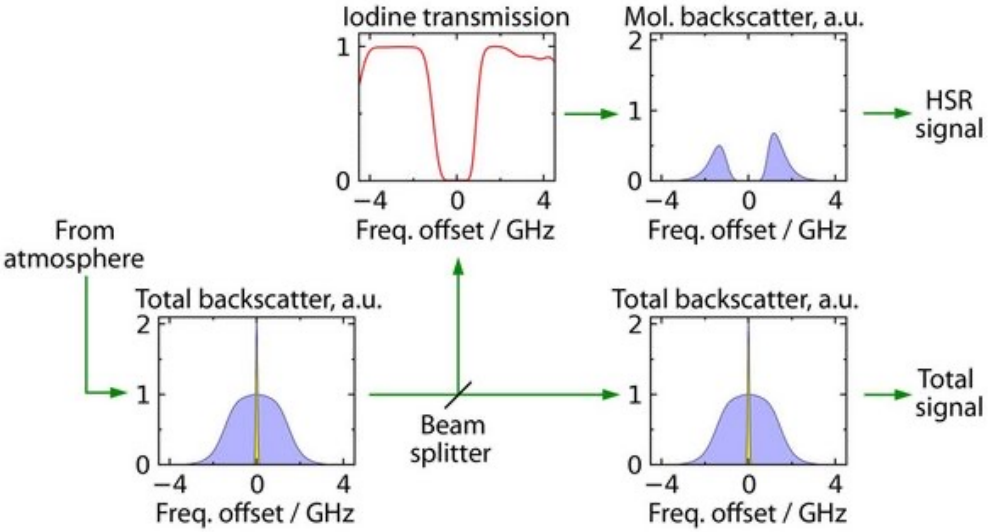
Iodine transmission
Mol. backscatter, a.u.
HSR signal
From atmosphere
Total backscatter, a.u.
Total backscatter, a.u.
Beam splitter
Total signal
Freq. offset / GHz

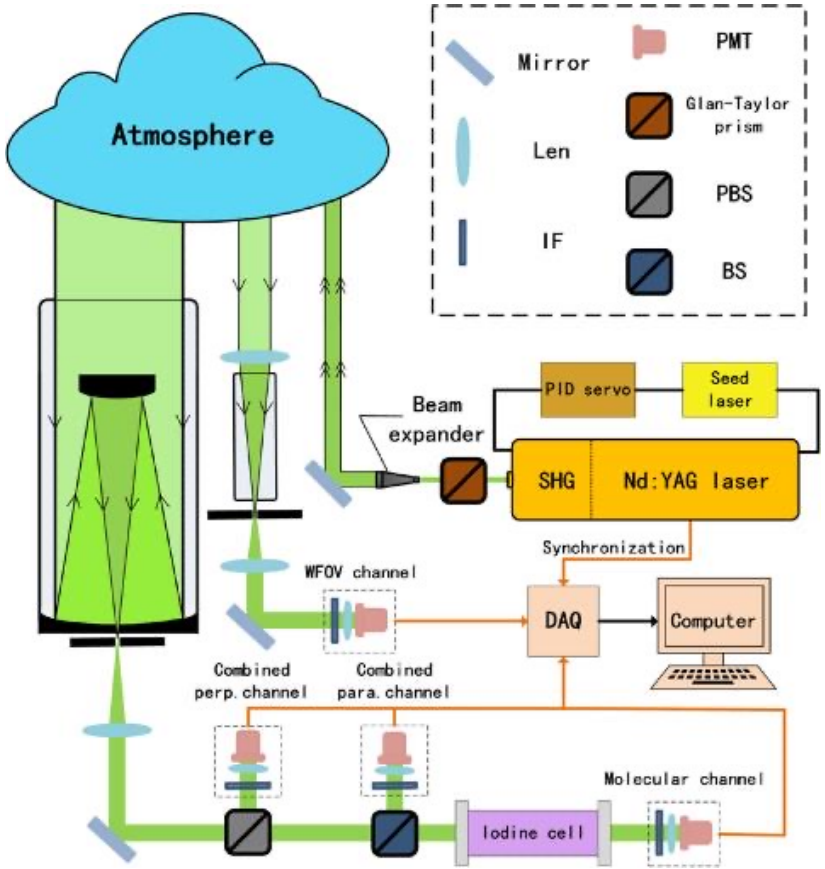

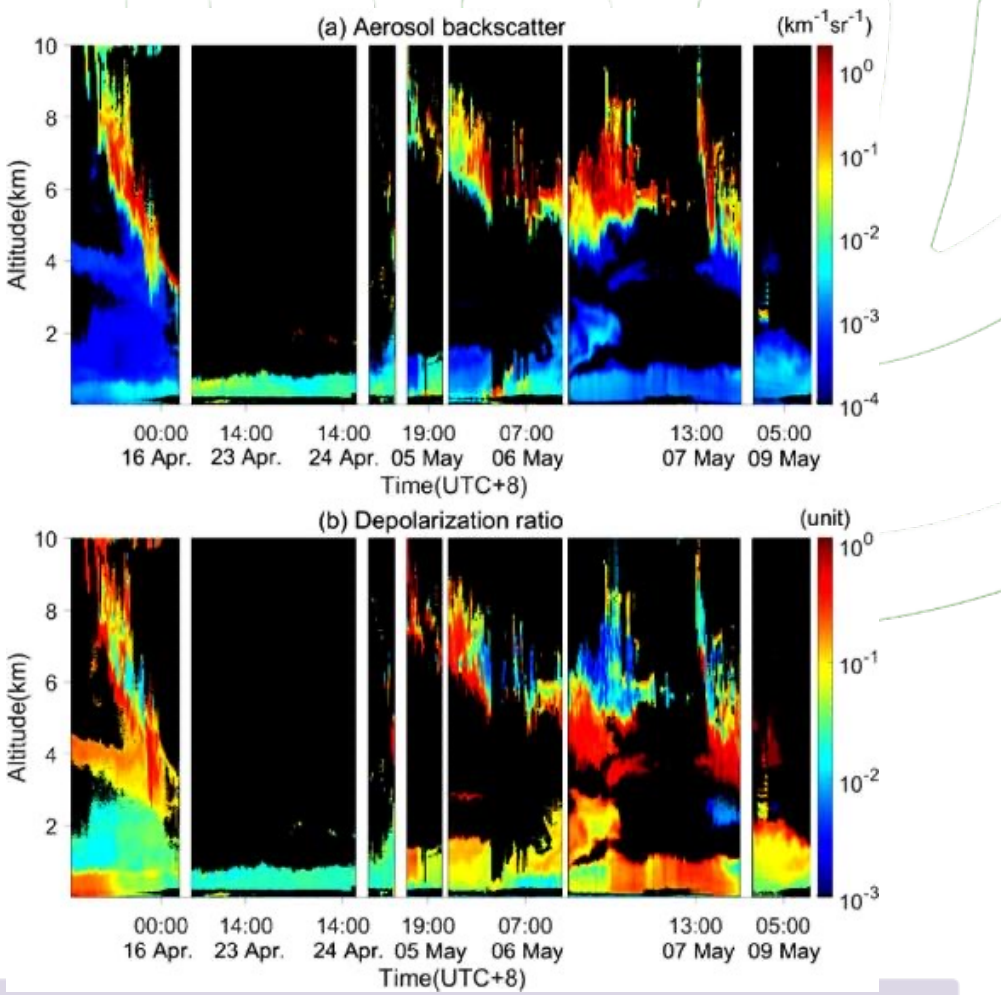

Wang et al., 2021

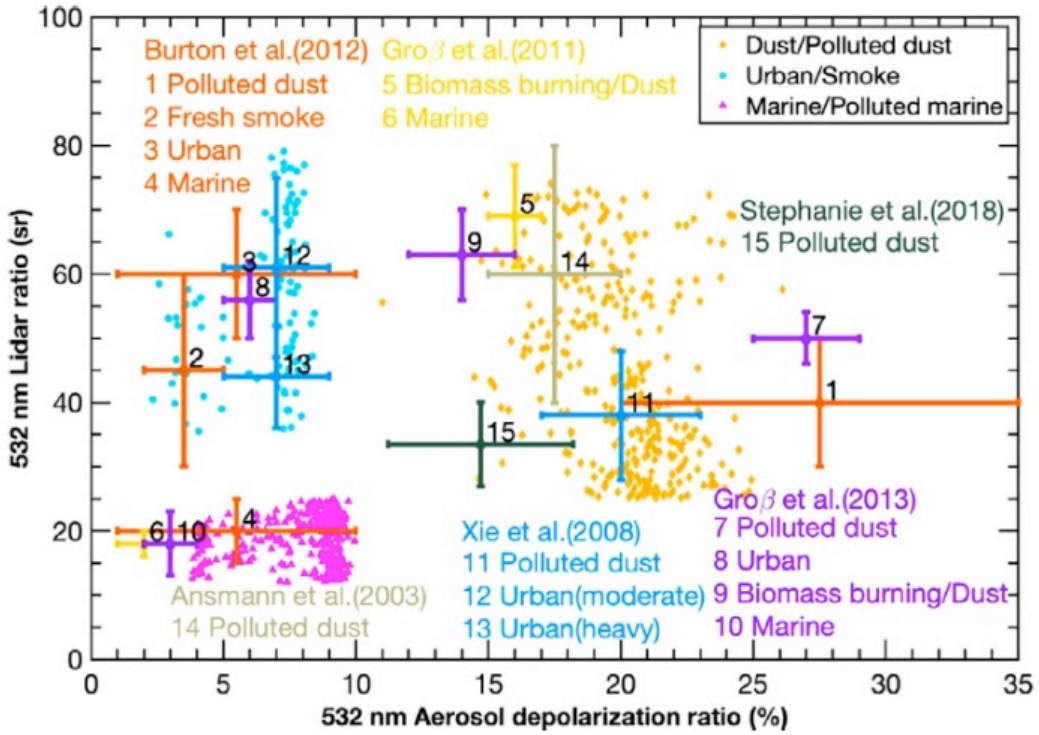

Wang et al., 2021

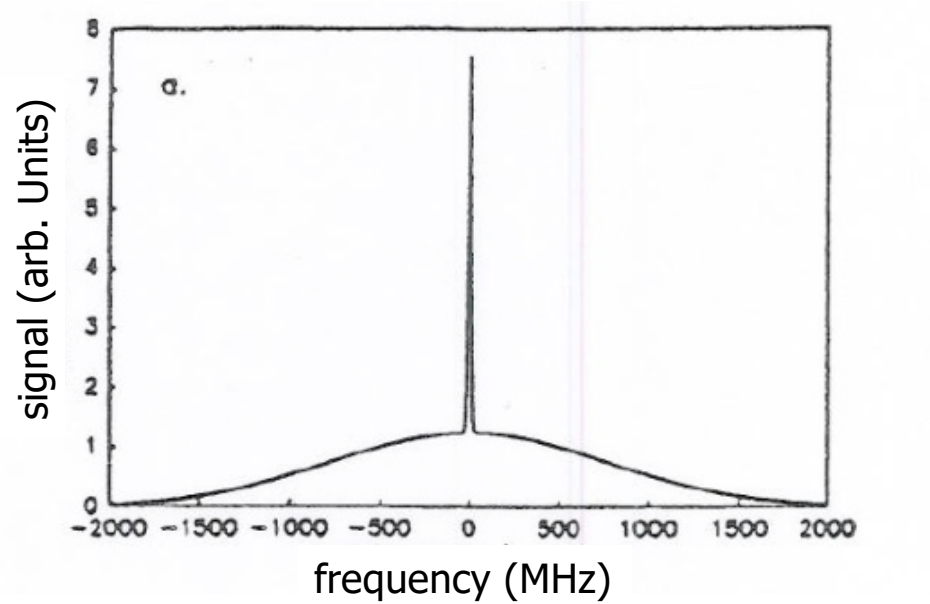

$$\delta\nu_D = 2\frac{\nu_r}{\lambda}$$

At 532 nm, v_r of 1 m/s produces a δv_D of 3.8 MHz

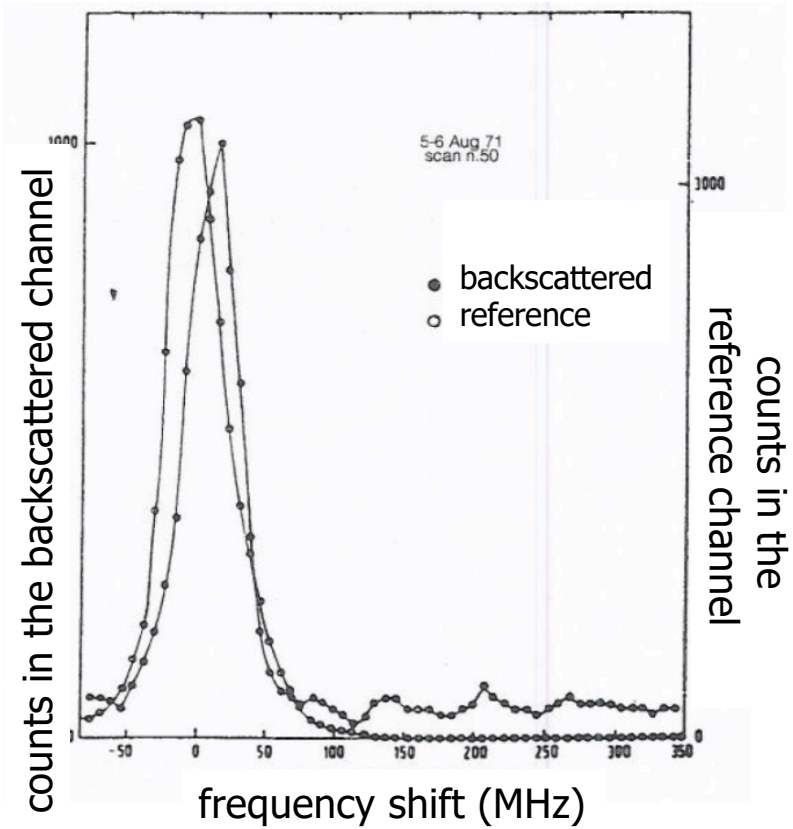

Benedetti Michelangeli et al., 1972

06 JOURNAL OF THE ATMOSPHERIC SCIENCES VOLUME 29

Measurement of Aerosol Motion and Wind Velocity in the Lower Troposphere by Doppler Optical Radar

G. BENEDETTI-MICHELANGELI, F. CONGEDUTI AND G. FIOCCO[1]

European Space Research Institute (ESRIN), Frascati (Rome), Italy

(Manuscript received 19 October 1971, in revised form 6 March 1972)

ABSTRACT

An optical radar has been used to measure the radial wind velocity component in the lower troposphere by detecting interferometrically the bulk Doppler shift affecting the echoes from atmospheric aerosols. The measurements, carried out at night, have basically utilized a highly coherent single-frequency Ar^+ laser

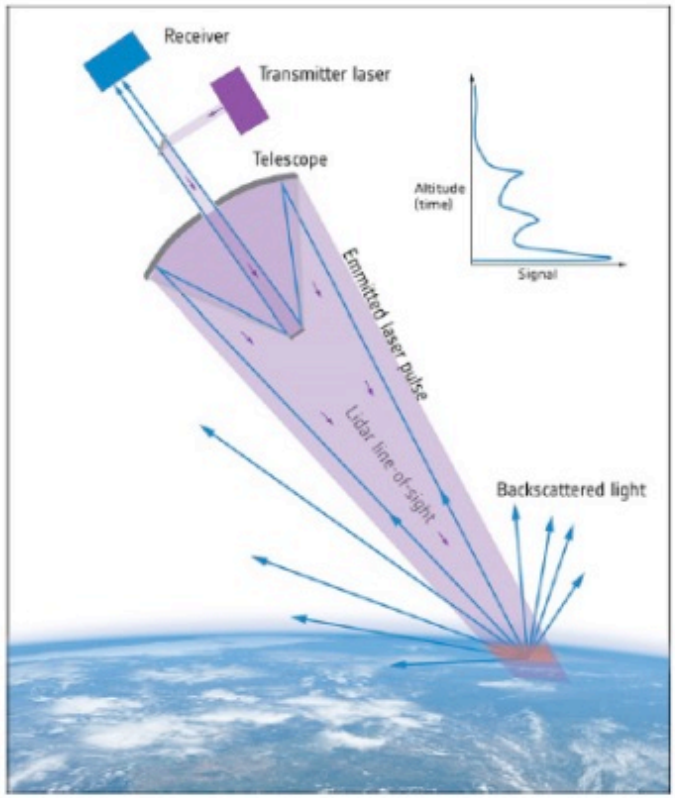

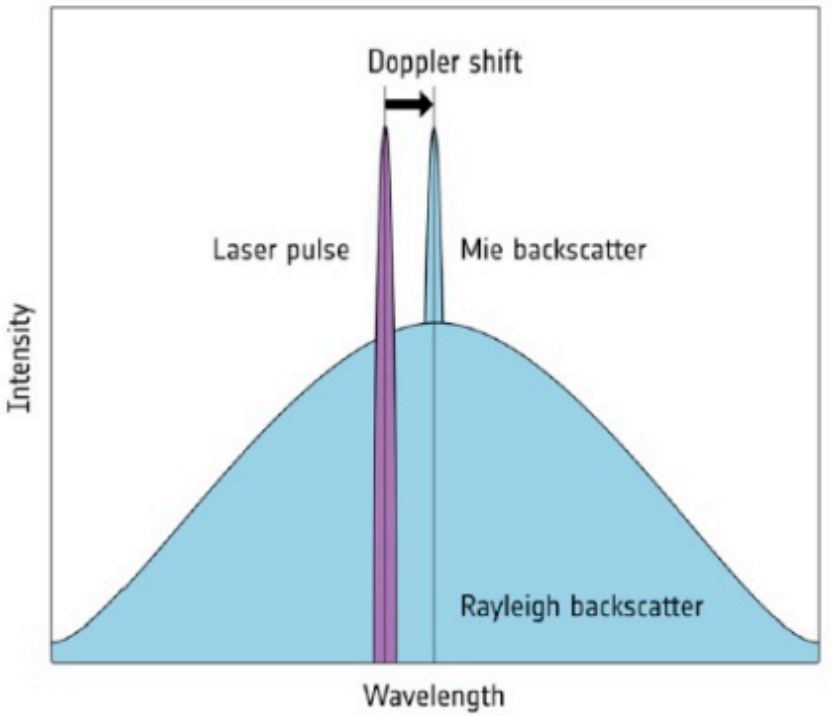

Figure 4: *The ALADIN measurement principle. Wind and atmospheric optical properties profile measurements are derived from the Doppler shifted signals that are backscattered along the lidar line-of-sight (LOS).*

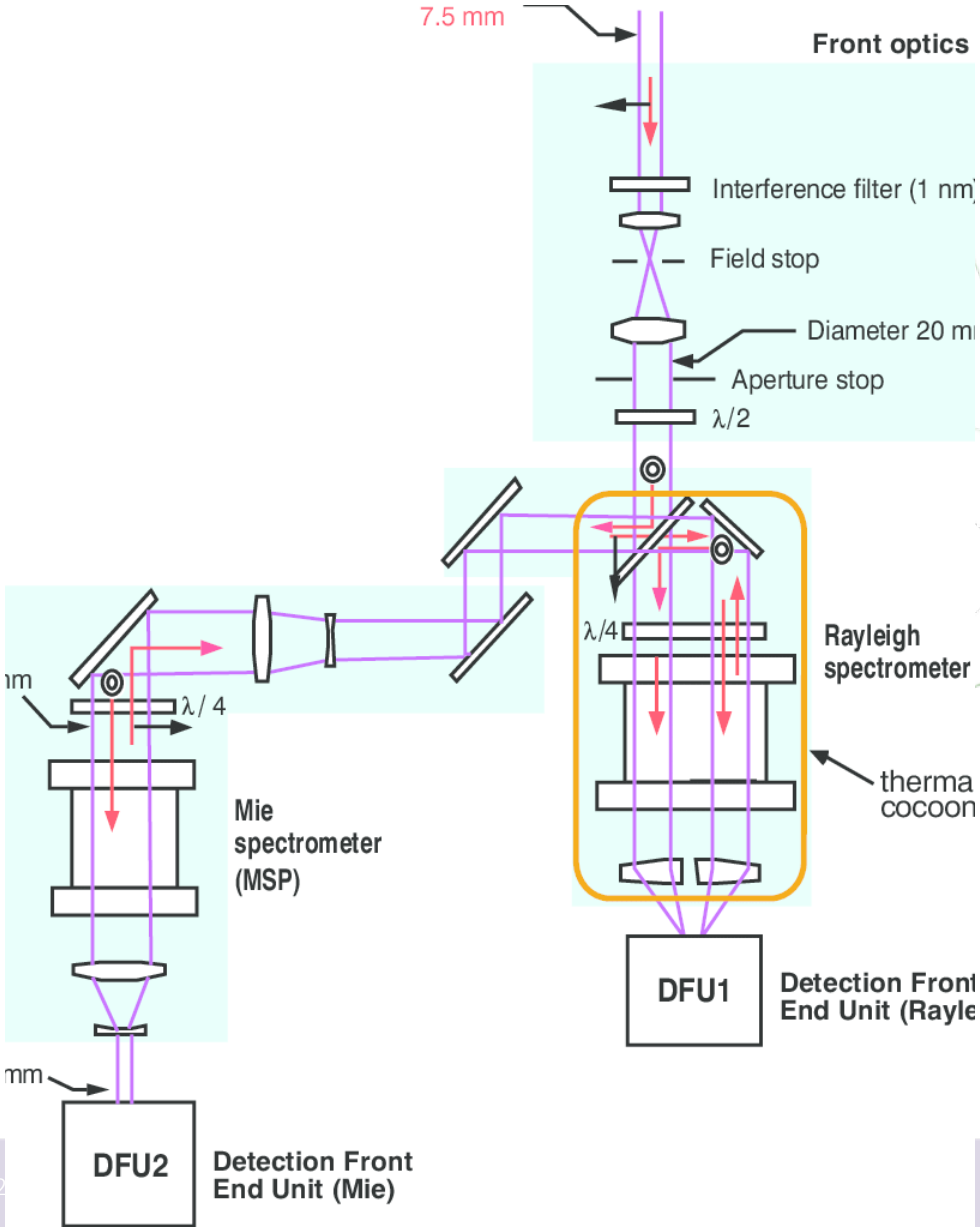
7.5 mm
Front optics
Interference filter (1 nm)
Field stop
Diameter 20 m
Aperture stop
λ/2
λ/4
Rayleigh spectrometer
therma
cocoon
λ/ 4
Mie spectrometer (MSP)
DFU1
Detection Front End Unit (Rayle
DFU2
Detection Front End Unit (Mie)

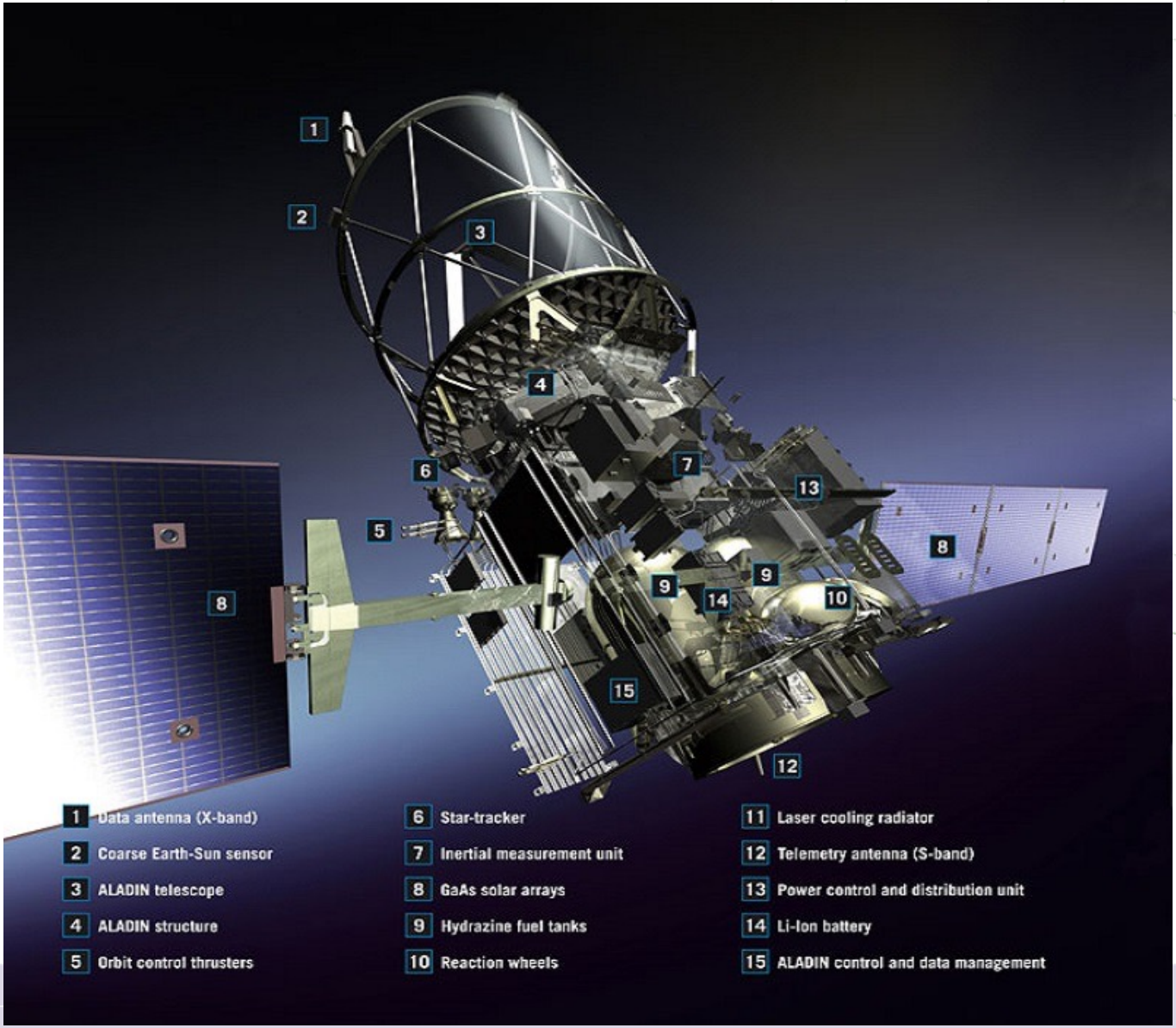
1 Data antenna (X-band)
2 Coarse Earth-Sun sensor
3 ALADIN telescope
4 ALADIN structure
5 Orbit control thrusters
6 Star-tracker
7 Inertial measurement unit
8 GaAs solar arrays
9 Hydrazine fuel tanks
10 Reaction wheels
11 Laser cooling radiator
12 Telemetry antenna (S-band)
13 Power control and distribution unit
14 Li-Ion battery
15 ALADIN control and data management

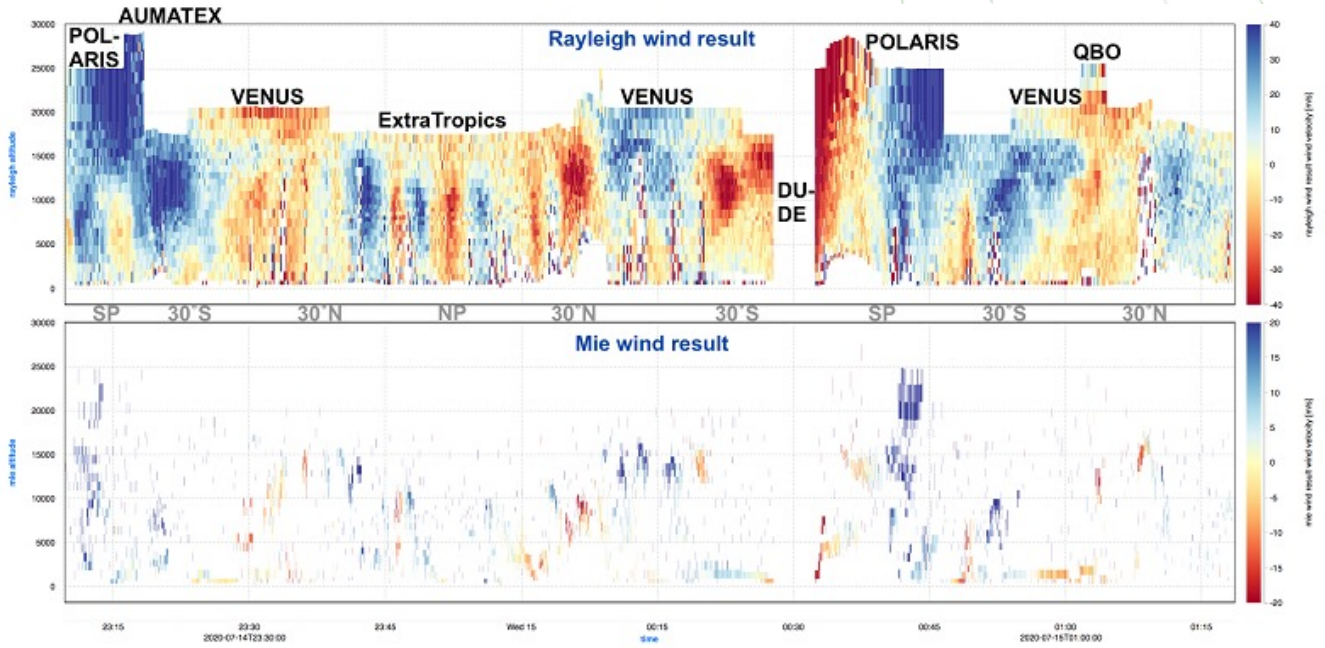
AUMATEX
POL-
ARIS
Rayleigh wind result
VENUS
ExtraTropics
VENUS
DU-
DE
POLARIS
QBO
VENUS
SP
30˚S
30˚N
NP
30˚N
30˚S
SP
30˚S
30˚N
Mie wind result

Wind lidar

Shangguan et al., 2022

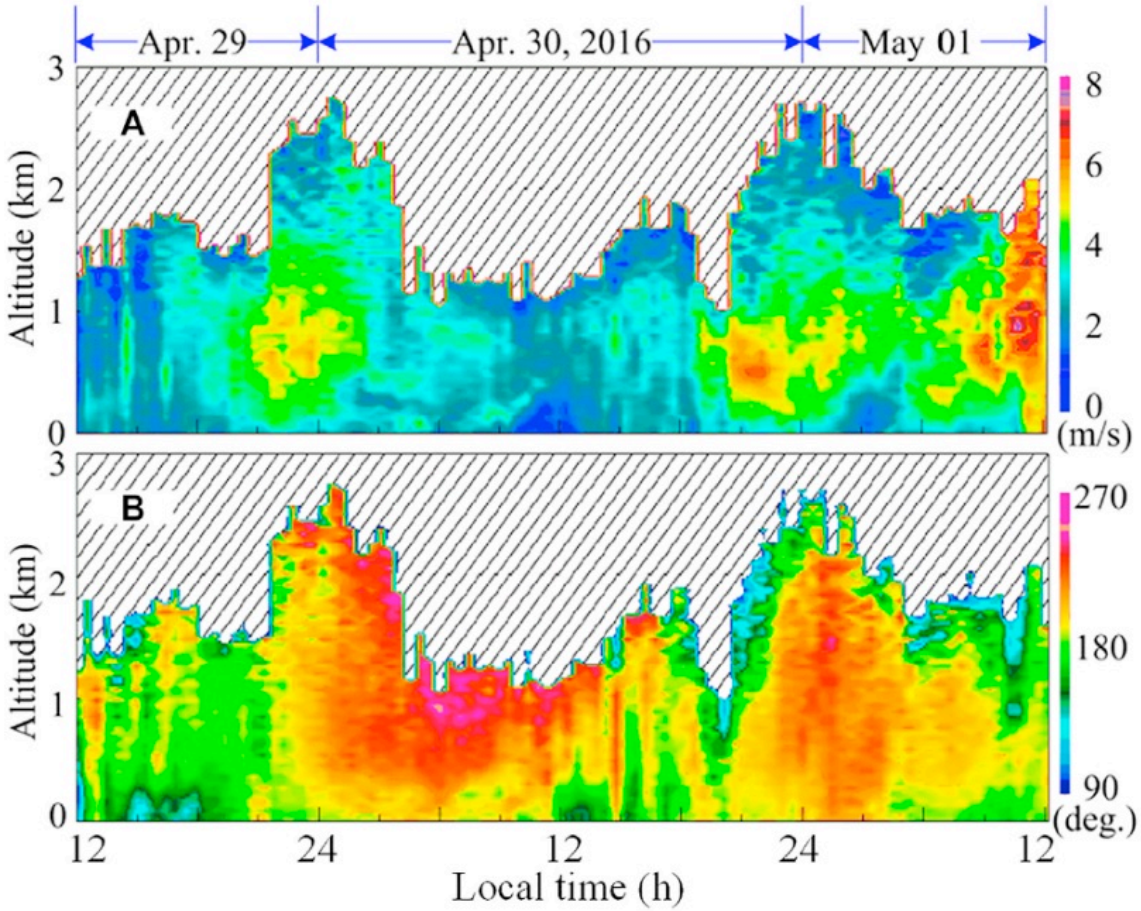

FIGURE 3 | Forty-eight-hour observation of atmospheric wind and visibility. **(A)** Wind speed and **(B)** direction.

- **Incoherent anelastic backscattering lidar (1)**
  - No information from the phase of the signal
  - Emission and detection at different wavelengths

- Incoherent «broadband» anelastic backscattering lidar
  - Raman: aerosol extinction; profile of specific gases
  - Fluorescence: aerosol typing (vegetation, ocean properties)

- Incoherent «narrowband» anelastic backscattering lidar
  - Raman: temperature profile

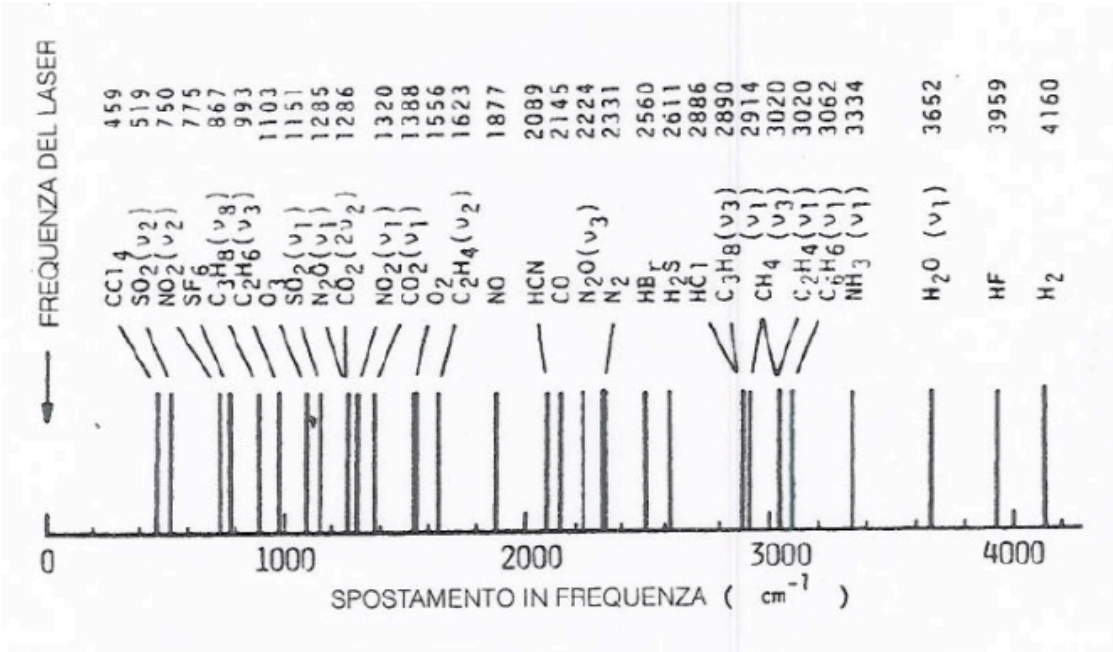

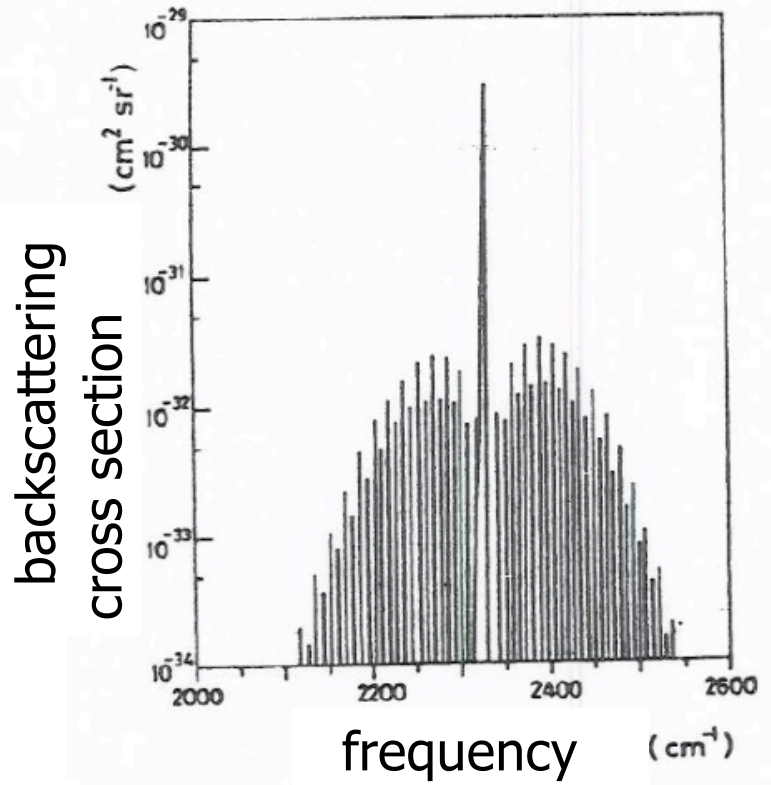

N_2 Raman spectrum

$$P_1(r) = P_0 \frac{A}{r^2} \eta_1 \frac{c\Delta t}{2} \beta_1(r) T_r(\lambda_0, r) T_r(\lambda_1, r)$$

$$P_2(r) = P_0 \frac{A}{r^2} \eta_2 \frac{c\Delta t}{2} \beta_2(r) T_r(\lambda_0, r) T_r(\lambda_2, r)$$

$$\frac{n_2(r)}{n_1(r)} = c \frac{P_2(r) T_r(\lambda_1, r)}{P_1(r) T_r(\lambda_2, r)}$$

160

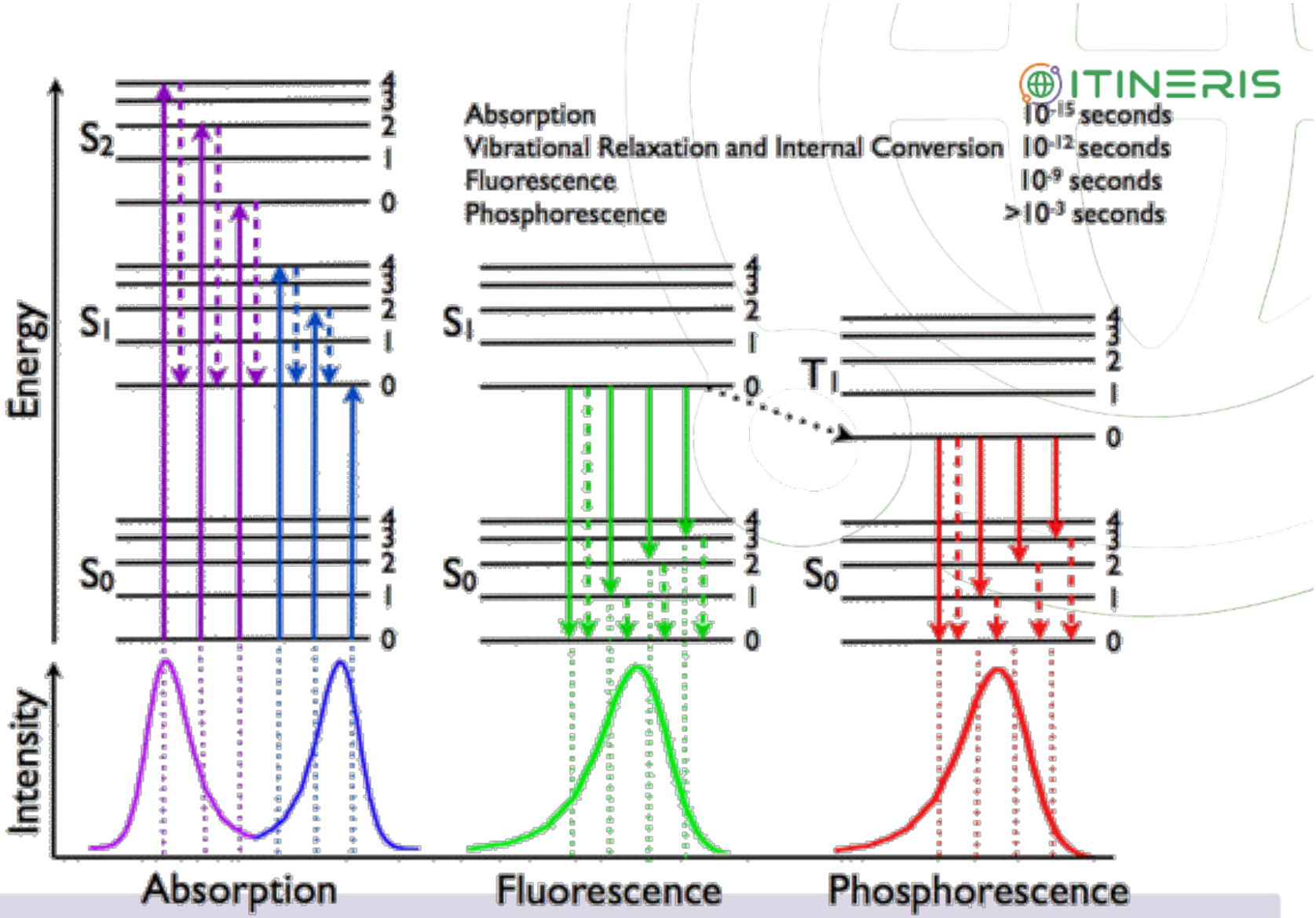
Absorption
Vibrational Relaxation and Internal Conversion
Fluorescence
Phosphorescence
10-15 seconds
10-12 seconds
10-9 seconds
>10-3 seconds
Energy
S2
S1
S0
T1
Intensity
Absorption
Fluorescence
Phosphorescence

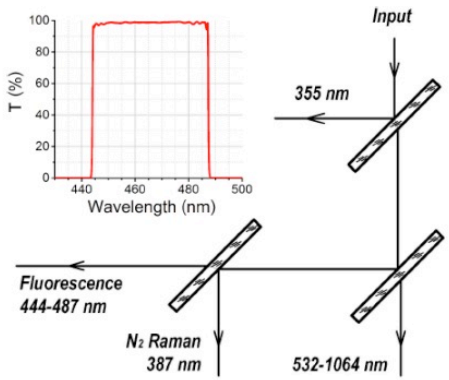

Figure 1. Optical scheme of the elastic, Raman and fluorescence backscatters' separation together with the transmission curve of the interference filter in the fluorescence channel.

Veselovskii et al., 2020

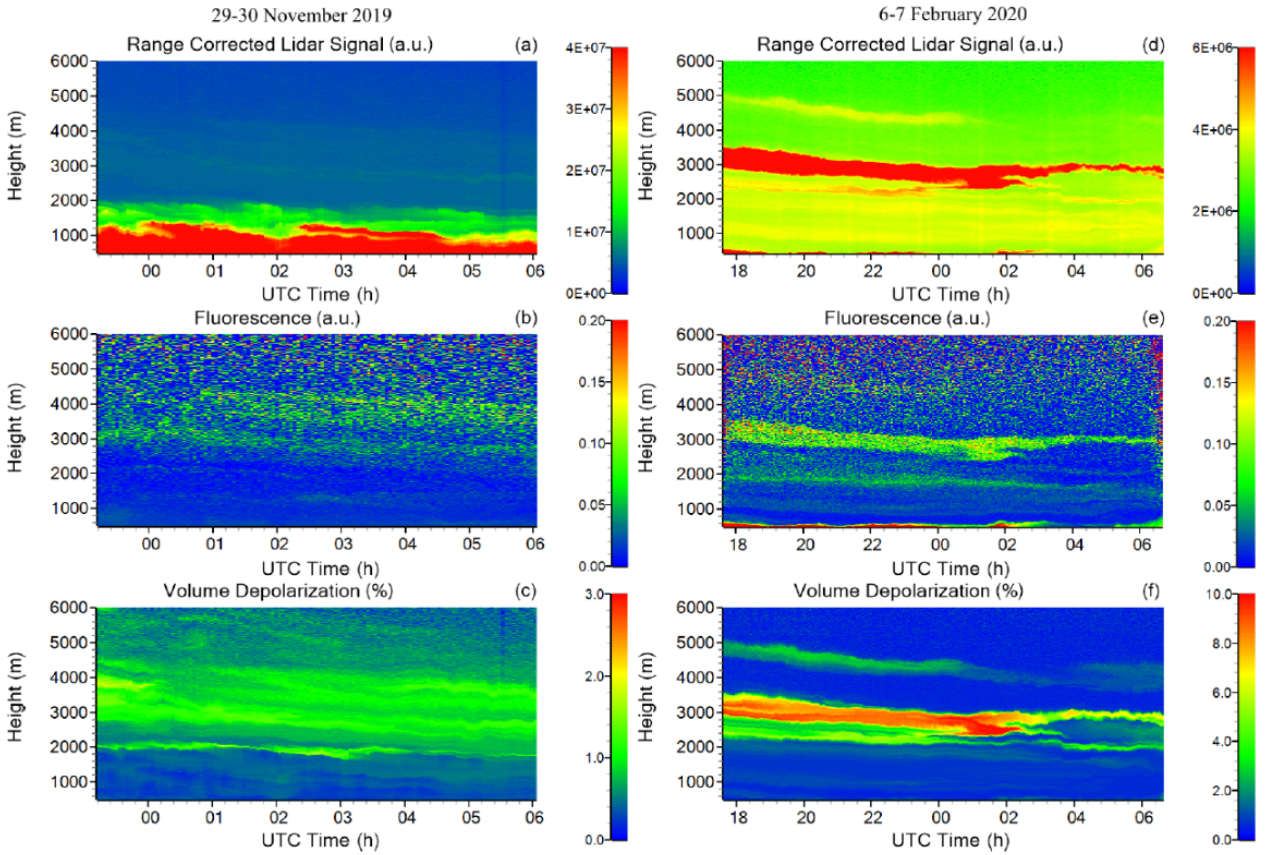

igure 2. The range-corrected lidar signal at 1064 nm, fluorescence backscattering and volume depolarization ratio δ_{1064} measured at Lille n 29–30 November 2019 **(a–c)** and 6–7 February 2020 **(d–f)**.

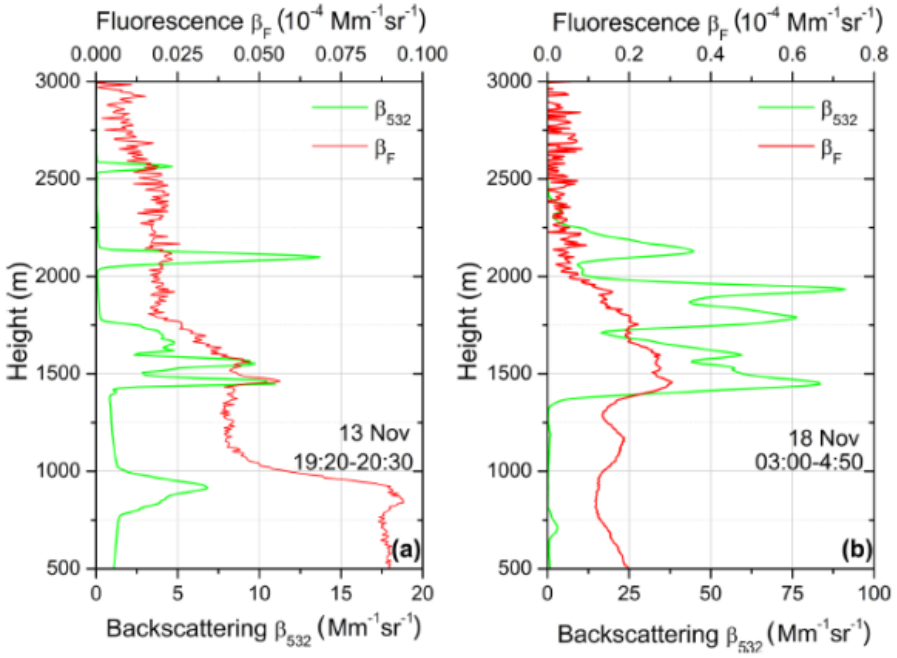

Figure 4. Aerosol (β_{532}) and fluorescence (β_F) backscattering coefficients on 13 and 18 November 2019.

Veselovskii et al., 2020

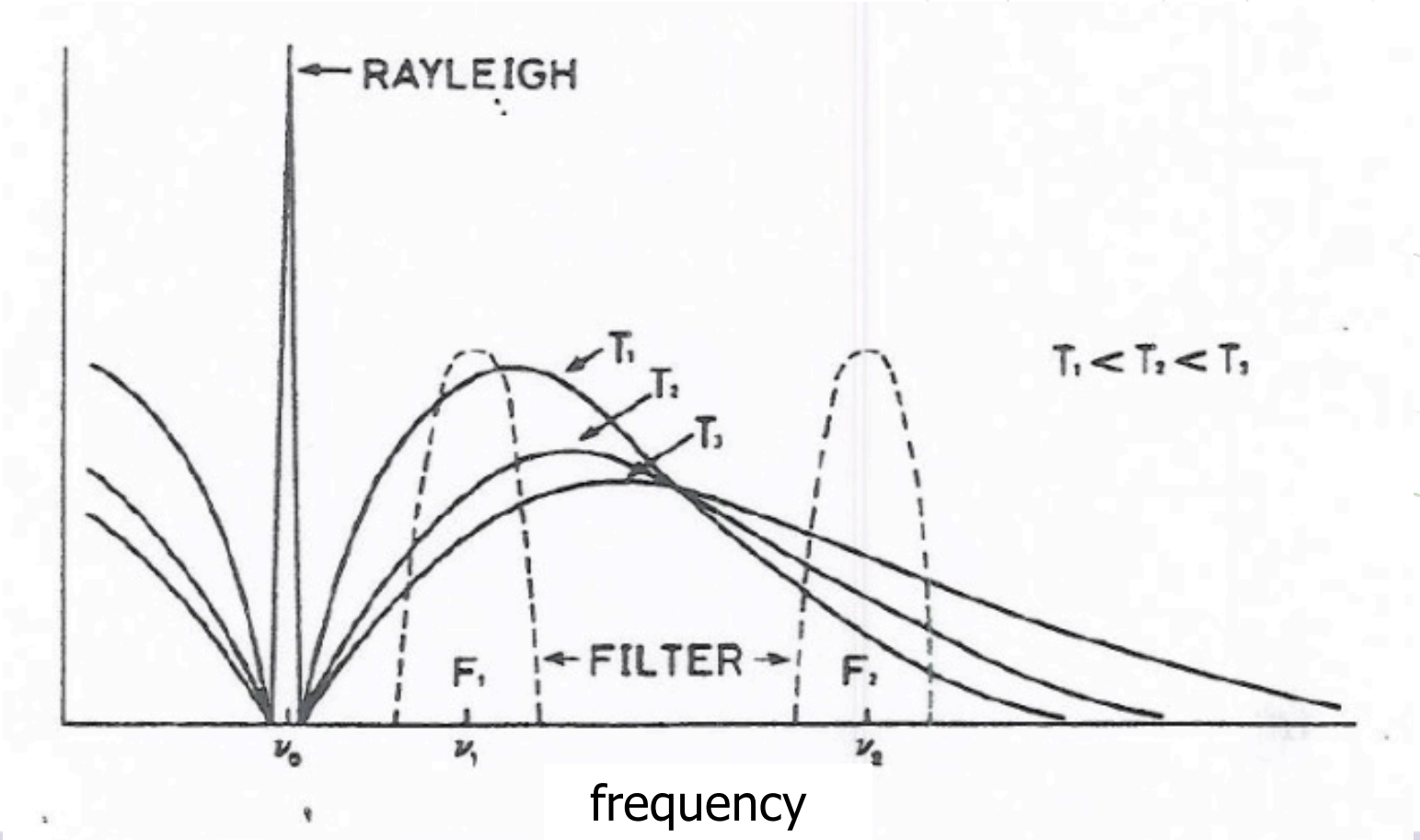
RAYLEIGH
T₁
T₂
T₃
T₁ < T₂ < T₃
F₁
FILTER
F₂
ν₀
ν₁
ν₂
frequency

De Rosa et al., 2020

Table 1. The main characteristics of the BASIL Raman lidar system.

Laser	Nd : YAG
Wavelengths	354.7, 532 nm
Single pulse energy	500 mJ at 354.7 nm, 300 mJ at 532 nm
Pulse repetition frequency	20 Hz
Beam divergence	0.5 mrad (FWHM)
Telescope	Newtonian configuration
Primary mirror diameter	0.45 m
Combined focal length	1.8 m
Field of view	0.5 mrad (FWHM)
Interference filters	Elastic, N_2, H_2O, LoJ, HiJ
Centre wavelength (nm)	354.7, 532, 386.7, 407.5, 354.3, 352.9
Bandwidth (nm)	1.0, 1.0, 1.0, 0.25, 0.2, 1.0
Blocking at 354.7 nm	–, 10^{-6}, 10^{-10}, 10^{-12}, 10^{-8}1, 10^{-8}

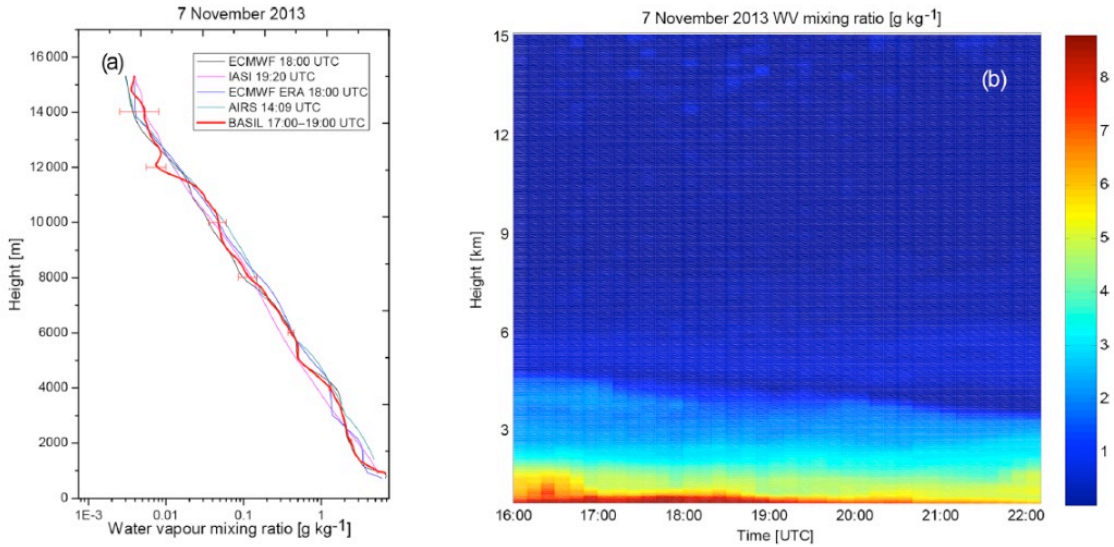

Figure 3. Water vapour mixing ratio profile as measured by BASIL over the time period from 17:00 to 19:00 UTC on 7 November 2013, as well as the closest profiles (in time) from IASI (at 19:29 UTC), AIRS (at 14:09 UTC) and the ECMWF (ERA-15 and ERA-40, at 18:00 UTC) model reanalysis **(a)**. Time evolution of the water vapour mixing ratio profile as measured by BASIL over the interval from 16:00 to 22:00 UTC on 7 November 2013 **(b)**.

Incoherent anelastic backscattering lidar (2)

No information from the phase of the signal

Emission and detection at the same wavelength, in correspondance with an atomic energy level transition (resonance scattering)

- Incoherent «broadband» anelastic backscattering lidar

  Resonance scattering: concentration profile for Na, Ca, Ca+, Fe, K, ...

- Incoherent «narrowband» anelastic backscattering lidar

  Resonance scattering, hyperfine structure: temperature profile

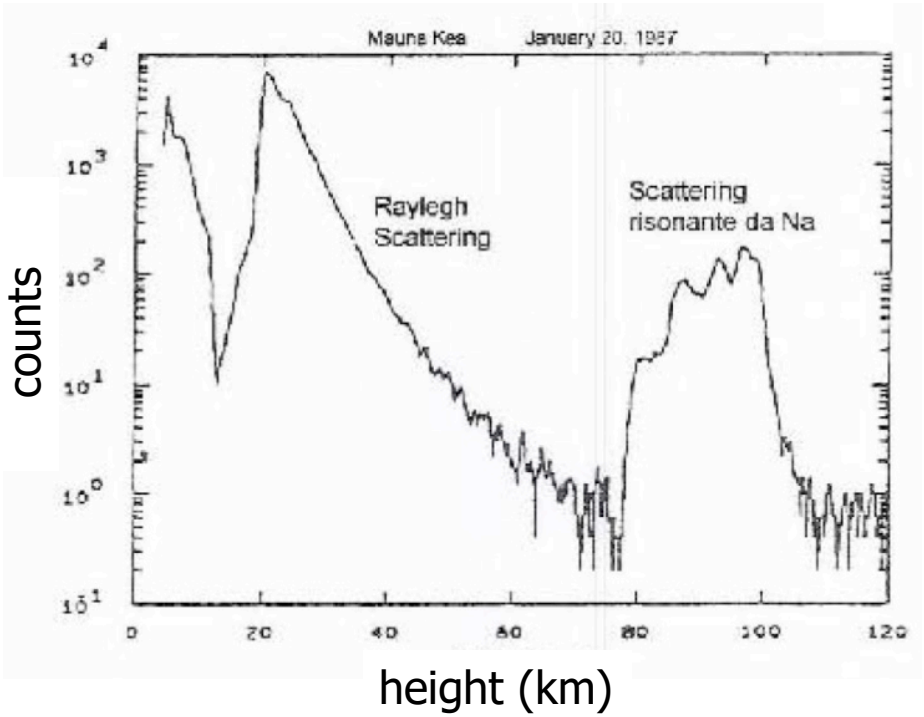
Mauna Kea January 20, 1987
Rayleigh Scattering
Scattering risonante da Na
counts
height (km)

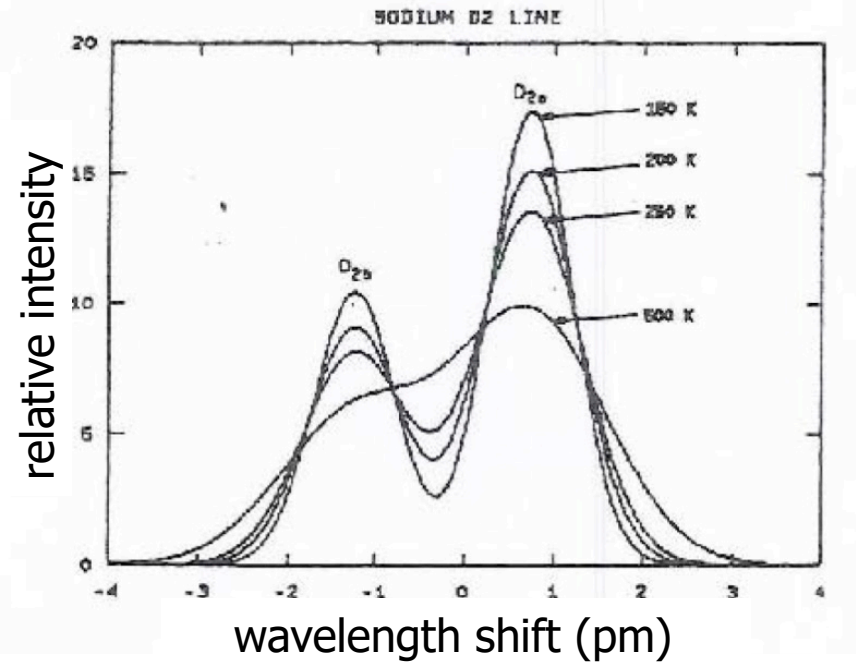
SODIUM D2 LINE
relative intensity
wavelength shift (pm)

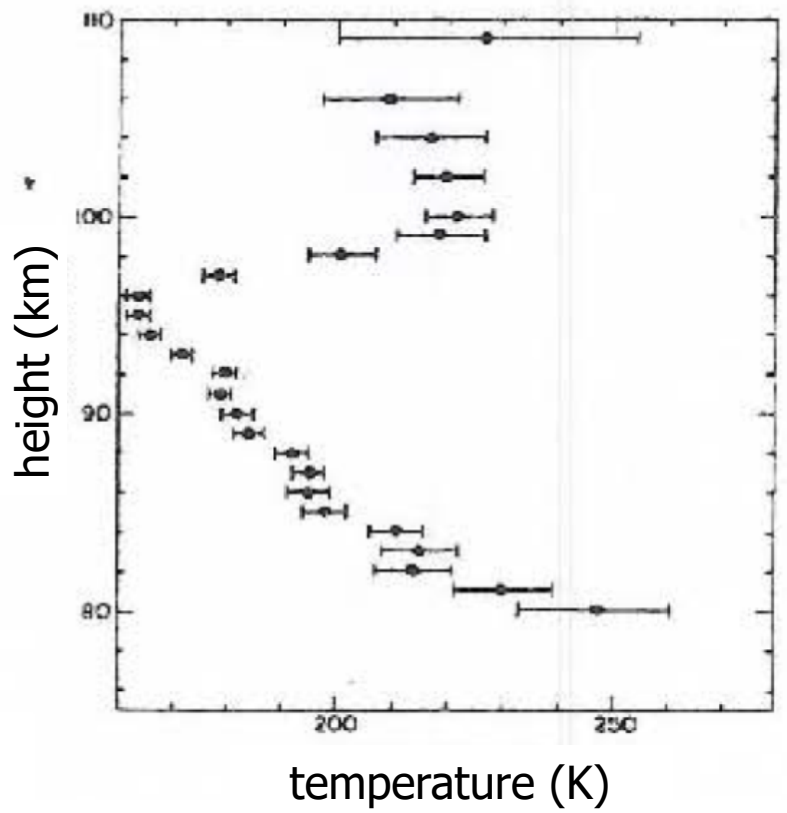

Fricke and von Zahn, 1985

- **Coherent elastic backscattering lidar**
  - Information in the phase of the signal
  - Emission and detection at (almost) the same wavelength, elastic scattering

- Coherent «narrowband» elastic backscattering lidar
  - Temperature profile, aerosol profile, wind

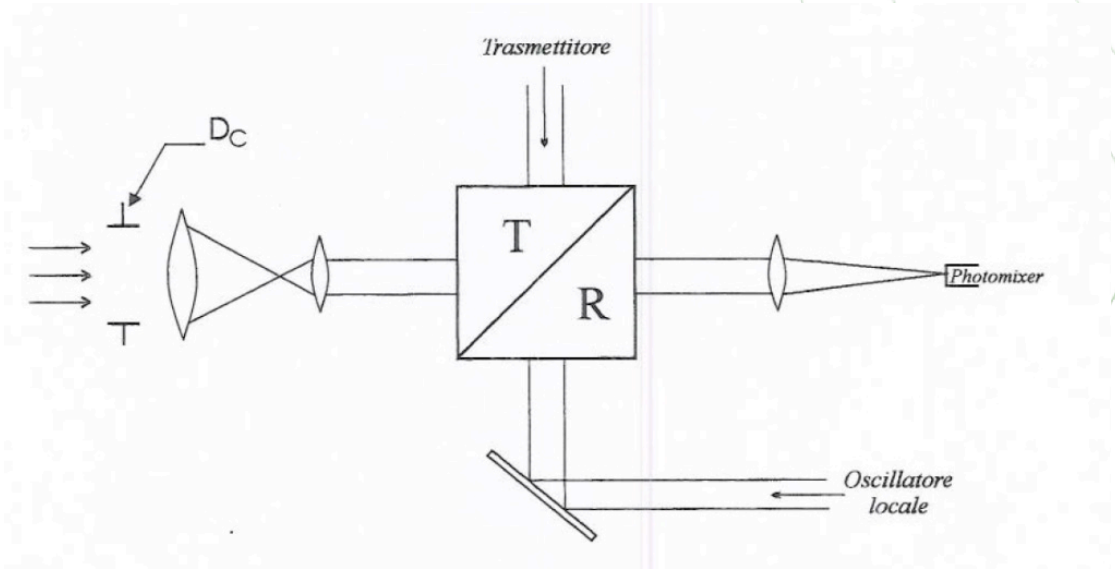
Trasmettitore
Dc
T
T
R
Photomixer
Oscillatore
locale

Range corrected signal
Clouds

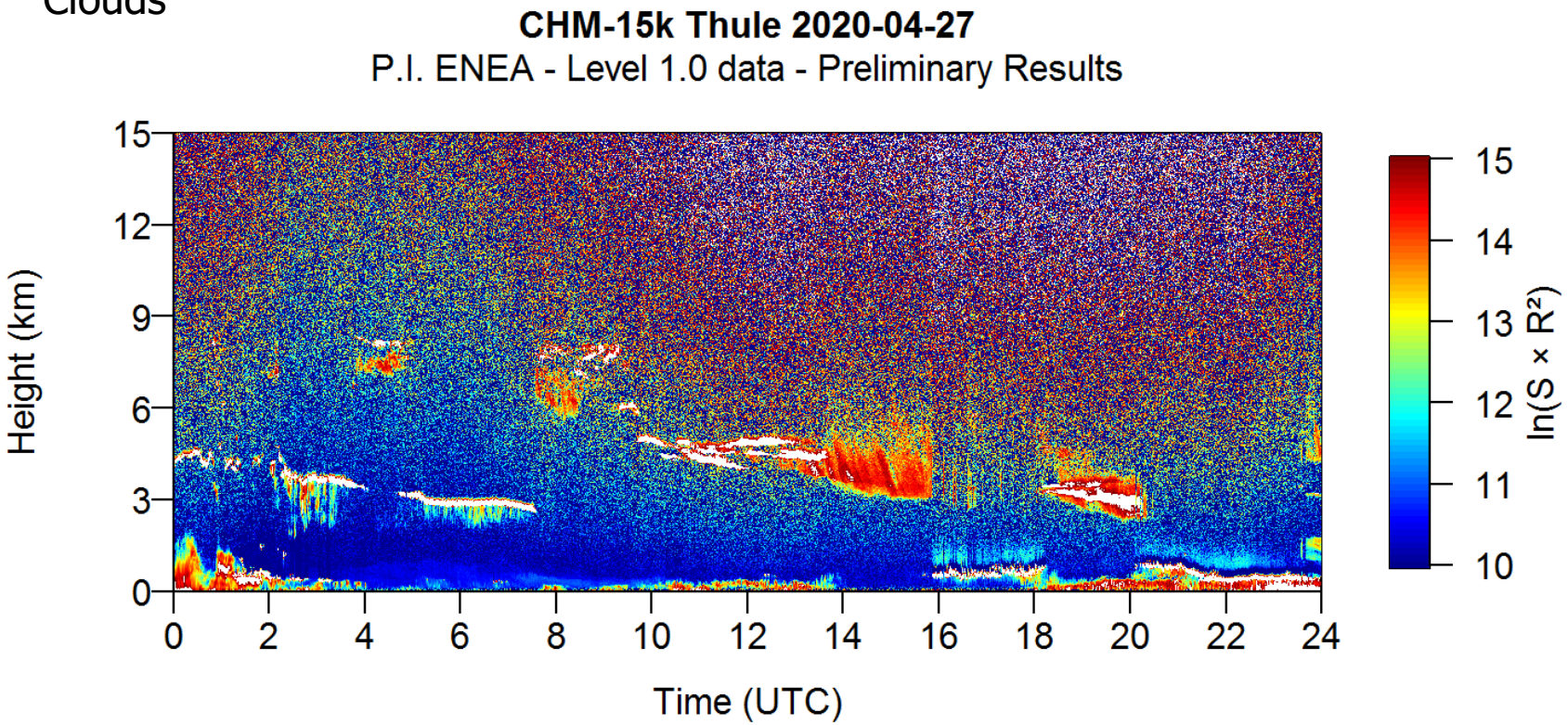

International Collaborations with NASA

From the early stages of mission definition, **NASA** showed interest in the initiative and a **fruitful collaboration was immediately established between the two agencies.**

NASA confirmed its interest through the involvement in the mission of authoritative scientists and engineers from its two centers: the Langley Research Center (**LaRC**) and the Goddard Space Flight Center (**GSFC**).

Image credit: NASA

LITE - NASA

volò sul Discovery Space Shuttle nel settembre 1994

past

Image credit: NASA, CNES

CALIPSO - NASA

trasmettitore laser a due lunghezze d'onda (IR and VIS).
2006-2023

Image credit: NASA

CATS - NASA

operato da febbraio 2015 a ottobre 2017 a bordo della Stazione Spaziale Internazionale;

Image credit: ESA

AEOLUS - ESA

Strumento Lidar con il primo trasmettitore laser UV nello spazio
2018-2023

present

Image credit: ESA

EARTHCARE - ESA

Strumento Lidar con trasmettitore laser UV.
2024-today

Image credit: CNES

MERLIN - DLR-CNES

Image credit: NASA

AOS – NASA

future

Members of the CALIPSO team have been involved by NASA in the collaboration with ASI for the Implementation of the Luce mission

F2F in LaRC June 2024

14

CALIOP on CALIPSO

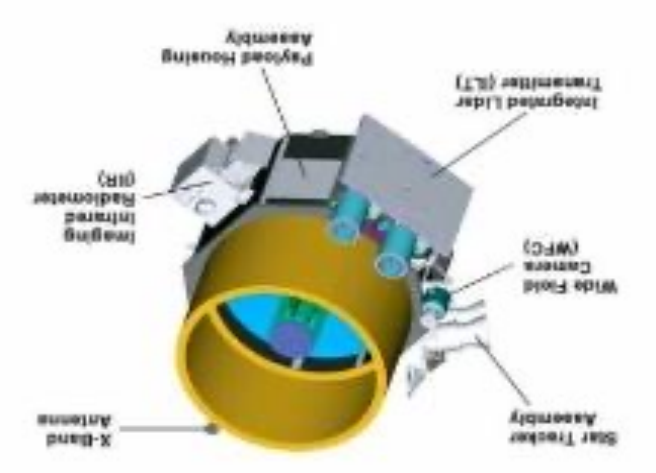

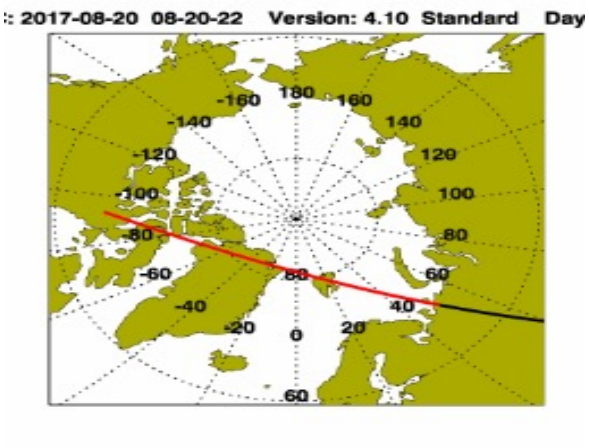

Arctic fire plumes

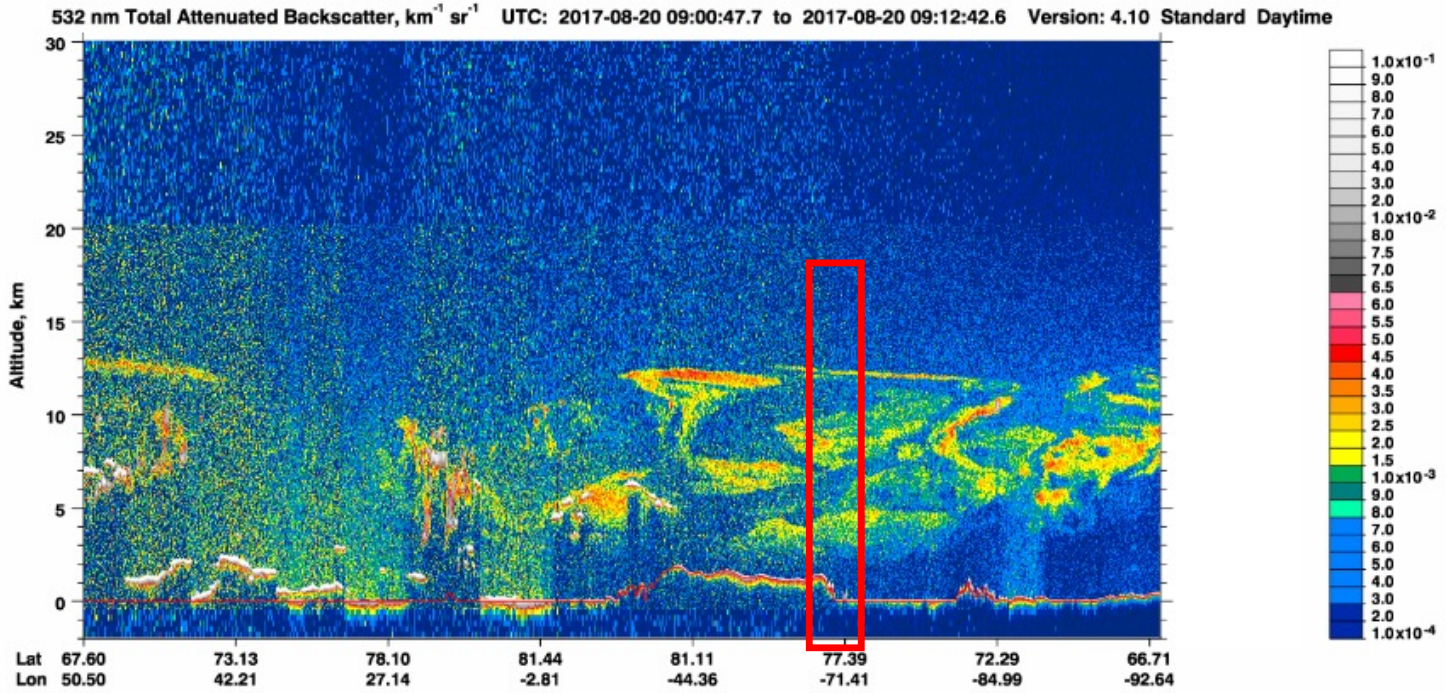

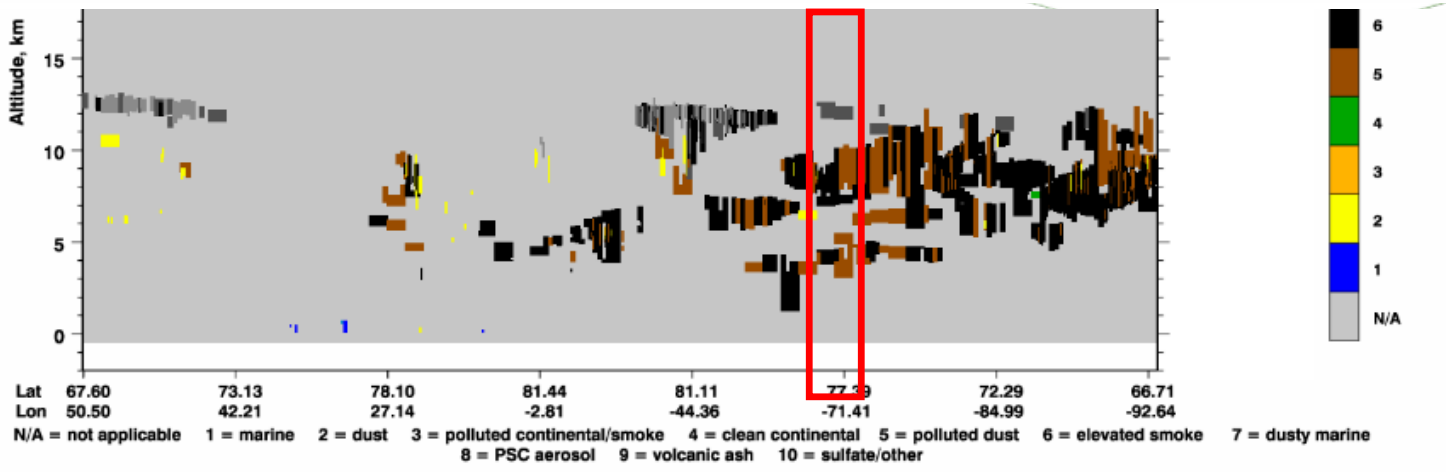

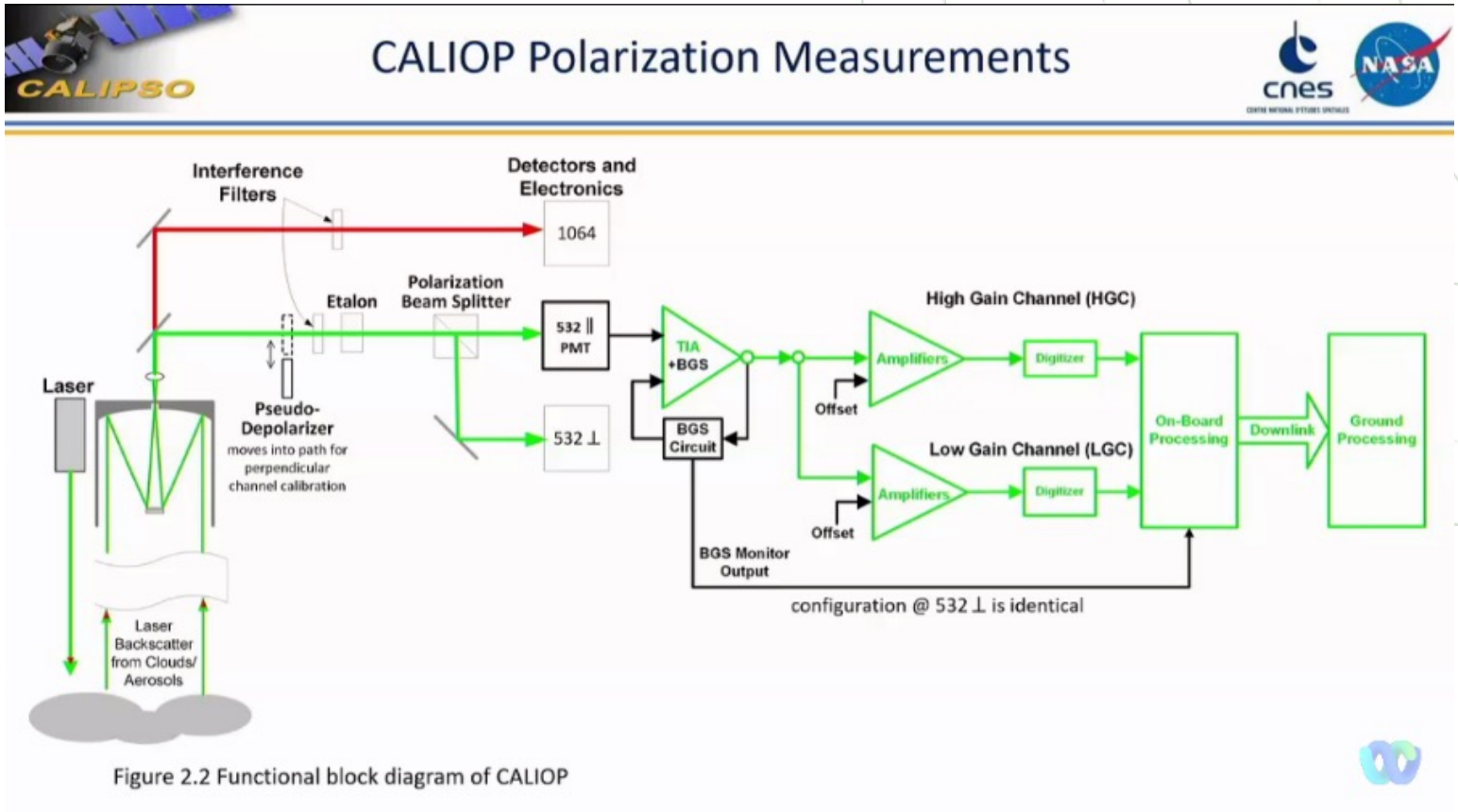

Figure 2.2 Functional block diagram of CALIOP

About EarthCARE

Earth Explorers are **research missions designed to address key scientific challenges**, while demonstrating breakthrough technology in observing techniques. Every Earth Explorer mission provides an important contribution to further understanding of our planet

What

The largest and most complex Earth Explorer to date, it is ESA's cloud, aerosol and radiation explorer mission

Where

EarthCARE is a joint venture between ESA and JAXA (Japan Aerospace Exploration Agency)

Aim

EarthCARE will improve current climate and numerical weather prediction models, advancing our knowledge of:

- **the role that clouds and aerosols play in reflecting incident solar radiation back into space**
- **how infrared radiation emitted from Earth's surface is trapped in the atmosphere**

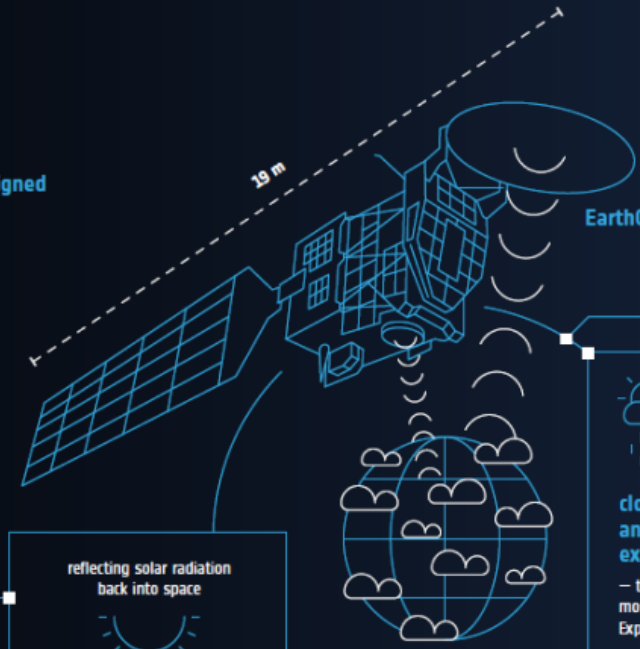

cloud, aerosol and radiation explorer mission

– the largest and most complex Earth Explorer mission

high-performance lidar and radar technology, which has never been flown in space before

Innovation

EarthCARE will employ high-performance lidar and radar technology, which has never been flown in space before. The High Spectral Resolution Lidar operates in the UV and also filters co- and cross- polarised signals. The Cloud Profiling Radar offers Doppler capability

Instruments

EarthCARE carries a suite of instruments:
an atmospheric lidar (ATLID), a cloud profiling radar (CPR), a multispectral imager (MSI) and a broad-band radiometer (BBR)
The two active instruments, ATLID and CPR, probe the atmosphere to collect data at a microscopic level, observing clouds, aerosols and precipitation. The two passive instruments (MSI and BRR), provide complementary optical and radiation measurements, necessary for scientific products
The mission will help scientists to improve atmospheric models by 'closing the loop', providing an actual measurement of the radiation balance that will also be calculated by models fed with observation data collected by the active instruments

Curiosity

EarthCARE is 19 m long with the solar panel deployed. The solar wing is an essential part of the satellite, providing the energy for EarthCARE to do its job

EarthCARE mission page: earth.esa.int/eogateway/missions/earthcare

ATLID (ATmospheric LIDar)

Orbit	Routine operations
Orbit Type	Sun-synchronous
Mean Solar Local Time	14:00 (descending node)
Mean Spherical Altitude	393.14 km
Inclination	97.05°
Repeat Cycle	25 days/389 orbits
Orbital Duration	5552.7 seconds

Parameter	
Operating Wavelength	354.8 nm
Emitted Energy	38 mJ
Receiver Footprint Diameter	≤ 30 m
PRF	51 Hz
Transmit Pulse Width	20 ns
Altitude Range	-0.5 to +40 km
Vertical Sampling Interval	103 m (up to 20.2 km) 500 m (20.2 km - 40 km)
Along Track Sampling Interval	285 m (2 shots accumulated onboard)
Channels	HSRL particulate HSRL Molecular Depolarization channel

ATLID (ATmospheric LIDar)
UV HSRL with Linear Depolarization channel

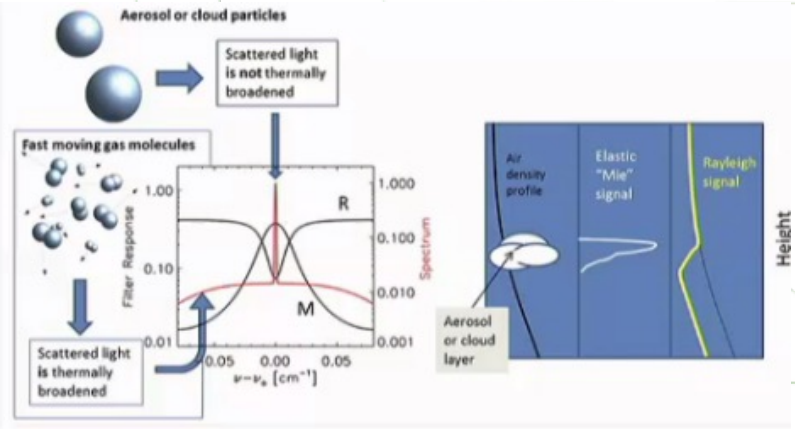

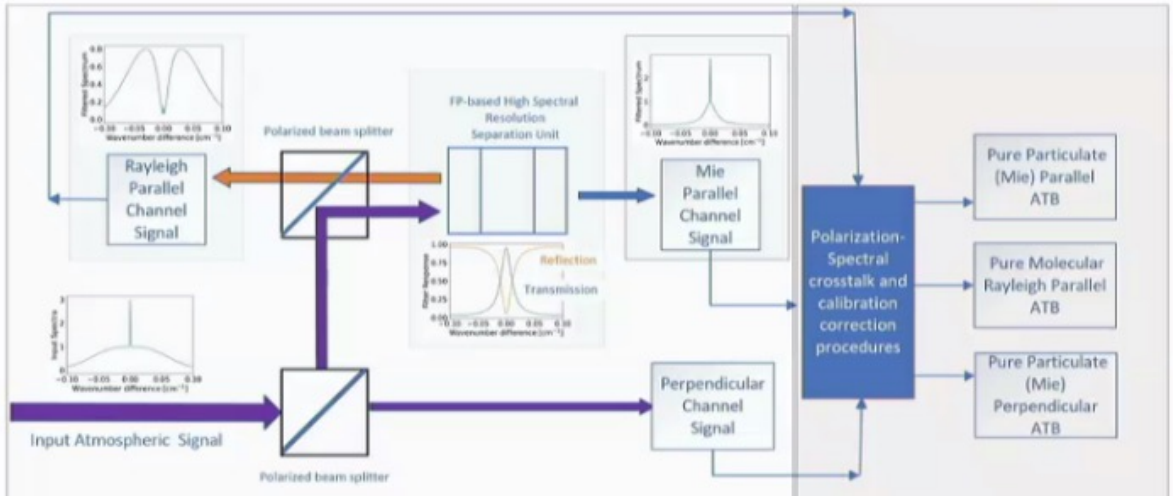

HSRL

⇒ Good daylight performance
⇒ More accurate retrievals
⇒ Extinction + Backscatter are retrieved.
⇒ More info. content.

Birth of a Hot Pixel

Cross-Polar Channel

Frame 1355D 08/24 : 0305

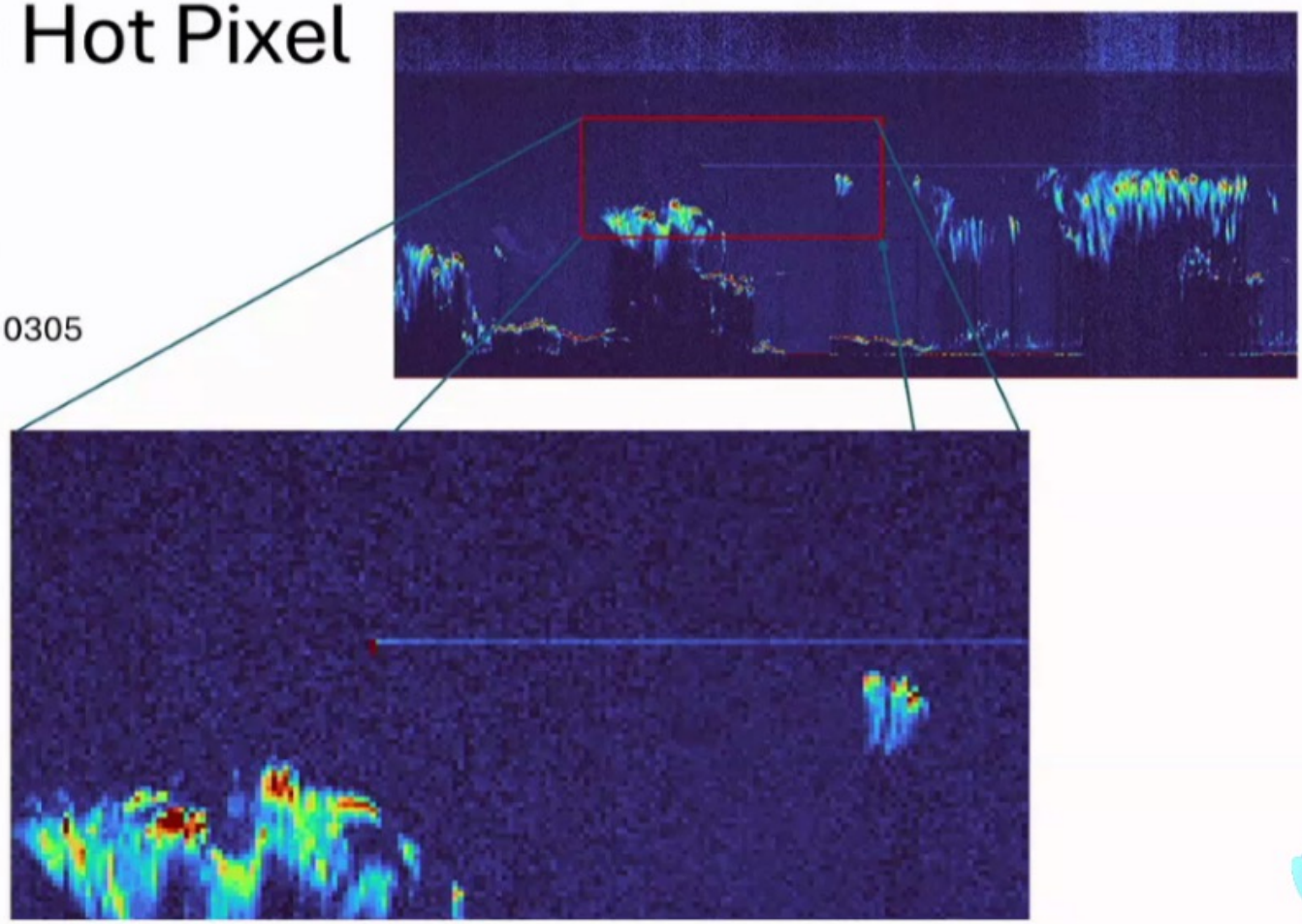

THANKS!

IR0000032 – ITINERIS, Italian Integrated Environmental Research Infrastructures System
(D.D. n. 130/2022 - CUP B53C22002150006) Funded by EU - Next Generation EU PNRR-Mission 4 "Education and Research" - Component 2: "From research to business" - Investment 3.1: "Fund for the realisation of an integrated system of research and innovation infrastructures"